DEVELOPMENT OF A NEW MODEL-BASED RADIATION DOSE CALCULATION ALGORITHM FOR KILOVOLTAGE ENERGY X-RAYS

By

Jason M. Pawlowski

Dissertation

Submitted to the Faculty of the

Graduate School of Vanderbilt University

in partial fulfillment of the requirements

for the degree of

DOCTOR OF PHILOSOPHY

in

Physics

August, 2013

Nashville, Tennessee

Approved:

George X. Ding, Ph.D.

Charles W. Coffey, II, Ph.D.

David J. Ernst, Ph.D.

David R. Pickens, Ph.D.

J. Michael Fitzpatrick, Ph.D.

To my infinitely loving and supportive wife, Michelle,

our daughter Josephine,

and our growing family.

Acknowledgments

I am grateful to have received the generous help and guidance of many people over the course of my graduate studies. It is a great pleasure to thank Dr. George Ding who has been a supportive advisor, a committed teacher, and a good friend. This dissertation would not have been possible without his mentorship and essential contributions. The Monte Carlo calculations that were used to develop and benchmark the algorithms described within were performed by Dr. Ding. Additionally, I began this work as a full-time student in June of 2009. In September, 2010, I accepted a full-time position as a clinical medical physicist, leaving me to complete my dissertation research as a part-time student. I am extremely grateful for the patience and lenience granted to me by Dr. Ding which has allowed me to pursue my profession while completing my dissertation research.

I want to thank my dissertation committee members for their invaluable time, support, and guidance. Dr. Charles Coffey has been a mentor to me as a graduate student and as a medical physicist. I am grateful to Dr. David Ernst, Dr. J. Michael Fitzpatrick, and Dr. David Pickens for their probing and insightful comments that have been instrumental in guiding my dissertation.

I am also grateful to the faculty and staff of the Vanderbilt University Department of Physics and Astronomy. In particular, Dr. Richard Haglund, Don Pickert, Dr. Julia Velkovska, and Peggy McGowan were extremely helpful in advising me and facilitating my transfer to the department.

My family, friends, and colleagues have been a tremendous support for me throughout my graduate studies. I am indebted to my parents, John and Jane, for instilling in me the need to always push myself and the desire to always look deeper. My Grandfather, Bernard Saper, was instrumental in inspiring my love of science. My colleague and friend,

Dr. Keith Ver Steeg, has been extrememly supportive of me and has been an important source of encouragement and advice.

Lastly, I want to express my deep appreciation and love of my wife, Michelle. She has provided unwavering support and encouragement, and is in large part the reason I am the person I am today.

Contents

List of Tables

List of Figures

List of Symbols

I Introduction

I.1 Overview

I.1.1 Motivation and organization

Kilovoltage (kV) energy x-rays are used with increased frequency in medicine to aid in both the diagnosis and treatment of disease. For example, there has been a rapid increase in the number of computed tomography (CT) examinations performed annually in the United States, with an estimated 62 million individual procedures performed in 2006, up from around 10-12 million in 1990 [19]. While the diagnostic information provided by x-ray imaging is often critical for patient care, there are significant concerns about the risks of carcinogenesis from the increased radiation exposure to patients from imaging [14, 15, 17–19, 43].

In addition to their diagnostic utility, kilovoltage energy x-rays are useful for treating superficial tumors on or near the surface of the body such as skin cancers, kaposi's sarcoma, and certain non-cancerous lesions such as keloids.

Due to the frequent use of kilovoltage energy x-rays in medicine there is a need to calculate the radiation dose to patients from these procedures. Existing techniques commonly used for clinical dose calculation are inadequate for this application. Model-based convolution/superposition algorithms are universally utilized for 3-dimensional dose calculations for radiation therapy treatment planning. These algorithms have become the standard for clinical radiotherapy dose calculations due to their high degree of accuray, efficiency, and ease of implementation. Current model-based dose calculation algorithms implemented in

commercial radiotherapy treatment planning systems, however, are inaccurate for kilovoltage photon beams as these techniques were designed with approximations appropriate for megavoltage (MV) photon beams that are not applicable in the kilovoltage energy range.

Due to the widespread use of model-based convolution/superposition algorithms in radiation therapy clinics for patient-specific dose calculations it is desireable to extend this approach to the kilovoltage energy range. In this dissertation we present a new model-based convolution/superposition dose calculation algorithm for kilovoltage x-rays developed to overcome the limitations of existing algorithms for these energies. This algorithm has the potential for clinical implementation to calculate the radiation dose to patients from imaging procedures such as computed tomography and fluoroscopy as well as for kilovoltage energy radiation therapy treatments.

In the following sections we review the basics of radiation dose and model-based convolution/superposition algorithms.This is followed by a discussion of the previous work done in kilovoltage dosimetry for both therapeutic and diagnostic procedures. Lastly, we develop the new calculation algorithm for kilovoltage energy x-rays and present benchmark calculations testing it for the specific cases of calculating the dose to real patients from kilovoltage cone-beam CT (kV-CBCT) and single-angle projection imaging. These test cases were chosen due to their increased utility for patient set up for image-guided radiation therapy (IGRT).

I.1.2 Radiation dose

In radiological physics the parameter that is typically correlated with the physiological effects of radiation is absorbed dose, defined as the energy imparted to matter per unit mass. The SI unit of absorbed dose is the Gray (Gy, 1 Gy=1 J/kg). Radiation

therapy and diagnostic imaging frequently use high-energy photon beams for therapeutic and diagnostic procedures. The interactions of these high energy photons in tissue produce a shower of primary electrons. The local energy deposition in tissue from these interactions is the fraction of the primary electron kinetic energy that is lost to tissue while traveling minus any radiative losses due to bremsstrahlung radiation and characteristic x-rays.

Under specific conditions the absorbed dose can be expressed simply in terms of the incident photon fluence and the properties of the absorbing medium. For a single mass element, if the conditions of charged-particle equilibrium are met, i.e.:

1. The atomic composition of the absorbing medium is homogeneous;
2. The density of the absorbing medium is homogeneous;
3. There exists a uniform field of indirectly ionizing radiation such as photons;
4. No inhomogeneous electric or magnetic fields are present;

then the absorbed dose can be written as:

$$D = \int E \cdot \phi\left(E\right) \cdot \left(\frac{\mu_{en}\left(E\right)}{\rho}\right) dE. \tag{I.1}$$

Here E is the photon energy, $\phi\left(E\right)$ is the photon fluence, and $\left(\mu_{en}\left(E\right)/\rho\right)$ is the mass-energy absorption coefficient of the absorbing media. For medical applications of ionizing radiation the primary contributions to the mass-energy absorption coefficient are the photoelectric effect, Compton scattering, and $e^{-}e^{+}$ pair production. Figure I.1 shows the dependence of the mass-energy absorption coefficient of water on photon energy, and the energy regions where each of these three interactions dominate the photon interaction cross section.

Medical linear accelerators (linacs) used in radiotherapy produce x-ray beams specified by the electric potential used to accelerate electrons to a target, which is typically in

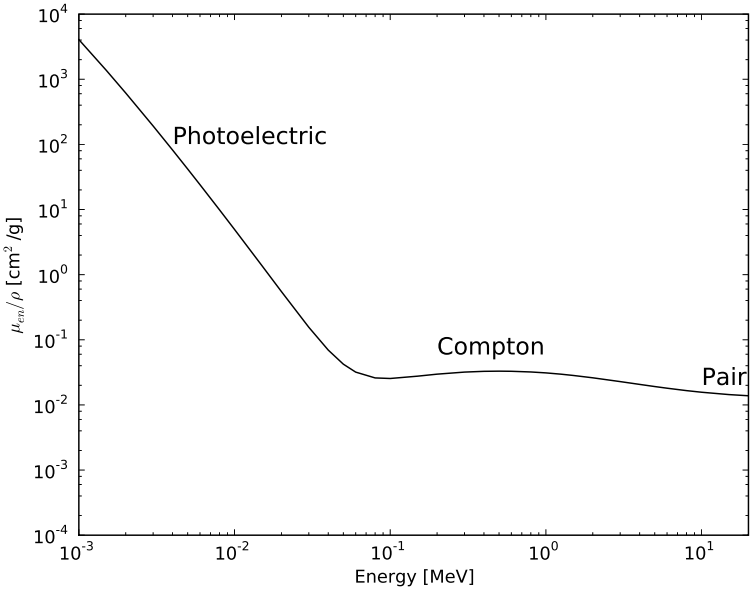

Figure I.1: Mass-energy absorption coefficient of water as a function of photon energy. The photoelectric effect dominates the photon cross section for energies less than about 20 keV. Compton scattering is the dominant interaction from this energy until about 20 MeV where pair production dominates. (Data from NIST [62])

the 4–25 MV range. The average energy in MeV of the resulting bremsstrahlung radiation which makes up the treatment beam is roughly 3 times smaller than the accelerating potential. As seen in Fig. I.1, the dominant photon interaction in water at these energies is Compton scattering. Diagnostic imaging procedures, on the other hand, typically use kilovoltage x-rays since they provide greater contrast between the tissues in the body than megavoltage x-rays. This is largely due to the strong dependence of the photoelectric effect on the atomic number of the absorbing material. Fig I.2 shows the energy spectra for representative cone-beam computed tomography (CBCT) x-ray beams with maximum energies ranging from 60 to 125 keV.

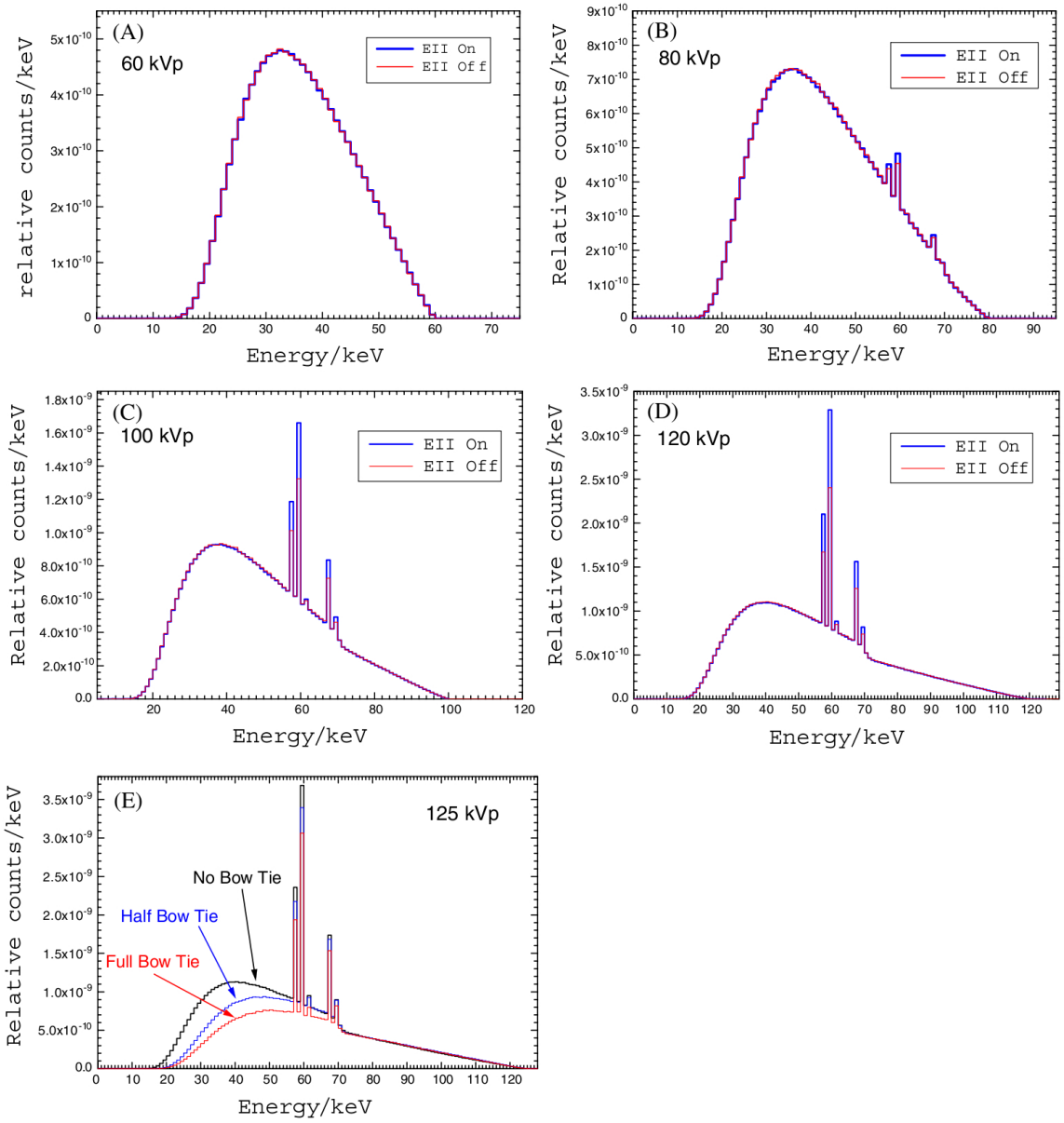

Figure I.2: Energy spectra of kV-CBCT x-ray beams with various accelerating potentials and filters. (Reproduced from [32] with permission)

I.1.3 Model-based convolution/superposition dose calculations

Therapeutic applications of radiation typically require radiation doses that are in general extremely high (on the order of tens of Gray) and precisely targeted. Consequentially, sophisticated model-based convolution/superposition dose calculation algorithms have been developed for clinical use that provide three dimensional dose distributions based on patient-specific anatomy and custom designed treatment fields. The basis of these techniques is to express the dose distribution as a convolution of the incident photon fluence with the spatial distribution of the energy deposited in medium due to photon interactions.

Figure I.3 shows the mass-energy absorption coefficients for bone and soft-tissue as a function of energy. In the therapeutic energy range the mass-energy absorption coefficient is nearly equivalent for all tissues in the body regardless of composition, and is roughly equivalent to that of water. This considerably simplifies dose calculation as the energy released due to the interaction of a photon field is independent of the atomic composition of the medium, and scales directly with density for a given photon fluence [63]. This simplification motivated the development of volumetric x-ray dose calculation methods in which the dose is calculated as a convolution of the photon fluence $\phi(\boldsymbol{r'}, E)$ and a dose deposition kernel $k(\boldsymbol{r} - \boldsymbol{r'})$ [13, 59]:

$$D(\boldsymbol{r}) = \iint \phi(\boldsymbol{r'}; E) \cdot k(\boldsymbol{r} - \boldsymbol{r'}; E)\, dV' dE. \tag{I.2}$$

The dose deposition kernels characterize the fraction of the energy released at $\boldsymbol{r'}$ that is absorbed at $\boldsymbol{r}$. Kernels are typically generated using Monte Carlo simulations in which photons are forced to interact at the center of a water calculation phantom and the spatial

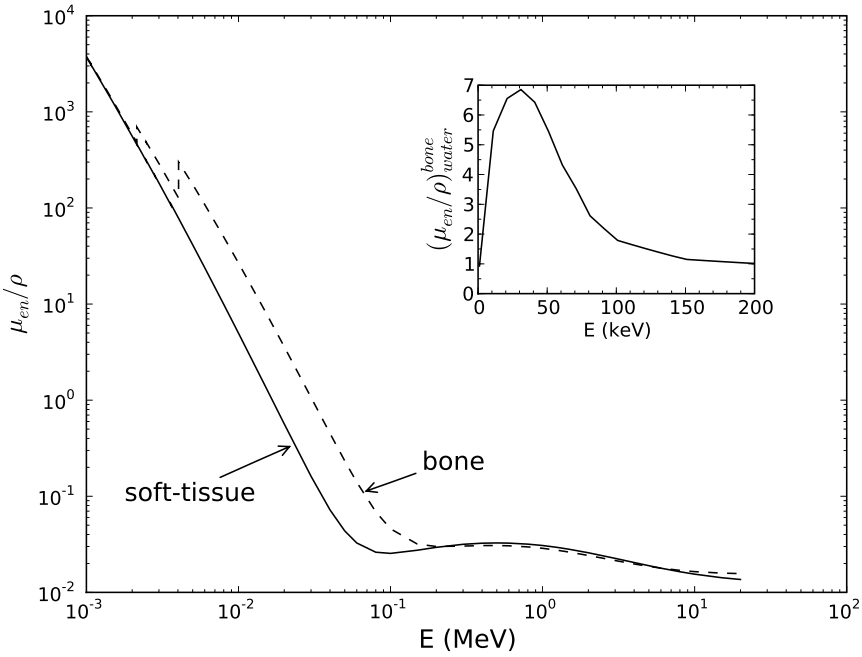

Figure I.3: Mass-energy absorption coefficients for bone and soft-tissue. The insert shows the quotient of the bone mass-energy absorption coefficient to that of water in the diagnostic energy range. (Data from NIST [62])

distribution of the deposited dose is recorded [58]. Due to the near equality of the mass-energy absorption coefficients of all tissues in the body at megavoltage energies, kernels generated in water are capable of describing the deposited dose distribution in all tissues from interactions with megavoltage energy x-rays.

In the model-based convolution/superposition approach, calculation of the radiation dose is performed in three steps: (1) modelling the treatment head and collimation systems of the linac to provide the incident fluence based on the the treatment plan [54, 68], (2) determining the x-ray fluence distribution in the patient, and (3) convolving the fluence with the dose deposition kernels. The first part of the calculation requires commissioning the x-ray beams delivered by the linac in a treatment planning system so that x-ray fluences can be determined for the treatment fields designed by the treatment planner. The commissioning process consists of performing extensive beam measurements including

percent-depth-dose curves, lateral beam profiles, and relative output factors as a function of field size, and supplying these data to the planning system to build the beam model.

The second part of the calculation requires detailed knowledge of the patient anatomy so that attenuation of the beam within the patient can be calculated. This data is obtained from CT images taken of the patient prior to radiotherapy specifically for the purpose of treatment planning. For megavoltage x-ray beams the necessary information to extract from the CT data is the distribution of electron densities within the patient. As a CT image is obtained from the absorption of x-rays within the body, it provides a three-dimensional map of the linear attenuation coefficients of the materials being imaged. Customarily, these values are reported as CT numbers or Houndsfield units, which are defined relative to the linear attenuation coefficient of water:

$$\text{CT Number} = \frac{\mu - \mu_{\text{H}_2\text{O}}}{\mu_{\text{H}_2\text{O}}} \times 1000 \tag{I.3}$$

To correlate the CT number with electron density, a CT number to density calibration curve is obtained for a CT unit by imaging a phantom consisting of various known materials and correlating the resulting CT numbers with the known densities of the materials (Fig. I.4). In convolution/superposition dose calculations the densities are used for attenuation of the primary beam and for scaling the length between an interaction site and dose calculation site, $\boldsymbol{r} - \boldsymbol{r'}$, in order to apply the dose deposition kernel to media with density inhomogeneities.

Model-based convolution/superposition algorithms have been shown to be highly accurate for megavoltage calculations in a wide variety of situations [7, 39, 41, 44, 55, 56]. Due to their accuracy and speed relative to other calculation methods they have become the standard approach to clinical dose calculation for external beam photon therapy.

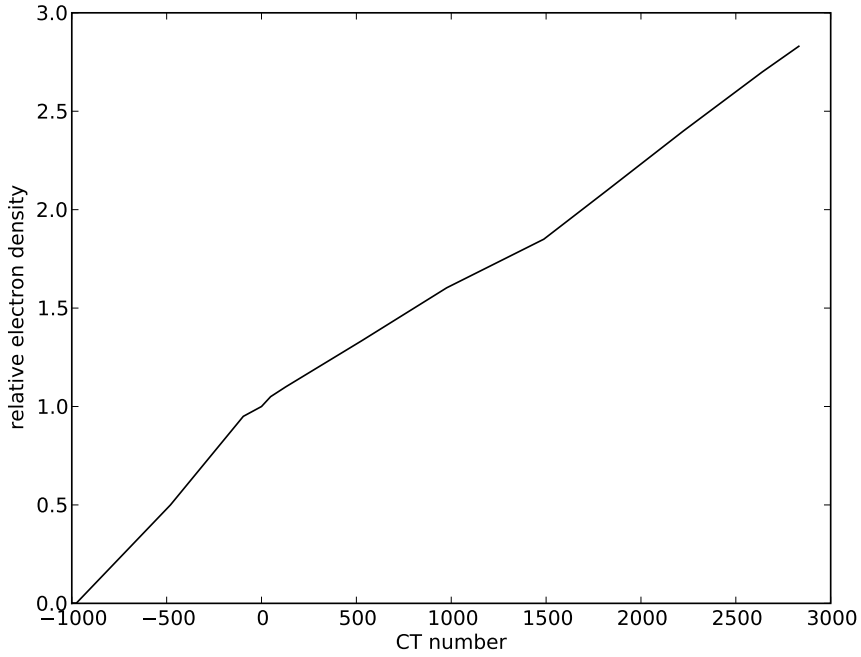

Figure I.4: Example of a CT number to electron density calibration curve used in a radiotherapy treatment planning system. The calibration curve was obtained for a 120 kVp beam from a GE LightSpeed® 16 CT scanner (General Electric Company, Fairfield, CT) using a GAMMEX 467® Tissue Characterization Phantom (GAMMEX, Inc., Middleton, WI).

These algorithms, however, are limited to megavoltage energies since the technique requires that the mass-energy absorption coefficients of the different absorbing media be equivalent. At kilovoltage energies, photoabsorption introduces a strong atomic number dependence on the photon interaction cross section. As Table I.1 shows, most materials in the body have similar effective atomic numbers; the atomic number of bone, however, is significantly higher than that of soft-tissues. This results in the enhanced mass-energy absorption coefficient of bone over soft-tissue that is seen in Fig. I.3 for photons in the kilovoltage energy range. Dose deposition kernels obtained in water calculation phantoms for kV x-rays are thus not be applicable in regions in or near bone.

To illustrate the shortcomings of the convolution/superposition technique for kilo-

Table I.1: Effective atomic numbers of tissues in the human body. (Data from [45])

Material	Effective Atomic Number
Air	7.6
Water	7.4
Muscle	7.4
Fat	5.9–6.3
Bone	11.6–13.8

voltage x-rays Figure. I.5 shows results of dose calculations performed for a kilovoltage cone-beam computed tomography scan of a pediatric head-and-neck patient with both Monte Carlo and model-based convolution/superposition techniques. The Monte Carlo calculation fully accounts for the photoabsorption of the x-ray beam as it travels through the skull of the patient. This leads to drastically increased dose to bone relative to the adjacent soft-tissue. The model-based calculation neglects photoabsorption and significantly underestimates the dose to bone. The dose to soft-tissues is overestimated with this technique since the calculation does not account for the reduced x-ray fluence in the body due to photoabsorption in bone.

I.1.4 Overview of the new algorithm

To extend the applicability of model-based dose calculation algorithms to the calculation of dose from kV x-rays it will be necessary to account for the perturbations to the calculated dose distributions due to medium-atomic number dependent effects. The new radiation dose calculation that we develop for kilovoltage energy x-rays calculates the radiation dose-to-medium including the effects of photoabsorption in bone in two steps. First, the radiation dose-to-water is calculated using a model-based convolution/superposition technique. This calculation utilizes a newly introduced, empirically parameterized scatter dose kernel, and accounts for density inhomogeneities in the calculation volume with a newly developed kernel-scaling approach. This calculation ignores medium atomic number

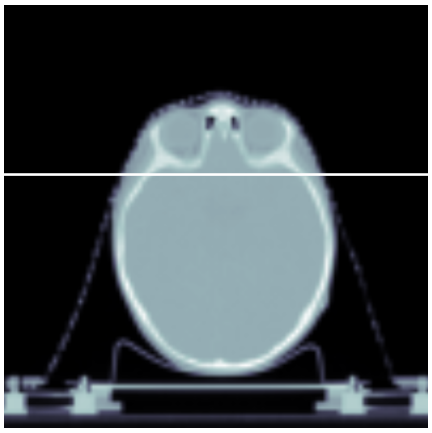

(a) Pediatric head-and-neck CT.

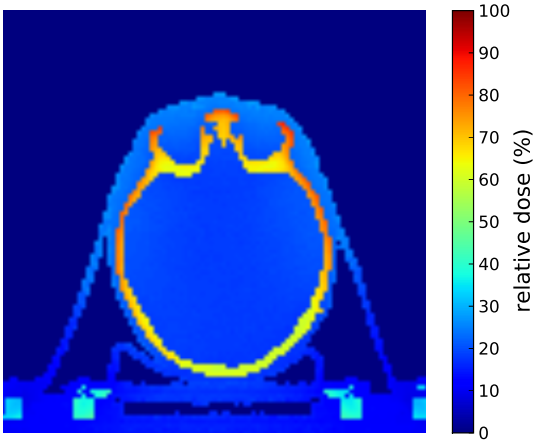

(b) Monte Carlo

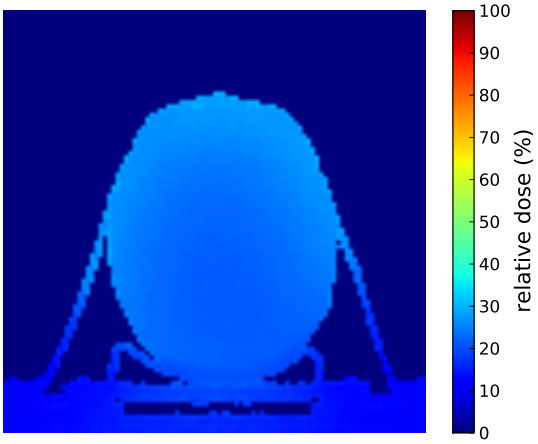

(c) Model-based

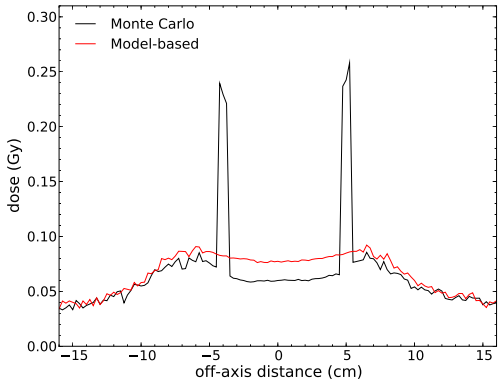

(d) Dose profiles along the line in (a).

Figure I.5: (a) An axial slice through a pediatric head-and-neck CT scan. (b and c) Axial dose planes in colorwash calculated for a CBCT scan taken for this patient with Monte Carlo and model-based convolution/superposition. Dose was normalized to the maximum dose to the scanned body. (d) Horizontal dose profiles for the line in (a).

dependent effects. The development of the model-based dose-to-water calculation algorithm is presented in chapter II. The second step of the calculation is to account for the medium atomic number dependent effects by applying a medium-dependent correction factor distribution to the dose-to-water calculation. We develop two methods to obtain patient and procedure-specific medium-dependent correction factor distributions that are presented in chapter III. In chapter IV we combine the model-based dose-to-water calculation with the medium-dependent correction method to calculate the dose-to-medium to real patients from

kilovoltage x-ray imaging procedures.

I.2 Previous work in kV dosimetry

I.2.1 Radiation dose calculation methods in radiotherapy

Model-based convolution/superposition algorithms applied to kilovoltage x-rays

Addressing the need for model-based imaging dose calculations, Alaei, et al. have generated photon energy deposition kernels for kV x-rays and commissioned a kilovoltage x-ray unit [4–6], and later a kV-CBCT unit [3] in a radiotherapy treatment planning system. These authors introduced two methods to account for the increased absorption of the x-ray beam in bone. In [5] they introduced a modified CT number to density calibration curve that artificially enhanced the density of high CT number voxels. Modifying the CT number calibration effectively enhances Compton scattering in the high density regions of the patient. This increases the attenuation of the beam in bone, but does not accurately calculate the high dose regions in bone or compensate for the spectral changes of the beam as a result of photoabsorption. With this approach average dose calculation errors of 16% were reported, with maximum errors of up to 69% compared to measurements made with thermoluminescent dosimeters.

In [3], model-based dose calculations were performed for a kV-CBCT imaging procedure. In this work, dose calculation was performed with a standard CT number calibration. The resulting dose errors were up to -22% for soft-tissue measurement points and -72% in bone. To correct for the error in the bone calculation the authors retrospectively multiplied the bone dose values by the ratio of the mass-energy absorption coefficients of bone to water using the energy of the x-ray beam in air for reference. The corrected values

had errors of up to almost 29%. These results overestimated the measured values since the energy of the x-ray beam in air is less than if it had been attenuated in the body, giving a higher ratio of mass-energy absorption coefficients. This study illustrates the main difficulties in applying simple correction methods to calculate the perturbation of the model-based calculation due to medium-dependent effects: (1) it is difficult to determine the energy spectrum of the x-ray fluence at a given point in a patient in order to determine the proper ratio of mass-energy absorption coefficients to use for correction of bone dose; (2) the dose to soft tissues is affected by the reduced photon fluence resulting from photoabsorption of the x-ray beam in bone.

The studies presented here represent the only published applications of model-based convolution/superposition dose calculation techniques for kV energy x-rays.

Monte Carlo dosimetry for kilovoltage x-rays

The calculation of radiation dose from first principles is possible in a stochastic manner where the probability distributions for the photon and electron interactions in medium are used to simulate the trajectories and interactions of particles. This is the basis of the use of Monte Carlo techniques for radiation transport in which physical quantities are obtained statistically by averaging the contributions of a large number of simulated particles. Several general-purpose Monte Carlo software packages have been developed including EGSnrc [53], MCNP [20], and GEANT4 [1], of which EGSnrc has seen the most widespread application in radiological medical physics. Using this suite, the BEAM user code [68] was written to facilitate the simulation of medical linear accelerators, and the DOSXYZnrc user code [78] was developed for radiation dose calculations within Cartesian geometries, such as voxelized CT-based volumetric phantoms. These software packages have

been used extensively for benchmarking and calculating dose from the x-ray and electron beams from linear accelerators [27, 31, 71, 76] as well as the x-ray beams from kilovoltage x-ray sources [11, 23, 24, 28, 33, 38, 74, 77] and are considered the gold-standard in radiation dose calculation.

As an example of Monte Carlo kV dosimetry, Ding et al. carried out dose calculations for real patient CT-based volumetric phantoms irradiated with clinical kV-CBCT scans used in IGRT [28, 33]. It was found that the imaging dose to soft-tissue ranged from 1–10 cGy, and that of bone from 6–29 cGy per imaging procedure.

Although the theoretical feasibility of using Monte Carlo calculations in treatment planning systems has been previously demonstrated [9, 40, 52], these techniques have not seen widespread clinical implementation. The computational intensity of Monte Carlo simulation has, until recently, prohibited the use of this method for the accurate calculation of radiation dose within clinical time constraints.

Dosimetry for superficial and orthovoltage x-ray therapies

Therapeutic kilovoltage x-ray beams (called superficial or orthovoltage x-rays depending on the energy) are used in radiation therapy for the treatment of superficial lesions. The American Association of Physicists in Medicine (AAPM) protocol for 40–300 kV x-ray beam dosimetry is based on an air-kerma (Kinetic Energy Released in Matter) calibration [57]. This procedure calculates the dose to the surface of a water phantom from in-air ion chamber measuerments as

$$D_{w,z=0} = M N_K B_w P_{\text{stem, air}} \left[\left(\frac{\overline{\mu}_{en}}{\rho} \right)^{w}_{\text{air}} \right]_{\text{air}}, \tag{I.4}$$

where M is the free-in-air ionization chamber reading for an exposure of t seconds, N_K is the chamber-specific air-kerma calibration factor determined for the beam quality, B_w corrects

the dose for the lack of backscatter in the in-air measurement relative to the situation where there is a water-density medium at the location of the chamber, $P_{\text{stem, air}}$ is a correction factor that accounts for scatter from the chamber stem, and $[(\overline{\mu}_{en}/\rho)^{w}_{\text{air}}]_{\text{air}}$ is the mean ratio of mass-energy absorption coefficients of water-to-air averaged over the photon spectrum. This measurement provides the physicist with a dose rate which is used to calculate the length of exposure for each treatment to deliver a prescribed dose to the surface of a patient.

Knowledge of the 3D dose distribution from superficial and orthovoltage x-rays can be obtained by measuring beam profiles and percent depth-dose curves in water [61, 69], however, this does not take into account tissue inhomogeneities or patient specific anatomy. Measurements have shown that the presence of a high atomic number inhomogeneity reduces the dose to soft-tissue upstream and downstream of the inhomogeneity [21, 25, 26]. These perturbations depend on the atomic number of the inhomogeneity, the thickness and shape of the inhomogeneity, the the distance from the inhomogeneity, depth, and beam field-size, making it difficult to characterize *a-priori* the magnitude of the effects when determining an exposure time for superficial or orthovoltage x-ray therapy. Seuntjens and Ma [70] calculated dose conversion factors ($D_{\text{tissue}}/D_{\text{water}}$) and the effects of material on depth scaling for tissue dose calculations for kV x-ray beams using Monte Carlo techniques. They found that for soft-tissues the effects were small, however bone-dose conversion factors ranged from 0.3 to 1.7, and depth scaling factors varied from 1.7 to 7.7 in the energy range studied. This study was limited due to the lack of availability of patient dose calculations based on volumetric CT, and thus a general correction method for arbitrary geometry remained elusive.

I.2.2 Radiation dosimetry for diagnostic CT

Dosimetry techniques used in diagnostic radiology for CT have been developed for regulatory and quality assurance (QA) measures rather than for accurate patient specific radiation dose calculation. To this end, dosimetric specifications are geared towards characterizing the output of CT units. Patient dosimetry from these measurements requires extrapolation to patient and organ doses based on studies performed on reference phantoms. A key difference between diagnostic radiology and radiation therapy is that the radiation risk from diagnostic procedures is stochastic except for extraordinary cases and the probability of radiation induced cancer mortality from low-dose exposures is assumed to be proportional to effective dose. Therapeutic radiation, on the other hand, is delivered to levels exceeding the thresholds for non-stochastic sequelae such as erythema, epilation, and fibrosis. In order to minimize stochastic radiation risks it is important to ensure that CT units in diagnostic radiology are exposing patients to minimal radiation while obtaining diagnostically useful images. The metrics devised to evaluate dose from CT reflect this need.

The central concept in CT dosimetry for diagnostic applications is the Computed Tomography Dose Index (CTDI) [72] given as

$$\mathrm{CTDI} = \frac{1}{T}\int_{-\infty}^{+\infty} D_1(z)\,dz, \tag{I.5}$$

where T is the thickness of a single axial slice of the CT image, and $D_1(z)$ is the single slice dose distribution along the axial direction of the scanner. CTDI measurements of the dose profile are typically performed in phantom with a 100 mm cylindrical ion chamber, and

denoted CTDI_{100}. Phantom measurements are performed in two acrylic phantoms, a head phantom with a 16 cm diameter and a body phantom with a 32 cm diameter. As a single axial dose measurement does not uniquely specify the average dose to the irradiated volume, measurements are taken at the periphery ($\mathrm{CTDI}_{\mathrm{p}}$) and center ($\mathrm{CTDI}_{\mathrm{c}}$) of the phantoms and are combined to give a weighted average index:

$$\mathrm{CTDI}_{\mathrm{w}} = \frac{1}{3}\,\mathrm{CTDI}_{\mathrm{c}} + \frac{2}{3}\,\mathrm{CTDI}_{\mathrm{p}} \tag{I.6}$$

To account for helical CT acquisition, the quantity $\mathrm{CTDI}_{\mathrm{vol}}$ can be obtained by dividing $\mathrm{CTDI}_{\mathrm{w}}$ by the pitch, defined as the magnitude of table motion for one revolution of the x-ray tube around the table. Another quantity called the dose-length product (DLP) is obtained by multiplying $\mathrm{CTDI}_{\mathrm{vol}}$ by the length of the irradiated volume, and is directly related to the amount of radiation delivered to the patient. Commercial imaging units typically provide the user with DLP and $\mathrm{CTDI}_{\mathrm{vol}}$ estimates for performed scans [48].

A second fundamental quantity, energy imparted (ϵ), is the integrated energy deposited in a patient [47]:

$$\epsilon = \int \rho\,(\mathbf{r})\,D\,(\mathbf{r})\,dV, \tag{I.7}$$

where ρ is the mass density and D is the dose of the irradiated volume V. For a cylindrical phantom this can be estimated by obtaining the $\mathrm{CTDI}_{\mathrm{vol}}$ for an irradiated section and multiplying by the mass of the irradiated section.

Monte Carlo simulations have been performed on cylindrical and anthropomorphic phantoms to generate the ratio of effective dose to energy imparted (E/ϵ) for patients [8, 75]. These values can be multiplied by the energy imparted for a particular scan using information obtained in a measurement phantom to obtain an estimate of total body radiation

dose for a given procedure. Organ doses can be obtained in a similar manner by using Monte Carlo simulation to obtain organ dose normalized to a measurable quantity, such as the $\mathrm{CTDI_{vol}}$. These can be used in conjunction with CT unit specific measurements to provide an estimate of organ doses for the various settings of a CT unit [49, 50]. Energy imparted to effective dose conversion factors have been calculated by Atherton et al. [8]. In this work, the energy imparted to an anthropomorphic phantom from head, chest, and abdominal scans was calculated. These estimates are not patient specific and do not provide three-dimensional organ dose distributions, rather they provide estimated average doses to organs based on generalized anthropomorphic phantoms.

Since the development of these dosimetry techniques, CT units with multiple arrays of detectors have been introduced that produce radiation beams wider than the 100 mm ion chamber used for CTDI measurements. As such, several authors have called the utility of CTDI into question [12, 16, 36, 37, 42]. With cone-beam CT, this index is even less appropriate as the geometry of the dose profile is not well suited for measurement by a single cylindrical ion chamber. A new dosimetry formalism has recently been introduced that was designed to be applicable for arbitrary CT acquisition including helical and cone-beam irradiation [37]. The central concept of the new methodology for conventional CT is the equilibrium dose, D_{eq}, given by

$$D_{\mathrm{eq}} = \frac{1}{b}\int_{-\infty}^{\infty} D_1\left(z'\right) dz', \tag{I.8}$$

where b is the spacing between successive scans and $D_1\left(z\right)$ is the single axial rotation dose profile. The equilibrium dose is similar in concept to the CTDI, however, the measurement technique differs in that a thimble ionization chamber with an active length of 20-35 mm is used with an extrapolation method to integrate the charge collected for the entire single

slice dose profile.

Although the proposed new metrics are appropriate for quality assurance and acceptance testing of the wide array of CT equipment available, they do not provide patient specific organ dose estimates. Monte Carlo simulations could be used, as described above, to obtain equilibrium dose to organ dose conversion factors for mathematical phantoms, but a flexible calculation method based on individual patient anatomy is desirable, particularly in situations such as image-guided radiotherapy where organ doses could approach non-stochastic toxicity thresholds.

II An algorithm to calculate the dose to water equivalent media from kilovoltage energy x-rays

II.1 Introduction

In this chapter we develop the new model-based convolution/superposition dose calculation algorithm for kilovoltage energy x-rays. Model-based dose calculation algorithms are ubiquitous in radiation therapy treatment planning systems for megavoltage energy x-ray dose calculations. Studies by Alaei et al. [4–6] extended the capability of the Philips PINNACLE treatment planning system (Philips Medical Systems, Milpitas, CA) to calculate the radiation dose to patients from kilovoltage x-rays. In a more recent study this work was further extended to commission a kV-CBCT beam in the PINNACLE system [3]. This approach utilizes existing calculation techniques designed for megavoltage x-ray beams to calculate the imaging dose from kilovoltage x-rays. The characteristics of dose deposition are, however, very different in these two energy regimes as the range of secondary electrons is negligible for kilovoltage x-rays, as opposed to megavoltage beams where the secondary electron range can be macroscopic. Additionally, as the fraction of interacting photons energy lost during a single interaction is relatively small, as is the mean path length of kV energy x-rays, photons may undergo multiple scattering processes before exiting or imparting all of their energy to the medium.

Motivated by the unique physical aspects of dose deposition from kilovoltage x-rays we have developed a new convolution/superposition algorithm for kV x-rays. The new algorithm calculates the radiation dose as the sum of primary and scatter components. Multiple approximations are implemented to simplify the scatter dose calculation; namely,

we introduce a simple, empirically parameterized monoenergetic scatter dose kernel, account for density inhomogeneities using a simplified global inhomogeneity correction, and ignore kernel tilting. These approximations allow for efficient calculation of the scatter dose convolution with the fast Fourier transform.

II.2 Methods

Model-based dose-to-water calculation

The dose to water is calculated by separately considering the dose deposited by primary and scattered photons:

$$D_w = D_p + D_s. \tag{II.1}$$

Since the range of electrons released by the interaction of a primary photon is negligibly small, the primary dose is equivalent to the collision kerma:

$$D_p(r) = K_c(r) = \int \phi_{p,E}(r) \cdot \left(\frac{\mu_{en,E}(r)}{\rho(r)} \right) dE, \tag{II.2}$$

where $\phi_{p,E}$ is the primary energy fluence, μ_{en} is the energy absorption coefficient, and ρ is the density of the absorbing medium. The subscript E indicates that each term in Equation II.2 is a function of energy. For polyenergetic clinical x-ray beams a typical approach is to discretize the energy spectrum and separately calculate the quantities in Equation II.2 for each energy bin. A key simplification in this work, however, is to treat the x-ray beam as if it were monoenergetic. As such, the primary dose can be written as

$$D_p(r) = c_p \cdot \phi_p(r) \tag{II.3}$$

where ϕ_p is the primary photon fluence, and c_p is a beam-specific primary fluence to dose conversion factor. c_p is obtained in this work by empirically fitting to Monte Carlo generated gold standard dose distributions. The primary fluence is obtained by propagating the incident photon fluence from an x-ray beam through the patient using the ray-tracing algorithm introduced by Siddon [73].

The dose from scattered photons is obtained by convolution/superposition of the primary photon fluence with a dose deposition kernel:

$$D_s\left(r\right) = c_s \int \phi\left(r'\right) \rho\left(r'\right) k\left(r - r'\right) dr', \tag{II.4}$$

where c_s is a beam-specific scatter dose conversion factor. The monoenergetic approximation is again used for the scatter component of the calculation. The kernel used in this work was parameterized as

$$k\left(r, \theta\right) = \frac{1 - \epsilon}{1 - \epsilon \cos\theta} \frac{Ae^{-a\overline{\rho}r} - Be^{-b\overline{\rho}r}}{r^2}, \tag{II.5}$$

where ϵ, the eccentricity, specifies the degree of forward peaking of the kernel, and θ is the angle between the incident primary photon velocity and the vector from the interaction point to a calculation point. The radial dependence of the kernel is motivated by the kernel used by Ahnesjö for megavoltage beams [2], and later extended by Carlsson and Ahnesjö to kilovoltage x-rays emitted from brachytherapy sources [22]. The parameters in Equations II.3, II.4, and II.5 were obtained by empirically fitting dose calculations to Monte Carlo generated dose distributions for simple geometric phantoms.

Density inhomogeneities are accounted for in the scatter dose calculation by scaling the distances in the exponential terms of the scatter kernel by an average density weighted

by the primary fluence distribution:

$$\overline{\rho} = \frac{\sum_{i,j,k} \rho\left(i,j,k\right) \cdot \phi_p\left(i,j,k\right)}{\sum_{i,j,k} \phi_p\left(i,j,k\right)}. \tag{II.6}$$

The weighted average density is calculated for each incident beam and scaled kernels are implemented separately for each beam. This approach to density correction is motivated by the prevalence of multiple scattering at kV energies which contributes to scattered photons sampling a potentially large area of the patient volume prior to depositing all of their energy in the medium or exiting the patient completely.

A further simplification of the scatter dose calculation is that we ignore the effects of divergence on the directionality of the scatter dose kernel. This amounts to defining the angle θ in Equation II.5 for all points as the angle that the line from the interaction point to the calculation point makes relative to the direction of incidence of the primary x-rays along the central axis of the x-ray beam. Figure II.1 shows a schematic depicting this approximation, which is referred to as neglecting kernel tilting.

By neglecting kernel tilting and accounting for density inhomogeneities in a global manner, i.e., scaling the distances in the dose deposition kernel with a single effective density for all points in the calculation volume, the scatter dose kernel becomes spatially invariant. This allows for the integral in Equation II.4 to be performed efficiently with the fast Fourier transform.

Monte Carlo calculation

Monte Carlo calculations were used to obtain the incident primary fluence profiles for several clinically relevant x-ray beams used for kV-CBCT, and gold standard dose distributions for simplified geometric phantoms irradiated by these beams. These distri-

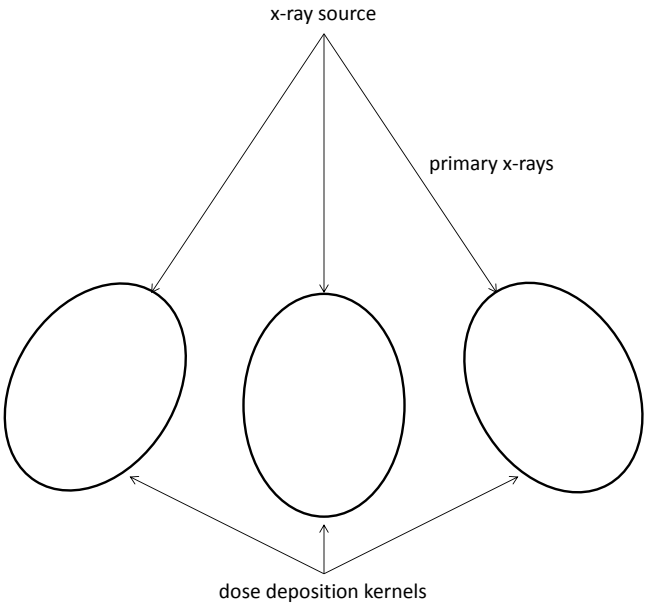

(a) Schematic depiction of a point kernel based dose calculation with tilted kernels.

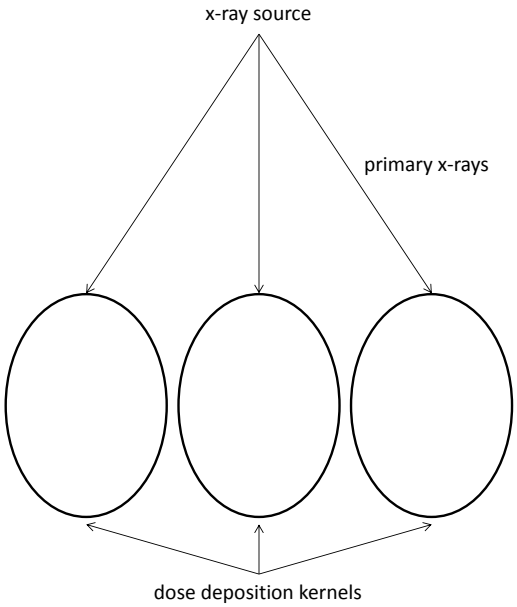

(b) Schematic depiction of a point kernel based dose calculation with non-tilted kernels.

Figure II.1: Kernel tilting is the process of accounting for divergence of the radiation beam by aligning the dose deposition kernel with the incident primary x-rays. This results in a spacially varying dose deposition kernel as shown in (a). By ignoring kernel tilting, (b), the directionality of the dose deposition kernels is assumed to be parallel to the direction of incidence of the primary photons at the central axis of the x-ray beam.

butions were used to empirically determine the model parameter values for the convolution/superposition dose-to-water calculation. Model parameters were obtained separately for each x-ray beam used. To test the resulting models we used Monte Carlo simulations to calculate the dose-to-water and dose-to-medium distributions for multiple real patient CT data sets with imaging sites including the head-and-neck (H&N), pelvis, and thorax. These results are presented in Chapter IV.

The Monte Carlo calculations in this study were performed as described by Ding et al. [28–30, 32, 34]. The x-ray beams were simulated using the BEAMnrc code [68], and dose calculations were performed with the DOSXYZnrc usercode [53, 78]. Dose-to-water calculations were performed by setting all materials in the calculation volume to water and scaling the density of each voxel according to a CT number to density calibration curve.

The simulated x-ray beams were from the Varian on-board imager (OBI) system integrated into a Trilogy^{TM}linear accelerator (Varian Medical Systems, Palo Alto, CA). Figure II.2 shows an example of the Trilogy^{TM}system and the orientation of the imaging x-ray apparatus relative to the treatment head and patient positioning table. The acquisition techniques used were the Varian OBI version 1.4 kV-CBCT x-ray beams denoted as standard-dose head, pelvis, and low-dose thorax, which were described by Ding et al [34]. Each of the kV-CBCT acquisition modes makes use of a bowtie filter. Bowtie filters are extrinsic filters placed on the x-ray tube to compensate for the shape of a patient. The bowtie filter is designed so that the thicker parts of the filter attenuate the x-ray beam that will irradiate thinner parts of a patient. The purpose of the filter is to ensure that a relatively uniform photon fluence irradiates the detector. The standard-dose head technique uses the full bowtie filter shown in Figure II.3, while the pelvis and low-dose thorax techniques use the half bowtie filter in Figure II.3. The x-ray energies for these kV-CBCT x-ray beams are

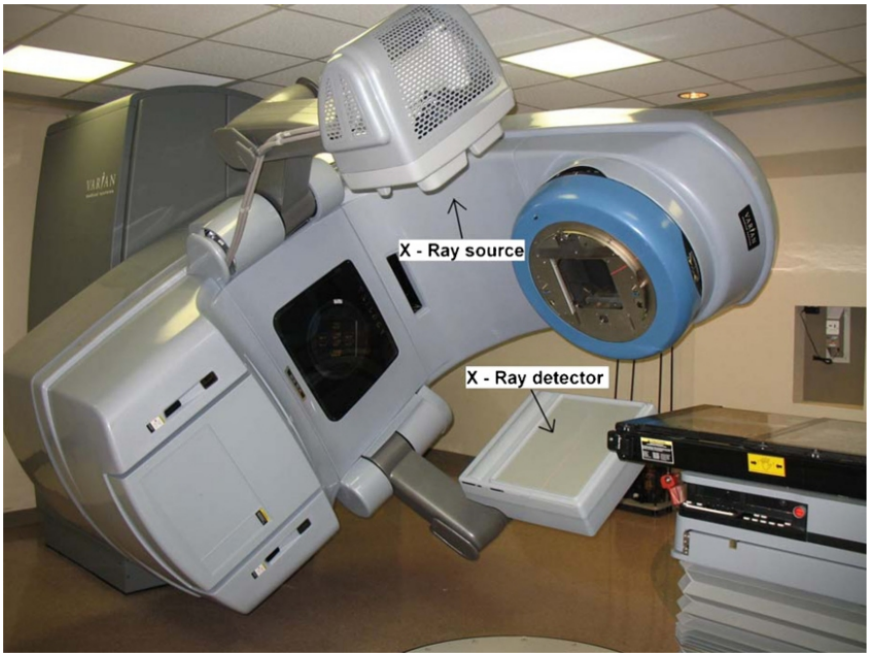

Figure II.2: Varian Trilogy with on-board imaging. The x-ray tube and detector are mounted at 90° from the treatment head and are only extended during kV imaging or CBCT procedures. This set-up enables acquisition of kV images or CT scans while the patient is in the treatment position immediately prior to treatment. (Reproduced from [32] with permission)

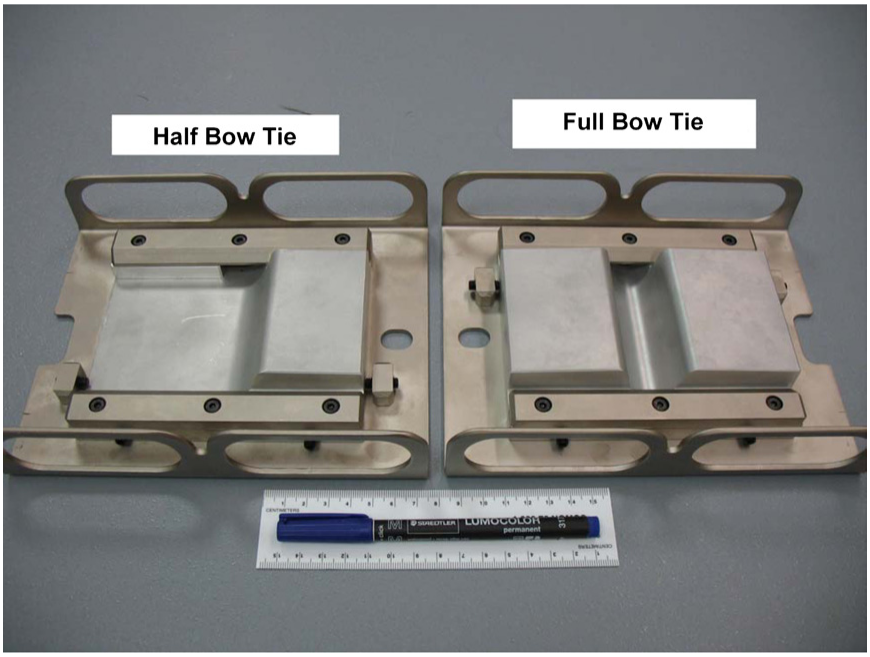

Figure II.3: Half and full bowtie filters placed in front of the x-ray source for kV-CBCT acquisition. (Reproduced from [32] with permission)

100 kVp for the head technique, 110 kVp for the thorax, and 125 kVp for the pelvis.

II.3 Results

The incident primary fluence profiles were obtained by simulating the x-ray beams used in this study using the techniques described above. The monoenegetic depth dependence of the fluence was empirically obtained by simulating the x-ray beams interacting with a phantom consisting of a narrow column of water, allowing for scattered photons to exit the phantom. This simulation was performed for x-rays along the central axis of the x-ray beam, thus neglected the effect of lateral energy differences on the depth dependence of the primary fluence. Figure II.4 shows fluence profiles for the pelvis, standard-dose head, and low-dose thorax x-ray beams used in this study. The shape of the fluence profile along the anode-cathode axis (X) is significantly affected by the bowtie filter used in the x-ray mode. The fluence is relatively constant in the patient superior-inferior direction (Z) as the bowtie filter is of constant thickness along this direction.

Figure II.5 shows the depth dependence of the photon fluence calculated for a phantom consisting of a narrow column of water placed 100 cm from the x-ray source. The narrow phantom ensures that scattered photons leave the calculation phantom and are thus not accounted for in the primary fluence profile. Density inhomogeneities are accounted for in the primary dose calculation by using the radiological depth to calculate the primary fluence in Equation II.3.

Dose calculations were performed for each x-ray beam with three simple, cubic water phantoms with dimensions of 10 cm per side, 20 cm per side, and 30 cm per side. A single incident x-ray beam normal to a surface of the cube was simulated for each configuration of beam type and phantom. These dose calculations were used to find model parameters for each beam by fitting the model-based calculation to the Monte Carlo results.

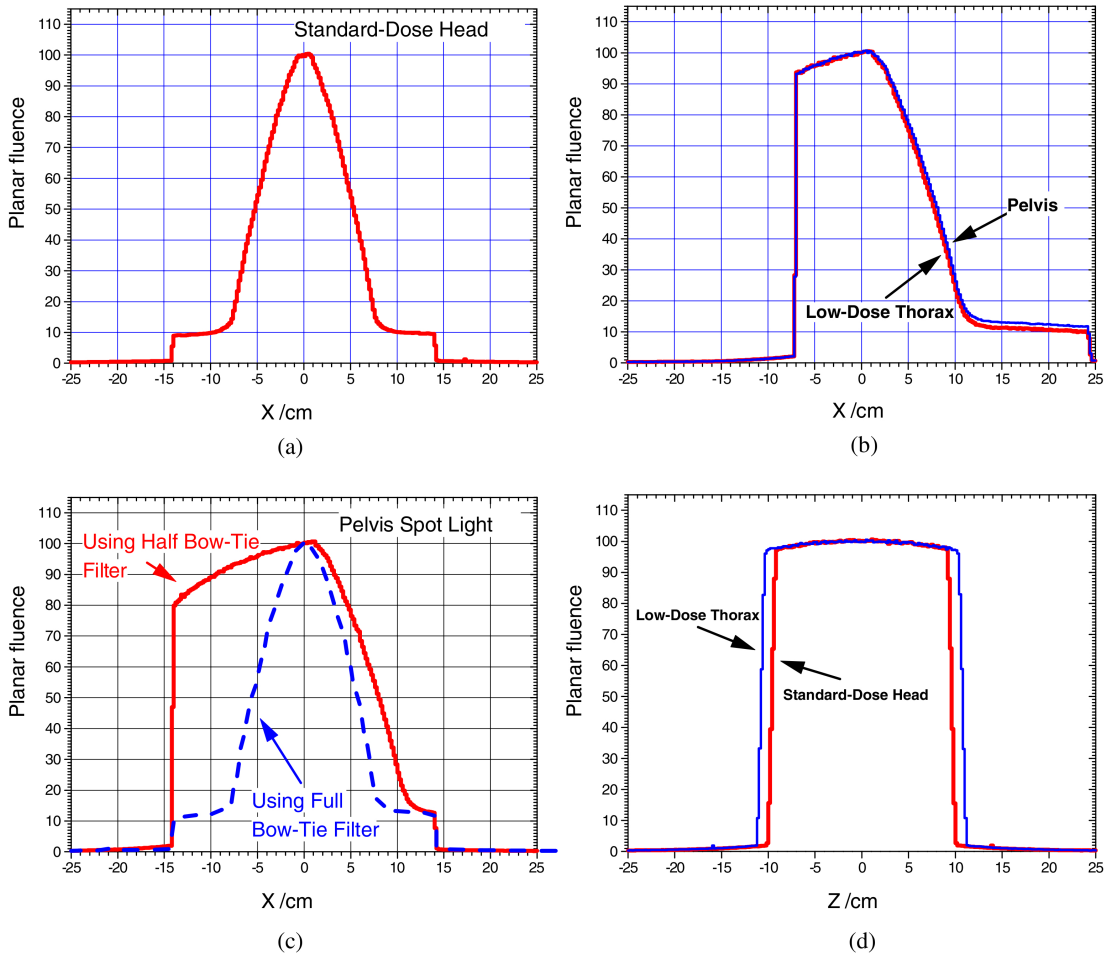

Figure II.4: Fluence profiles for the standard-dose head, pelvis, low-dose thorax, and pelvis spot light kV-CBCT x-ray beams taken at 100 cm from the x-ray source. (Reproduced from [29] with permission)

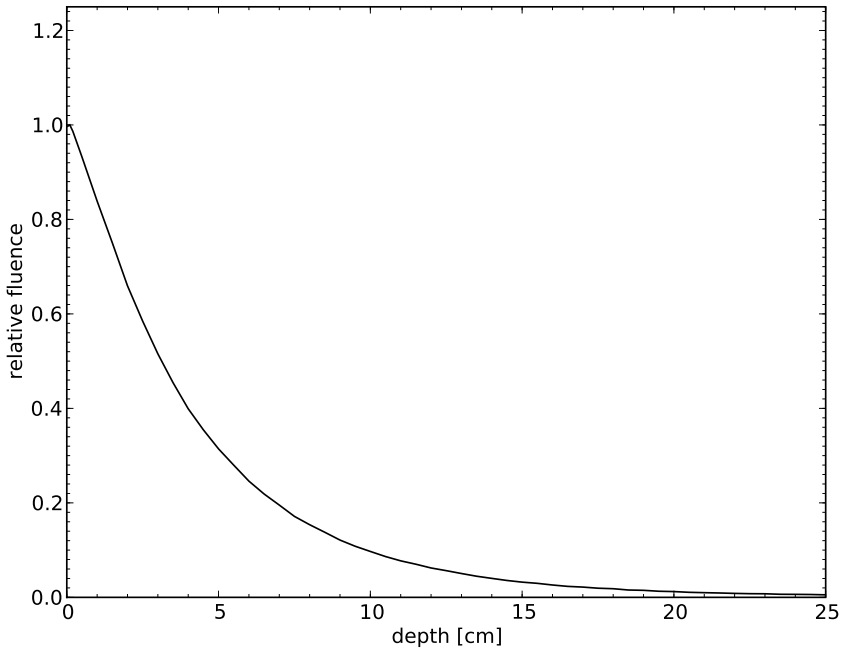

Figure II.5: The depth profile of the photon fluence simulated for a phantom consisting of a narrow water column placed 100 cm from the x-ray source.

We found that we could use the same kernel parameters for each x-ray beam, but adjust the ratio of the scatter dose conversion factor to the primary dose conversion factor (c_s/c_p) to fit each beam. Optimal values of this ratio were found to be 0.0081 for the pelvis technique, 0.0071 for the low-dose thorax, and 0.0059 for the standard-dose head. The kernel parameters resulting from the model-fitting procedural calculations are shown in Table II.1. Figure II.6 shows the radial dependence of the scatter dose kernel. The inverse square law has been removed from these plots by multiplying the kernel by r^2. The inverse square independent scatter kernel increases within a 5 cm radius as a result of using two exponential terms to parameterize the kernel in order to accurately model multiply scattered photons [22]. The inverse square law dominates the growth from multiple scatter, however, resulting in a monotonically decreasing function when this effect is taken into account.

Figure II.7 shows an example calculation using these model parameters to calculate

Table II.1: Model parameters for the empirical scatter dose kernel.

Parameter	Value
ϵ	0.5000
A	0.1194
a	0.1040
B	0.1037
b	0.3158

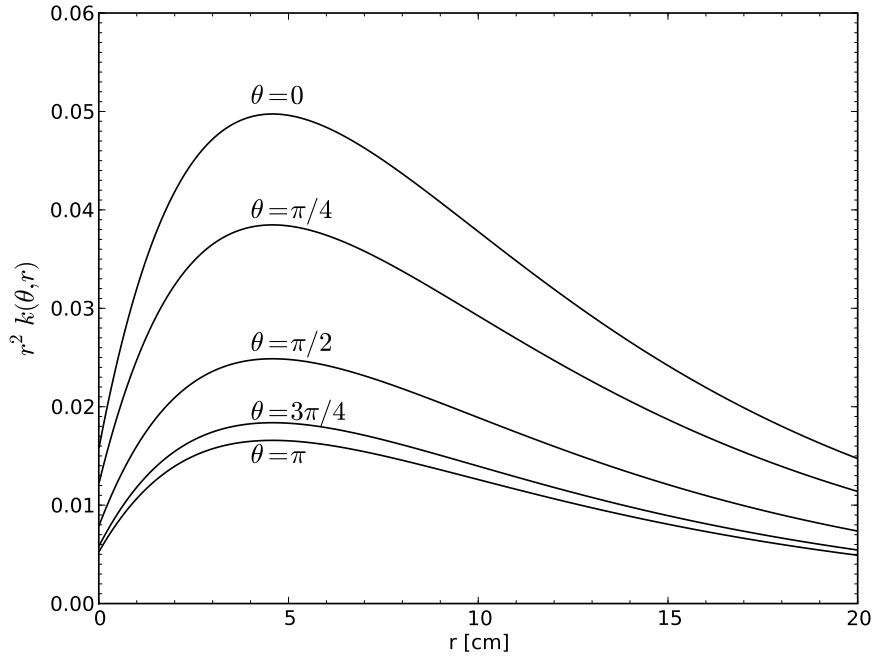

Figure II.6: Radial dependence of the scatter dose kernel for various angles from the direction of the incident photon to the voxel being calculated. The inverse square component of the kernel has been removed by multiplying the kernel by r^2.

the dose from the pelvis x-ray beam incident on the 30cm × 30cm × 30cm water phantom from above. The model calculation agrees well with the Monte Carlo calculation for this situation.

Figure II.8 shows example results for calculations performed using the standard-dose head x-ray beam incident on the 20cm × 20cm × 20cm phantom. Excellent agreement is found for the head x-ray technique as with the pelvis x-ray beam. The low-dose thorax x-ray beam is very similar to the pelvis x-ray beam so results for this technique are not

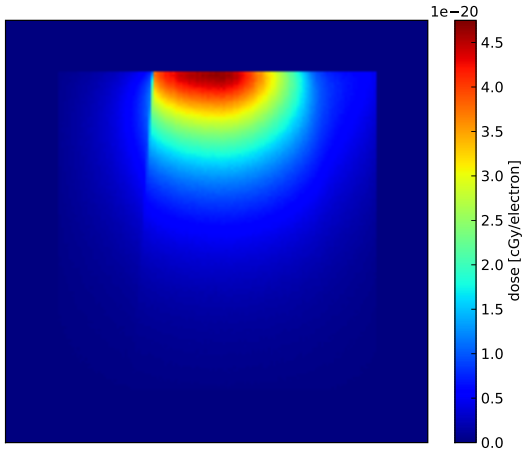

(a) Monte Carlo calculation dose-to-water distribution

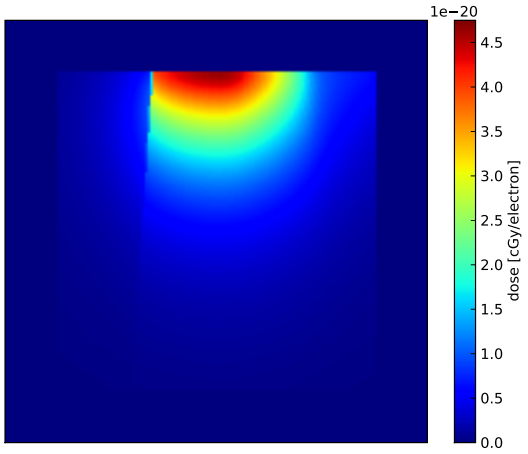

(b) Model-based calculation dose-to-water distribution

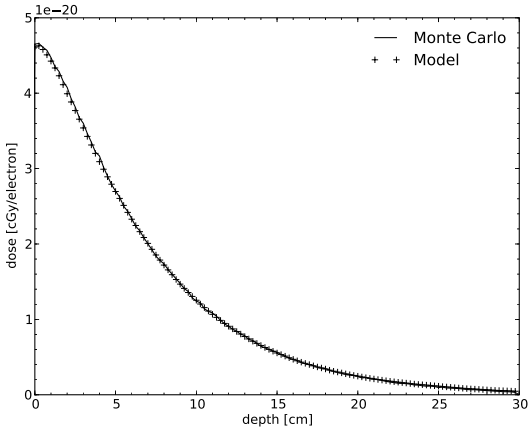

(c) Depth dose profiles

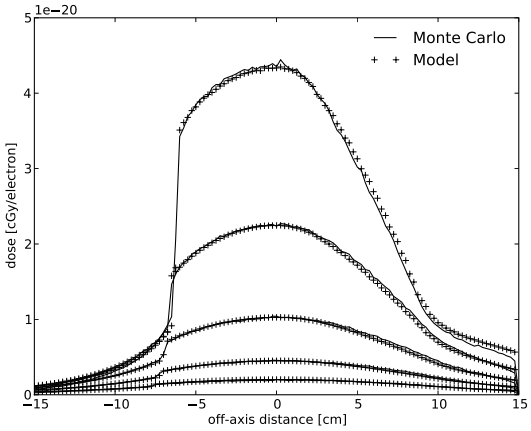

(d) Off-axis dose profiles

Figure II.7: Dose planes and profiles for calculations performed on a 30cm × 30cm × 30cm water phantom with the pelvis x-ray beam incident from above.

shown.

Figure II.9 shows the results of dose calculations performed with the pelvis x-ray beam irradiating the three different size water phantoms. Relative dose is presented with the dose for all calculations normalized to the maximum dose to the 30cm phantom as calculated by Monte Carlo. The difference in magnitude of the doses to each of the three phantoms is due to two factors: (1) all calculations were done with the center of the phantom placed 100cm from the radiation source so the dose at the surface for each calculation is scaled by the inverse of the square of the source-to-surface distance; (2) the larger phantoms result in an increase in the scatter dose as a larger volume is irradiated by the primary photon fluence and more energy is imparted to the phantom.

Figure II.9 illustrates a difficulty of applying model-based convolution/superposition algorithms to phantoms of varying sizes; namely that scatter kernels derived for scattering conditions present in a given volume phantom may overestimate or underestimate the scatter dose for calculations performed in smaller or larger volumes respectively. This is partially explained by the prevalence of multiple-scattering events which cause scattered photons to rescatter within the phantom and continue to deposit dose in the vicinity of the original interaction point. If a smaller phantom is used to derive a scatter kernel applied to calculations within a larger volume, then scattered photons that may have multiply scattered within the larger phantom do not contribute to the calculated scatter dose and the dose will be underestimated. Conversely, if a large phantom is used to derive a scatter kernel that is subsequentally applied to dose calculation in a small phantom, then photons that would have exited the small phantom without contributing to the scatter dose are now included in the calculation. This problem has been previously noted, and it has been recognized that scatter kernel generation in phantoms of comparable size to the dose cal-

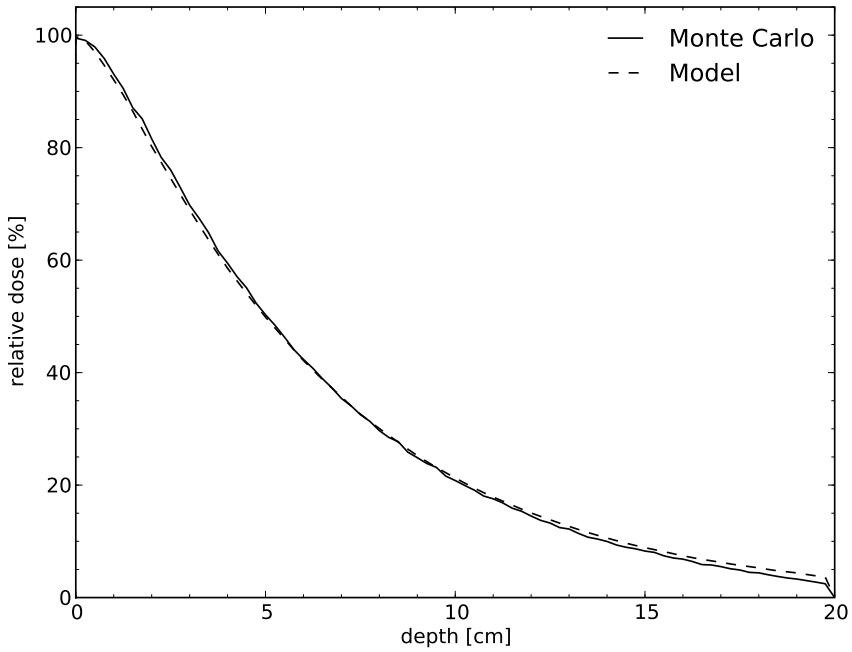

(a) Depth dose profiles for the standard-dose head x-ray beam

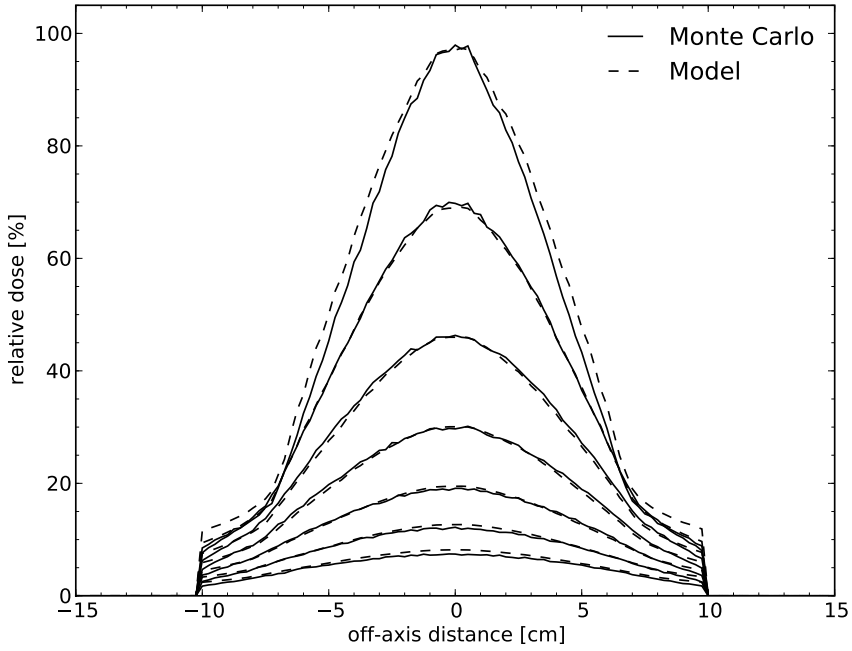

(b) Off-axis dose profiles for the standard-dose head x-ray beam

Figure II.8: Depth-dose curves and dose profiles for calculations performed on the 20cm water phantom irradiated by the standard dose head x-ray beam.

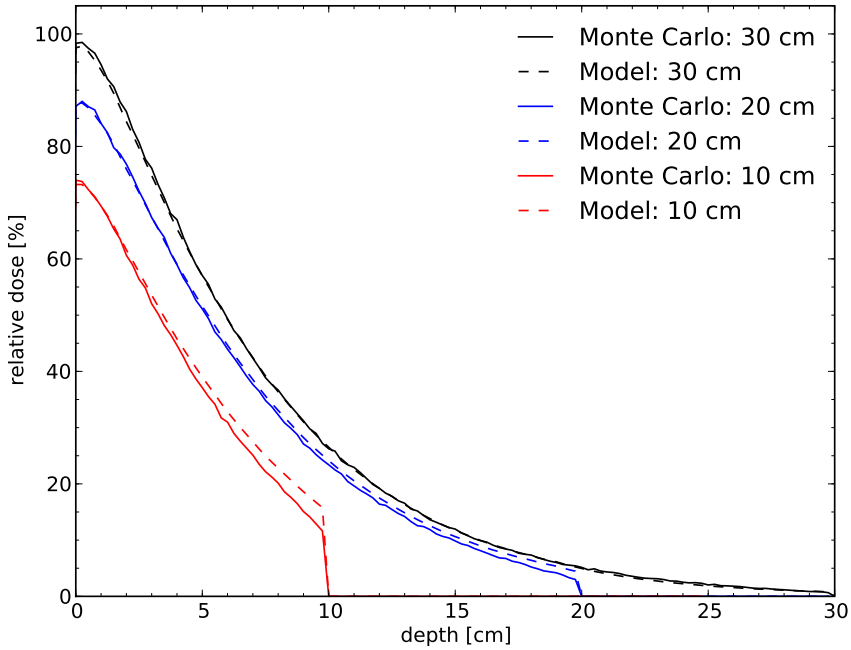

(a) Depth dose profiles for the pelvis x-ray beam irradiating each of the three simple cubic water phantoms

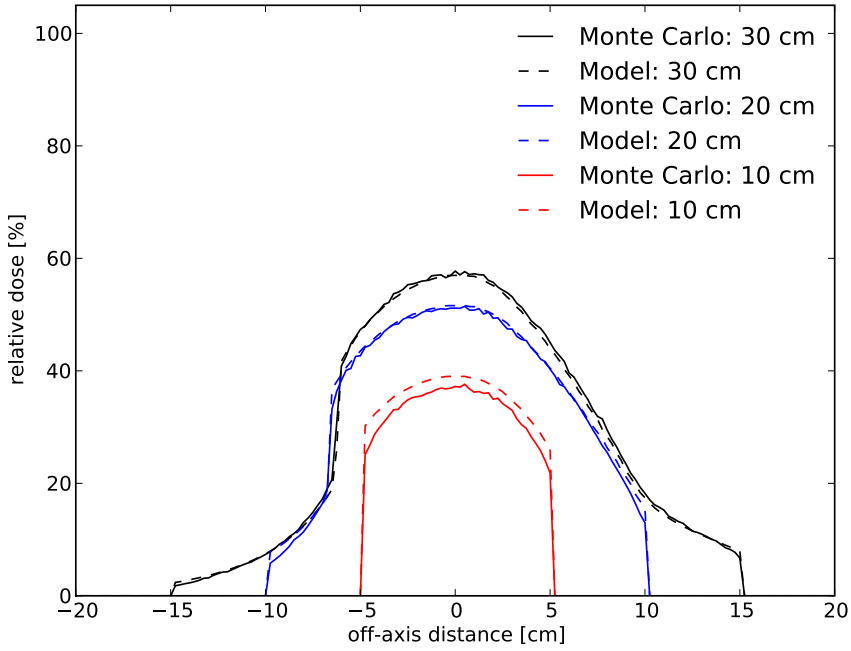

(b) Off-axis dose profiles at 5 cm depth for the pelvis x-ray beam irradiating each of the three simple cubic water phantoms

Figure II.9: Dose profiles for calculations performed on the 10cm, 20cm, and 30cm water phantoms irradiated by the pelvis x-ray beam from above.

culation volume may be advantageous [22]. We adopted this approach by determining the scatter kernel parameters that led to agreement between the model calculation and Monte Carlo calculations for the 20 cm phantom and the 30 cm phantom. As shown in Figure II.9, we were able to obtain accurate results for both of these phantoms using the same kernel parameters. This is at the expense of accuracy for the 10 cm phantom, which shows an overestimation of the dose at depth using our model. Our choice is justified, however, in that most clinical situations of significance involve the irradiation of volumes with dimensions generally greater than 10 cm.

Figure II.10 shows results of dose calculations performed with the pelvis x-ray beam incident on the 30cm phantom from an oblique angle. In these calculations the x-ray beam is diagonally incident on the phantom from the top right corner. Like the normally incident beam, the oblique x-ray beam results in high-dose areas at the surface of the phantom. The model-based calculation slightly overestimates the dose at the surface of the phantom due to overestimating the scatter dose in these regions. The explanation for this is similar to that for the 10 cm water phantom results shown in Figure II.9 as the model-based calculation assumes that there are full scatter conditions in the calculation volume, even if they do not exist. In this case, the oblique incidence increases the water-air interface which in turn reduces the contribution from laterally scattered photons to the scatter dose. The model-based calculation does not fully account for the lack of lateral scatter as the scatter dose deposition kernel implicitly assumes full scatter conditions.

To show the effects of low-density inhomogeneities on the dose calculation model similar calculations were performed for a second 30cm $\times$ 30cm $\times$ 30cm water phantom with a 10cm $\times$ 20cm $\times$ 20cm lung-density insert, as shown in Figure II.11. Calculations were performed for an x-ray beam incident normal to the surface from above the phantom.

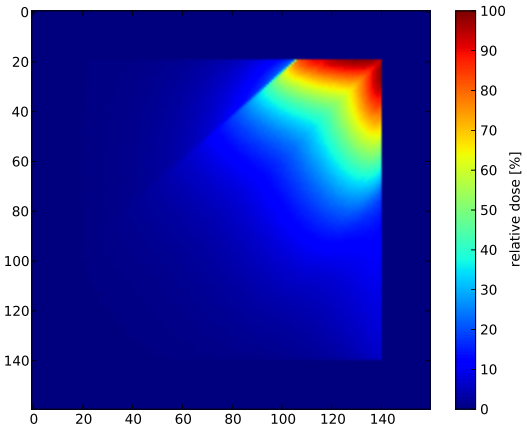

(a) Monte Carlo dose plane

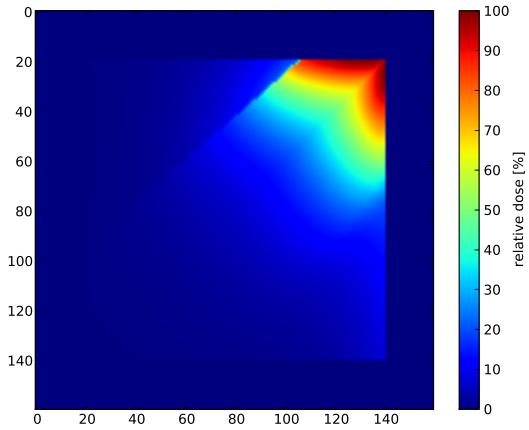

(b) Model-based dose plane

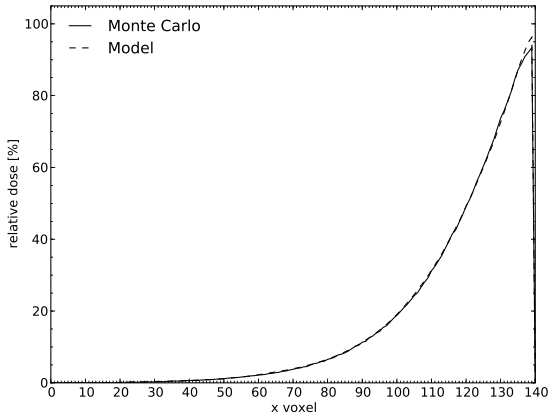

(c) Depth-dose profile along the diagonal

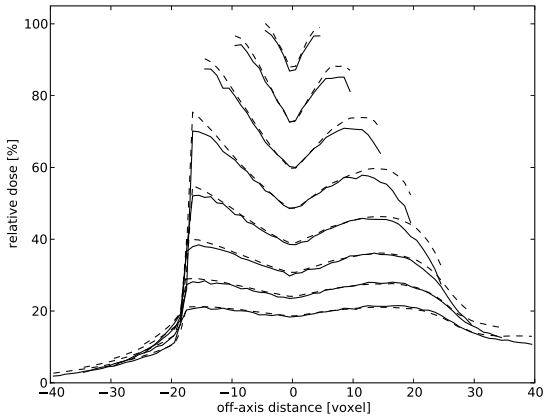

(d) Off-axis profiles at varying depths

Figure II.10: Dose calculations performed for the 30cm water phantom irradiated obliquely by the pelvis x-ray beam. The beam is incident from the top right corner of the phantom. Monte Carlo (solid) and Model-based (dashed) dose profiles are shown along the central axis of the beam (bottom left) and along lines perpendicular to the central axis of the incident x-ray beam for various depths (bottom right).

The dose calculation results shown in Figure II.11 are for the pelvis x-ray beam. The model-based calculation used the scaled kernel method with a calculated effective density scaling factor of 0.72. Good agreement is seen between the dose calculations both in the lung-density, and in the water-density portions of the calculation volume.

Figure II.12 compares these results to those obtained using the model-based calculation without kernel scaling, i.e., setting $\overline{\rho} = 1$. The depth-dose curve shows that the effect of scaling the kernel is to enhance the dose in the low-density region, whereas the dose to the water-density region is not significantly affected by scaling the kernel. Note that both calculations overestimate the dose in the water density region immediately upstream of the first water-to-lung interface. This is due to the model incorrectly modeling the lack of backscattered photons from interactions in the lung-density material.

The inhomogeneity correction method employed in this work differs from typical approaches employed in radiotherapy treatment planning systems using a point-kernel convolution. For example, the most common of these approaches, the collapsed-cone algorithm [2], scales the dose deposition kernel separately along rays emanating from an interaction point according to the densities of voxels along each ray. This approach assumes that scattered photons transfer energy to the absorbing medium rectilinearly from their point of origination until all of their energy is deposited in the medium.

As this approach is successfully implemented in commercial radiotherapy treatment planning systems, we seeked to compare results obtained using a similar calculation to results obtained using our scaled kernel method. To accomplish this comparison we developed a second scatter dose convolution algorithm that, similar to the collapsed cone method, scales the scatter kernel along rays emanating from an interaction point according to the densities that each ray intersects.

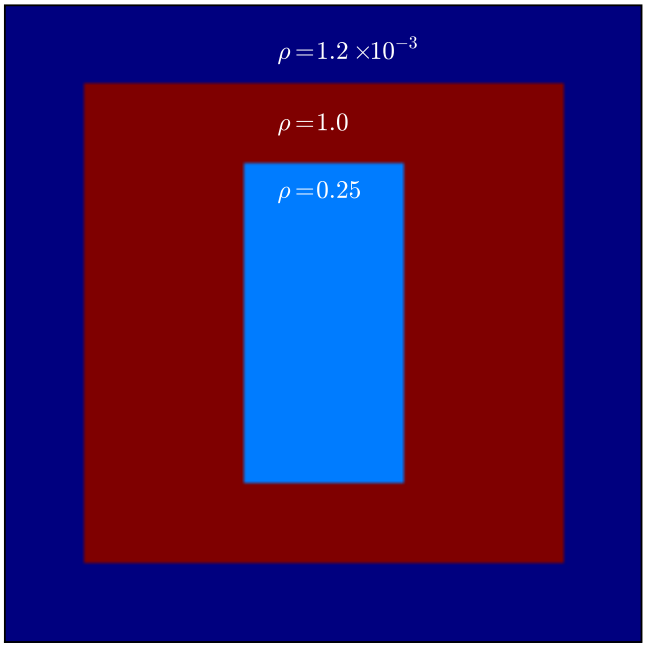

(a) Water calculation phantom with lung density insert

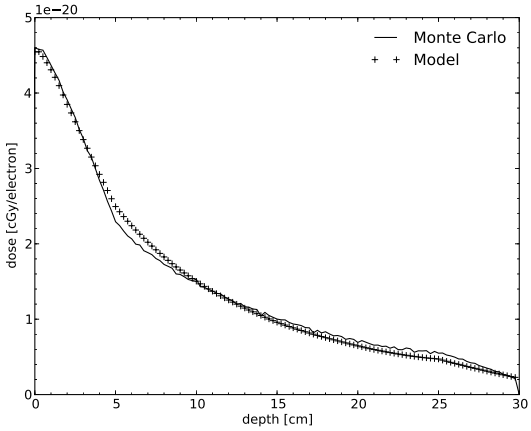

(b) Depth dose profiles

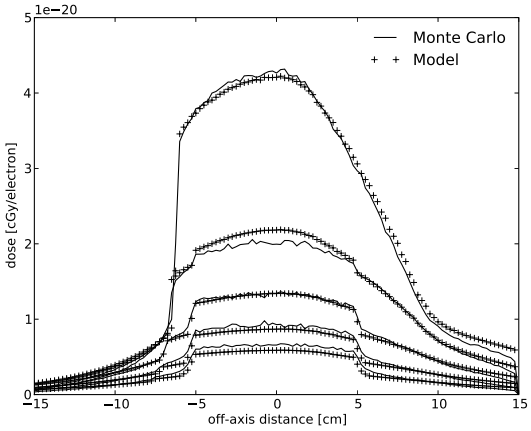

(c) Off-axis dose profiles

Figure II.11: Results for calculations performed for the Standard-Dose Pelvis x-ray beam incident from above on a 30cm×30cm×30cm water phantom with a 10cm×20cm×20cm lung density insert. The scaled kernel method was used for this calculation, with a kernel scaling factor of 0.72.

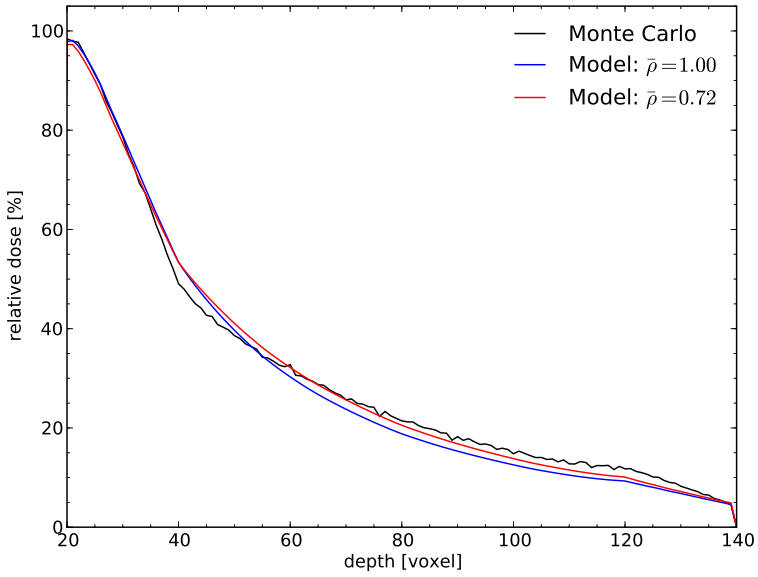

Figure II.12: Comparison of depth-dose curves between the model-based calculation with the effective density, $\overline{\rho}$, set to 0.72 as shown in Figure II.11, and with the effective density set to unity to show the effects of neglecting the inhomogeneity in the scatter kernel. Calculations were done on the same phantom as shown in Figure II.11. Voxels are of dimension 0.25 cm in each direction.

The basis of this calculation, like our scaled kernel method, is to first propagate the primary fluence through the patient using the densities of the patient to attenuate the beam. Once the primary fluence is known, the convolution in Equation II.4 is calculated by explicit summation:

$$D_s\left(l,m,n\right) = c_s \sum_{i,j,k} \phi\left(i,j,k\right) \rho\left(i,j,k\right) k\left(RPL_{i,j,k\rightarrow l,m,n}\right), \tag{II.7}$$

where $RPL_{i,j,k\rightarrow l,m,n}$ is the radiological path length from voxel (i,j,k) to voxel (l,m,n). A simplification made in our implementation of this algorithm was to only evaluate RPL along a finite number of rays emanating from an interaction point. This was done by defining rays using sets of discrete polar and azimuthal coordinates (θ_i, φ_i) defined relative to the vector from the radiation source to the interaction point. Ray tracing was then performed along

each ray to obtain tables of RPL versus physical path length L for each ray. To obtain the RPL for an arbitrary voxel (l, m, n) at a position not along one of these rays, the physical distance between that voxel and the interaction point is calculated:

$$L = d \cdot \sqrt{(i-l)^2 + (j-m)^2 + (k-n)^2}, \tag{II.8}$$

where d is the dimension of the isotropic voxel, and the table of RPL versus L for the ray closest to voxel (l, m, n) is used to look up the value of RPL.

This algorithm was slow to implement in practice as the number of operations required for a calculation volume of dimension N^3 is of the order of N^6. This is in contrast with the fast Fourier transform in which the number of operations is proportional to $(2N)^3 \cdot \ln 2N$ [2]. This limited calculation using this approach to just a few simple cases. We first showed that we could duplicate the results seen in Figure II.7 with this approach as the two models should yield identical results for a homogeneous water phantom since the same scatter kernel was used for each calculation. Upon validation, we tested the approach for inhomogeneity correction by performing calculations on the phantom seen in Figure II.11 for the same situation in which a single x-ray beam is incident from above. Figure II.13 shows these results and how they compare to Monte Carlo and the scaled kernel method. In these graphs, the black lines are the Monte Carlo calculation, the red lines are the scaled-kernel method using a kernel scaling factor of 0.72, and the green lines are the results for the second kernel-based method with density scaling along rays emanating from the interaction point. The scaled kernel method is shown to be only slightly less accurate than the method in which scaling is done for rays originating from the interaction point. In light of the significant difference in calculation time we feel that the slight loss in accuracy in using the scaled kernel method is acceptable.

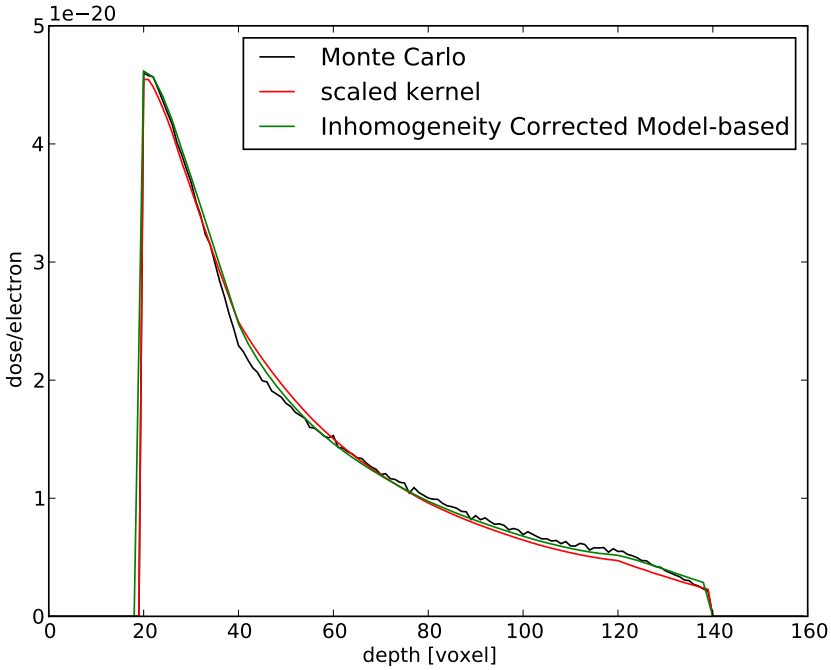

(a) Depth-dose curves

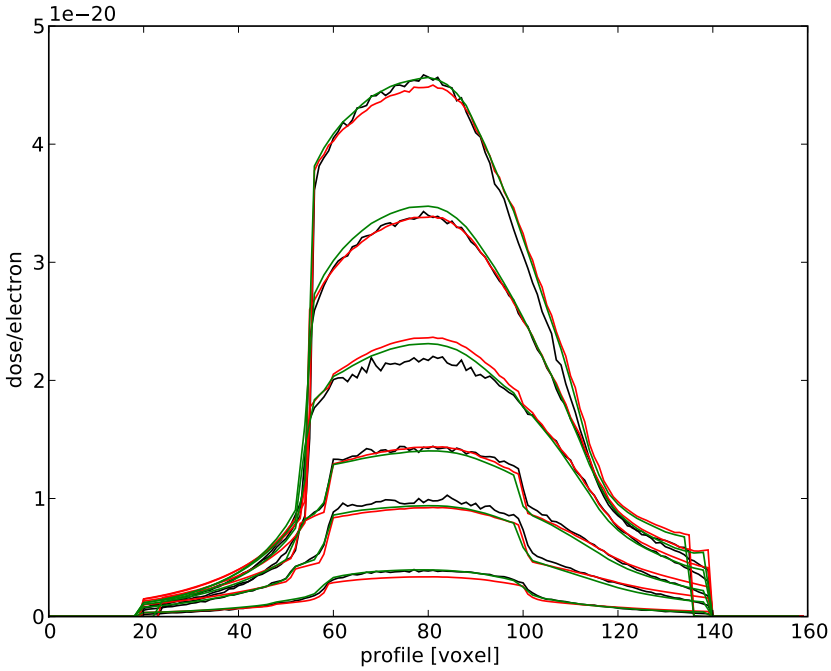

(b) Off-axis dose profiles

Figure II.13: Comparison of the scaled kernel method (red) vs. an inhomogeneity corrected model-based dose calculation where density scaling is performed along rays emanating from each interaction point (green). The phantom used for calculation is the same as shown in Figure II.11. Voxels are of dimension 0.25 cm in each direction.

II.4 Discussion and conclusions

We have presented a new model-based convolution/superposition dose calculation algorithm for kilovoltage energy x-rays and have employed the algorithm to calculate the dose-to-water for simple geometric phantoms from kV x-rays. The new technique employs multiple simplifications to exploit the physical characteristics of x-ray interactions at the kilovoltage energy range: 1) the x-ray beam is approximated as monoenergetic; 2) kernel tilting is ignored; 3) density inhomogeneities are accounted for in a global manner by scaling the scatter kernel for each individual beam by an average patient density. The monoenergetic approximation eliminates the need for multiple scatter dose convolutions to be performed for different energy bins, while the use of an invariable kernel for each beam enables the scatter dose convolutions to be performed with a fast Fourier transform. While these approximations may introduce additional error in the dose calculation relative to a more sophisticated algorithm, we found the dose calculations to be within acceptable accuracy for the simple phantom calculations performed in this chapter. The results of dose-to-water calculations for real patients irradiated with kV x-rays will be presented in chapter IV.

In the following chapter we develop the methods to determine medium-dependent correction factors for patient-specific and procedure-specific dose calculations for kilovoltage x-rays. The correction method will be used in conjunction with the model-based dose-to-water calculation developed here to calculate dose-to-medium distributions for real patients. These results will be presented in chapter IV.

III Methods to account for medium-dependent effects in kilovoltage energy x-ray dose calculations

III.1 The direct approach to medium-dependent correction

III.1.1 Introduction

In the previous chapter we developed a new model-based dose calculation algorithm for kilovoltage x-rays. Model-based dose calculations, however, have known deficiencies for kV x-rays in regions in or near bony anatomy since photoabsorption in bone leads to large differences between dose-to-medium and dose-to-water [5, 6, 33, 35]. To account for medium-dependent effects, Alaei et al. used a simple correction method based on multiplying the dose to bone voxels by the ratio of the bone-to-water mass-energy absorption coefficients [3]. This method was shown to be inaccurate as it is difficult to characterize *a priori* the energy spectrum at a given voxel for complicated geometries, such as volumes based on patient CT data. Furthermore, this method fails to correct the dose to soft tissues in the vicinity of bone that are irradiated by a reduced fluence relative to the model-based dose-to-water calculation.

To overcome the deficiencies of model-based calculations for kilovoltage dose calculation, an empirical correction based algorithm, the medium-dependent correction–direct-approach (MDC-DA), is developed [35]. This algorithm considers both medium-dependent effects and electron density effects by applying a correction factor matrix that accounts for the effects of photoabsorption in bone on the dose distribution obtained using a model-based dose calculation. The correction factor matrix is obtained by use of an empirical param-

eterization of the medium-dependent correction factors. In this section we introduce this method and validate the accuracy of the MDC-DA to calculate the radiation dose delivered to patients imaged with kV-CBCT for alignment prior to radiotherapy by comparing dose distributions calculated with the MDC-DA to Monte Carlo calculations.

III.1.2 Methods

Algorithm overview

The MDC-DA algorithm calculates the dose-to-medium by applying a correction factor, $MDC\,(x,y,z)$, to a dose-to-water matrix:

$$D_{\text{medium}}\,(x,y,z) = MDC\,(x,y,z) \times D_{\text{water}}\,(x,y,z)\,. \tag{III.1}$$

The dose-to-water calculation may be performed using a model-based method or by Monte Carlo simulation in which all media is set to water with density scaled to that of the actual media.

The matrix $MDC\,(x,y,z)$ is obtained by considering sets of parallel rays, called correction fields, incident on the patient from a discrete set of angles, θ_i, about the imaging isocenter. The distribution of incident correction fields depends on the geometry of the image acquisition. For example, the kV-CBCT x-ray beams simulated in this work irradiate the patient in either a half-fan mode, or a full-fan mode. The half-fan acquisition technique is used to image larger volumes. This is done by irradiating roughly half of the patient at a time, covering the entire patient by making a full 360° rotation with the x-ray source in order to reconstruct the full volume. The full-fan acquisition technique is used for smaller volumes such as a head. For this technique, the entire volume is irradiated by the x-ray

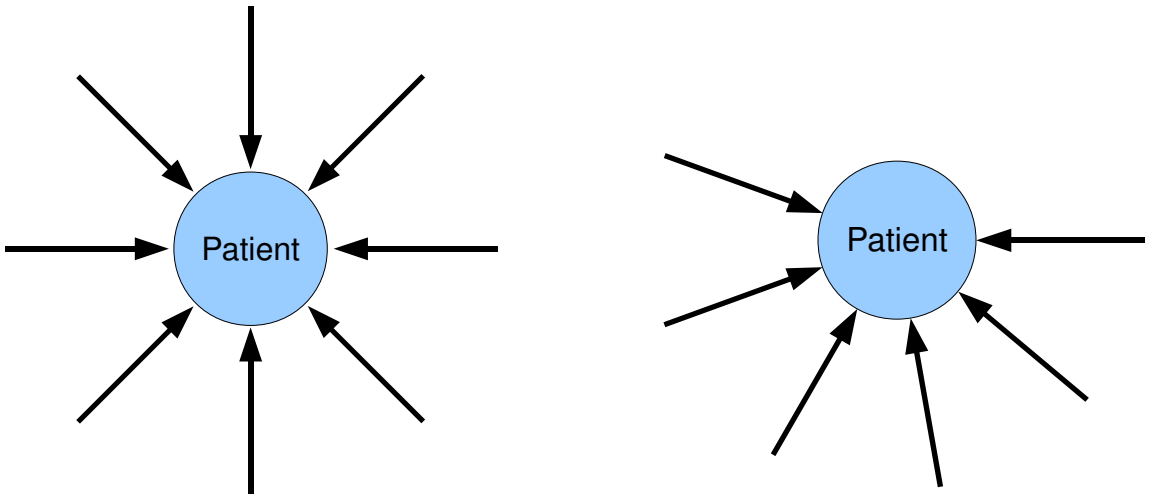

(a) Half-Fan (b) Full-Fan

Figure III.1: The rotation of the x-ray source around the patient during tomographic imaging is modeled by applying sets of one-dimensional correction factors along rays incident on the patient from a finite number of angles. Half-fan beams were modeled with eight sets of incident rays evenly spaced and spanning 360° . Full-fan beams were modeled with six sets of incident rays of one-dimensional correction factors spanning 200° .

beam and a 200° rotation of the source is used. Figure III.1 illustrates the discretization of x-ray beams for correction factor calculations for these techniques.

The effects of bone on the dose distribution are accounted for by applying an empirically parameterized one-dimensional correction factor along each ray. The parameterization is based on the distribution of bone and soft-tissue that each ray intersects. In this manner, each correction field provides the medium-dependent correction factor for an x-ray beam irradiating the patient from the angle of incidence of the correction field. The total correction factor at a voxel is taken to be a weighted average of the individual contributions to that voxel from each correction field.

For each ray, which for notational convenience we will take to be incident along the x-direction for a given y, z, and θ_i, the correction factor, $MDC\,(x, y, z; \theta_i)$, is obtained

as

$$MDC\left(x,y,z;\theta_i\right)=\prod_j \alpha_j\left(x,y,z;\theta_i\right)\times\beta_j\left(x,y,z;\theta_i\right)\times\gamma_j\left(x,y,z;\theta_i\right) \tag{III.2}$$

where α, β, and γ correct for the upstream, in-bone, and downstream effects of bone on the dose distribution respectively. The product in Equation III.2 is over each bone that the ray intersects, bounded by $x_j^1\left(y,z;\theta_i\right)$ upstream and $x_j^2\left(y,z;\theta_i\right)$ downstream.

This parameterization was motivated by studying the medium-dependent correction factors for kV x-ray beams incident on simple slab-geometry virtual phantoms. For example, Figure III.2 shows the correction factor along the central axis of a kV-CBCT beam incident on a simple water phantom with a 2 cm slab of bone. The correction factors were obtained using Monte Carlo simulations in which dose-to-medium and dose-to-water were calculated separately for this beam interacting with the phantom. The multiplicative correction factor needed to convert the dose-to-water to dose-to-medium is then the ratio

$$MDC\left(x,y,z\right)=\frac{D_{\text{medium}}\left(x,y,z\right)}{D_{\text{water}}\left(x,y,z\right)}. \tag{III.3}$$

The x-ray beam is incident from the left, and is traveling left to right in this graph. The blue and white sections below the graph depict the distribution of water and bone in the phantom, respectively. There are three distinct regions in the correction factor distribution–upstream, in-bone, and downstream–with the in-bone region evidenced by the large (>2) correction factors resulting from increased photoabsorption in bone relative to water.

The upstream correction accounts for the decrease in the backscattered photon fluence at points upstream of bone due to increased absorption of these photons in bone

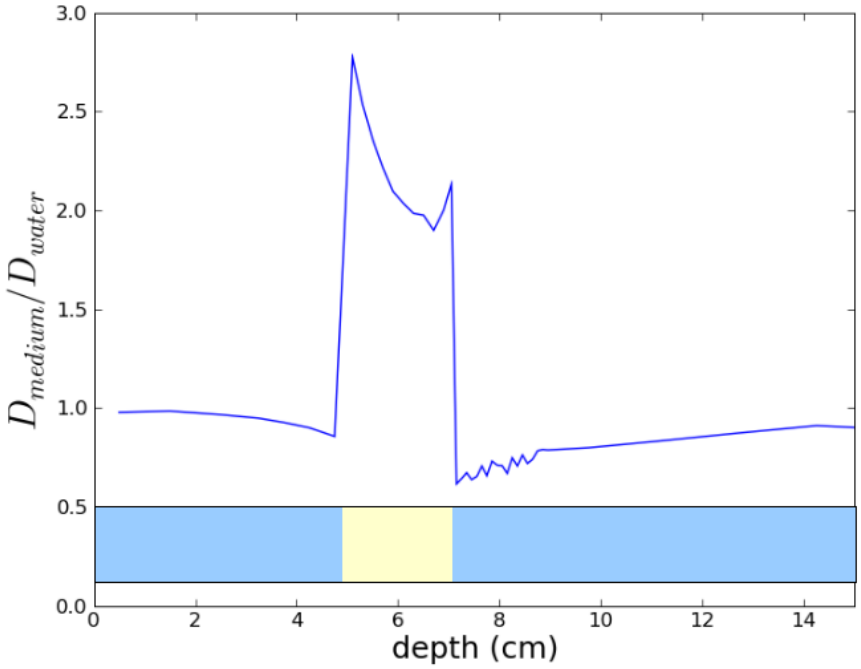

Figure III.2: Medium-dependent correction factor as a function of depth along the central axis of a kV-CBCT beam incident on a simple water phantom with a 2 cm slab of bone at 5 cm depth. The x-ray beam is incident from the left of the phantom.

relative to water. This effect can be parameterized as:

$$\alpha_j\left(x,y,z;\theta_i\right) \;=\; \begin{cases} \alpha_\infty - \left(\alpha_\infty - \alpha_0\right) e^{-\mu_\alpha\left(x_j^1 - x\right)} & , x < x_j^1 \\ 1 & , \text{otherwise} \end{cases} \tag{III.4}$$

Here, α_0 is the correction factor in soft tissue at the bone-tissue interface, and α_∞ is the correction factor far upstream from the interface. α_∞ should be close to, but less than unity in order to account for the slightly smaller fluence at these locations. The parameter μ_α models the rate at which the up-stream medium-dependent correction approaches the asymptotic value with increasing up-stream distance from the bone-tissue interface.

The factor β_i is the in-medium correction factor that accounts for the increased dose to bone due to photoabsorption in bone. This effect can be modeled with the following parameterization:

$$\beta_j\left(x,y,z;\theta_i\right) \;=\; \begin{cases} \beta_1 e^{-\mu_1\left(x - x_j^1\right)} + \beta_2 e^{-\mu_2\left(x_j^2 - x\right)} & , x_j^1 \le x \le x_j^2 \\ 1 & , \text{otherwise} \end{cases} \tag{III.5}$$

Here, the photon fluence is modeled to have two components, a primary fluence (subscript 1), and a backscattered fluence (subscript 2). The parameters β_1 and β_2 are the medium-dependent correction factors applicable on the bone side of the bone-tissue interface for the primary and backscattered photons, respectively, and the exponential factors account for the differential attenuation of the low-energy x-rays in bone relative to water. From Equation I.1, we can see that the value of β_1 and β_2 should be close to the ratio of the mass-energy absorption coefficient of bone to that of water evaluated at the primary and back-scattered photon energies respectively. However, it is difficult to determine the photon energy spectrum at a particular location within a patient without Monte Carlo simulation

so we relied on empirical studies to determine values for these parameters.

The downstream correction factor, γ_j, accounts for the reduction in the downstream photon fluence due to photoabsorption in bone. We found that an identical parameterization to the upstream correction can be used:

$$\gamma_j\left(x,y,z;\theta_i\right) = \begin{cases} \gamma_\infty - \left(\gamma_\infty - \gamma_0\right) e^{-\mu_\gamma\left(x-x_j^2\right)} & , x > x_j^2 \\ 1 & , \text{otherwise} \end{cases} \tag{III.6}$$

The downstream model parameters thus have similar interpretations to the analogous upstream parameters.

Monte Carlo simulation and MDC-DA model parameters

Monte Carlo techniques were used to derive the empirical MDC-DA model parameters used for calculation, and to provide gold-standard dose distributions to benchmark the accuracy of the MDC-DA using these parameters. The kV-CBCT beams simulated for dose calculation in this study were from the Varian on-board imager (OBI) system integrated into a Trilogy$^{\text{TM}}$linear accelerator (Varian Medical Systems, Palo Alto, CA). The beams used were the OBI version 1.3 half-fan beam operated with a half bow-tie filter, and characterized in [32]; and the OBI version 1.4 Standard Dose Head, Pelvis, and Low-Dose Thorax beams described in references [30, 34]. The x-ray beams were simulated using BEAMnrc [68]. The Standard Dose Head acquisition technique uses the full bow-tie filter whereas the Pelvis and Low-Dose Thorax techniques were simulated with the half bow-tie filter. The Standard Dose Head acquisition uses a 200° rotation of the x-ray source that is posteriorly incident on a supine patient. Table III.1 lists the kV-CBCT scan acquisition techniques used for each patient in this study.

Table III.1: kV-CBCT acquisition techniques used for dose calculation for each patient in this study. Each kV-CBCT x-ray beam simulated was from Varian's OBI system.

Patient	CBCT acquisition technique	X-ray Voltage (kVp)
Adult H&N 1[a]	OBI 1.3	125
Adult H&N 2	OBI 1.4 standard-dose head	100
Adult H&N 3	OBI 1.4 standard-dose head	100
Adult H&N 4	OBI 1.4 standard-dose head	100
Pediatric H&N 1[a]	OBI 1.3, OBI 1.4 Standard Head	125
Adult pelvis 1[a]	OBI 1.3	125
Adult pelvis 2	OBI 1.4 pelvis	125
Adult pelvis 3	OBI 1.4 pelvis	125
Adult chest[a]	OBI 1.3	125
Adult chest	OBI 1.4 low-dose thorax	110
Adult chest	OBI 1.4 low-dose thorax	110
Adult chest	OBI 1.4 low-dose thorax	110
Adult legs	OBI 1.4 pelvis	125
Pediatric abdomen	OBI 1.4 low-dose thorax	110

[a] Patients used to derive correction factor curves.

Patient dose-to-medium distributions were calculated with the Monte Carlo user code DOSXYZnrc [53, 78]. CT-based volumetric phantoms were created for each patient using four materials: air, lung, soft-tissue, and bone. Material segmentation was performed using a CT number to density calibration curve. In addition to the dose-to-medium distributions, the dose to water-like media was obtained with Monte Carlo calculation for each patient by setting each voxel in the CT-based volumetric phantoms to water, but with density assigned according to the CT number to density calibration. This second calculation is consistent with the model-based convolution/superposition treatment planning system calculations of Alaei et al. [3] that account for density inhomogeneities, but neglect medium-dependent effects.

The MDC-DA makes use of 10 tunable model parameters that characterize the effects of bone on the dose distribution resulting from kilovoltage x-rays [35]. In this work, we obtained independent model parameter sets for kV-CBCT imaging procedures performed on four patients with imaging sites including the adult head-and-neck (H&N) , pediatric

H&N, chest, and pelvis. The patients used for this purpose are referred to as Adult H&N 1, Pediatric H&N: OBI 1.3, Adult Pelvis 1, and Adult Chest 1. Separate parameter sets were determined for each patient by iteratively calculating and comparing the correction factors obtained using the MDC-DA correction method to gold-standard correction factors obtained by taking the ratio of the patient dose-to-medium distribution to the dose-to-water distribution calculated with the Monte Carlo technique. The MDC-DA calculations used to derive these model parameters utilized 8 sets of incident rays of one-dimensional correction factors separated by 45° (Figure III.1). An average model parameter set was obtained from the four individually obtained parameter sets, which was used for subsequent dose calculations throughout this work.

Benchmark calculations

To benchmark the accuracy of the MDC-DA algorithm, dose calculations were performed with the algorithm for 14 patients; four patients were used to derive the MDC-DA model parameters, and 10 patients were used as test cases for these parameter sets. These 10 patients in the second group had imaging sites including the head-and-neck, chest, abdomen, pelvis, and legs. Dose calculations were performed by applying the correction factors obtained with the MDC-DA to the dose-to-water distributions obtained as described above. These calculations were carried out for each patient using an average model parameter set obtained from the derived parameter sets. The accuracy of these calculations was assessed by comparing the resulting dose distributions to Monte Carlo calculated dose distributions.

In addition, we compared our results to a simple correction method based on multiplying the dose-to-water values calculated for bone voxels by the free-in-air, bone-to-water mass-energy absorption coefficient ratio using the procedure proposed by Alaei et

Table III.2: MDC-DA model parameters obtained for the patient types and imaging sites used in this study. The average parameter set was determined by taking the average of each parameter from the four patients.

Parameter	Adult H&N 1	Pediatric H&N 1	Pelvis 1	Chest 1	Average Set
α_∞	0.96	0.98	0.99	0.99	0.98
α_0	0.86	0.85	0.83	0.85	0.85
μ_α	0.82	0.82	0.85	0.85	0.84
β_1	2.24	2.21	2.28	2.23	2.24
μ_1	0.22	0.20	0.17	0.15	0.19
β_2	1.33	1.33	1.33	1.33	1.33
μ_2	0.17	0.16	0.18	0.16	0.17
γ_∞	0.95	0.95	0.95	0.95	0.95
γ_0	0.72	0.83	0.77	0.78	0.78
μ_γ	0.19	0.19	0.19	0.19	0.19

al. [3]. The energy of the unattenuated x-ray beam was used to determine the mass-energy absorption coefficient ratio.

III.1.3 Results

MDC-DA model parameters

Table III.2 lists the MDC-DA model parameters obtained for dose calculations for patients Adult H&N 1, Pediatric H&N: OBI 1.3, Adult Pelvis 1, and Adult Chest 1, and the model parameter set obtained by taking the average of the MDC-DA parameters for each imaging site. It is evident that there is some variation in the optimal parameters generated for different patient anatomies. This is a result of the difference in the relative amount of bone and soft-tissues in each imaged site, and of the arrangement of bone and soft-tissues in each site affecting the average energy fluence distribution within each patient. The average parameter set was used for the presented calculations in this study.

Benchmark results

Figure III.3 shows axial dose distributions in colorwash, and line profiles calculated for a pediatric H&N patient scanned with the OBI 1.4 Standard Dose Head protocol with a 200° posterior source rotation. Dose calculations were performed using four techniques: the Monte Carlo technique, the density-corrected-only dose-to-water technique, the simple correction method using the bone-to-water mass-energy absorption coefficient ratio, and the MDC-DA method. The distributions are each normalized to the maximum dose to the irradiated volume calculated with Monte Carlo. The Monte Carlo dose distribution shows a significant increase in the dose to the skull relative to the adjacent soft-tissue, which is due to the increased photoabsorption of the x-ray beam in bone. The density-corrected-only dose-to-water calculation resulted in a relatively homogeneous dose distribution in which the dose to bone was nearly equivalent to the dose to the adjacent soft-tissue. The simple correction method assumes a constant dose correction factor for all bone voxels and significantly overestimates the dose to bone everywhere. The MDC-DA algorithm corrected the bone dose to include the contribution from photoabsorption, and corrected the soft-tissue dose to account for the reduced x-ray fluence at these voxels due to photoabsorption. It is seen that the dose varies significantly along the patients anterior-posterior axis. This is due to the posterior scanning technique, which was accounted for with the MDC-DA by applying only correction factors calculated along the posteriorly incident rays shown in Figure III.1 (right).

Figure III.4 shows dose planes and profiles for the abdominal kV-CBCT scan of a prone pediatric patient. The dose delivered to the vertebrae and ribs is roughly a factor of three greater than the dose to surrounding soft-tissues. The profile along line segment AB shows that the dose-to-water calculation overestimates the dose to the soft-tissue in regions

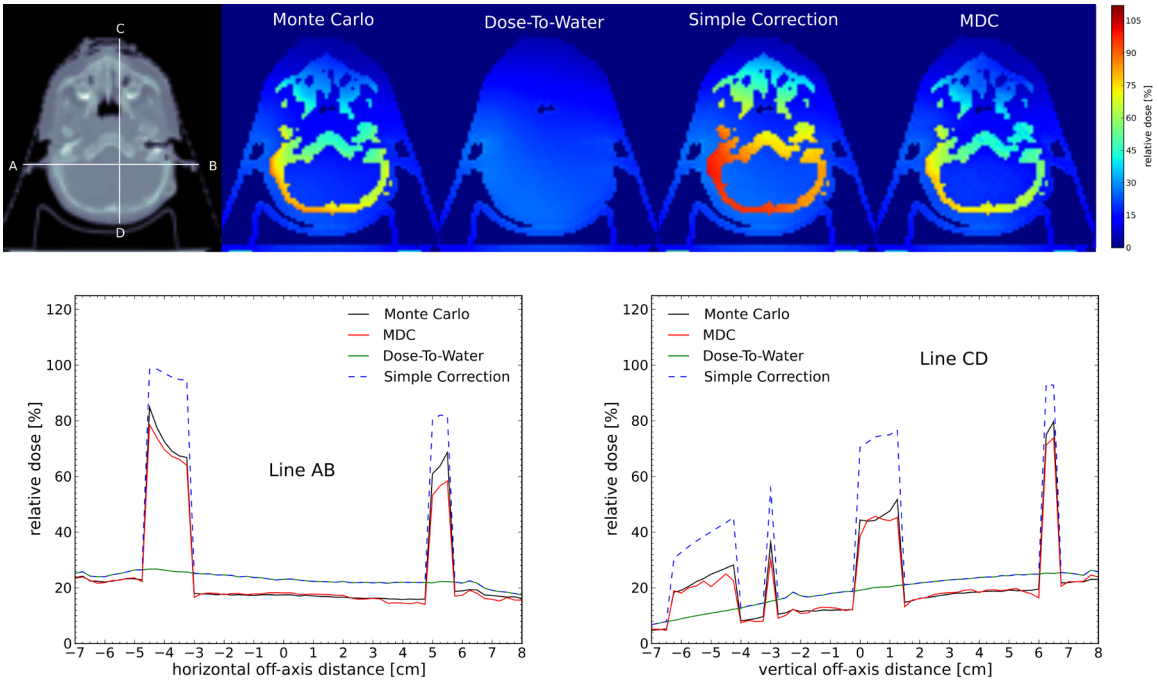

Figure III.3: (Top) Axial slice and corresponding dose planes for a pediatric H&N kV-CBCT scan. The acquisition technique simulated was the OBI 1.4 Standard Dose Head with a 200° posterior rotation. Doses were calculated with the Monte Carlo technique, the density-corrected-only dose-to-water, the simple correction based on the bone-to-water mass-energy absorption coefficient ratio, and the MDC-DA. (Bottom) Dose profiles through the horizontal and vertical lines shown in the CT image (top left). The dose distributions here are normalized to the maximum dose to the irradiated volume calculated with Monte Carlo.

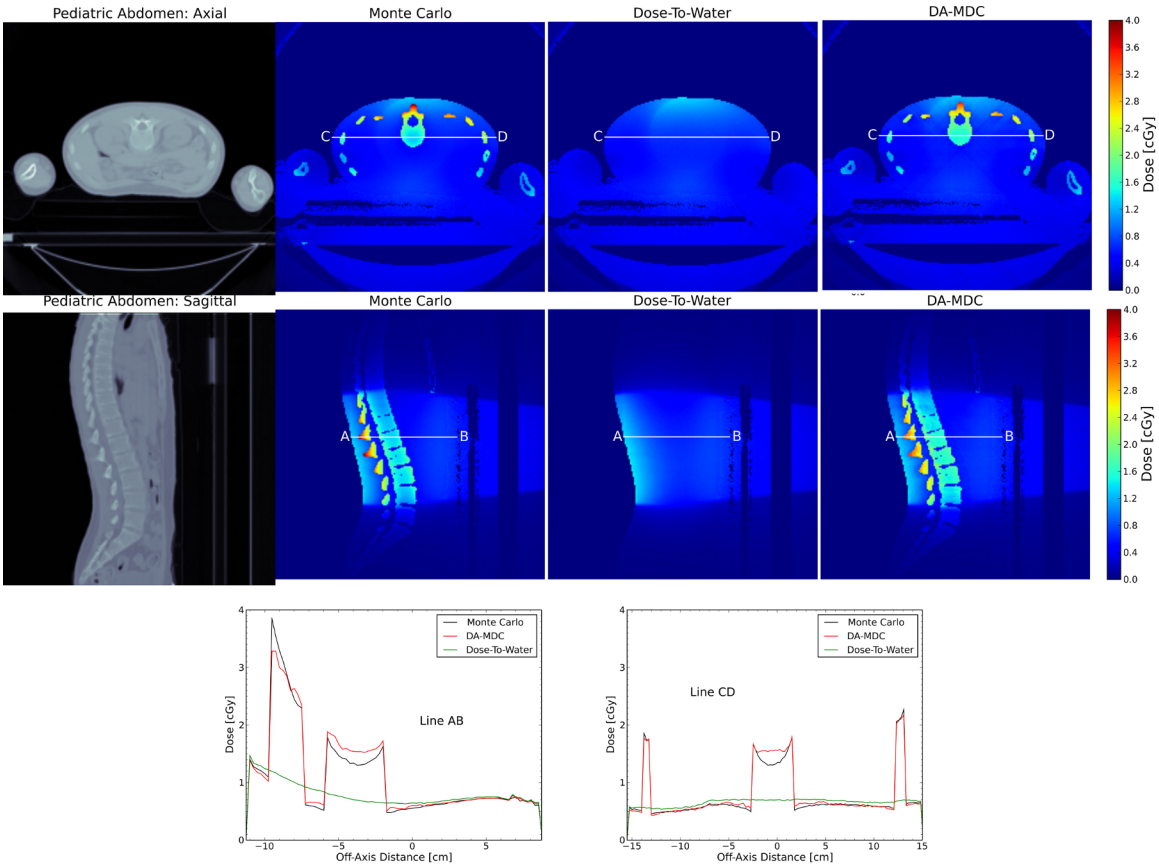

Figure III.4: (Top) Axial slice and corresponding dose planes for an abdominal kV-CBCT scan of a pediatric patient in the prone position. Doses were calculated with the Monte Carlo technique, the density-corrected-only dose-to-water, and the MDC-DA. (Middle) Sagittal slice and corresponding dose planes for a pediatric abdominal kV-CBCT scan. (Bottom) Dose profiles through lines AB and CD.

close to the spine and ribs, but is accurate for regions far from bone where a significant portion of the photon fluence has not been attenuated by bone. The spinal cord presents the worst-case scenario for a soft-tissue structure calculated with the dose-to-water technique since it is completely surrounded by bone and thus receives a significantly reduced fluence. This results in dose overestimation of approximately 40% with the dose-to-water calculation. The MDC-DA calculation models the effects of bone on the dose distribution and results in a significant accuracy improvement, reducing the dose error to less than 10% along this line segment for the spinal cord.

Figures III.5 and III.6 show the results of the dose calculations for the Adult Pelvis

3 patient and the Adult Chest 4 patient. The dose to bone is highly inhomogeneous, with the largest doses in portions of bone that are closest to the surface of the patient. The MDC-DA accurately accounts for the geometric distribution of these inhomogeneities. The dose volume histograms (DVHs) compare the results of calculations with the MDC-DA and the dose-to-water calculations to the Monte Carlo distributions for specific organs. Dose volume histograms are commonly used in radiation therapy to characterize the dose delivered to organs. A point on a DVH curve denotes the percentage of the volume of an organ that is receiving a dose greater than or equal to that specified on the abscissa. For example, if a point on a DVH curve corresponds to 90% of the volume and 10 cGy, then 90% of the organ is receiving at least 10 cGy. The dose-to-water calculation results in a significant underestimation of the dose to the femoral heads and ribs, and overestimates the dose to the soft-tissue structures. The MDC-DA shows a significant improvement in the accuracy of calculating the dose to soft-tissue and bone organs-at-risk.

Figure III.7 shows the results of the dose calculations for the Adult legs patient from a kV-CBCT scan. Whereas the dose-to-water calculation underestimates the dose to bone, this calculation is accurate for soft-tissue voxels that are not immediately adjacent to bone. Due to the geometry of bone in this patient, most soft-tissue voxels are irradiated by a photon fluence that has only minimally been perturbed by the passage though bone. This effect is accounted for in the MDC-DA since correction factors along rays that do not intersect bone are set to unity.

Table III.3 summarizes the results of the dose calculations performed on each patient. The mean dose to bone and soft-tissue voxels in cGy calculated for the region being imaged for each patient for a single kV-CBCT scan is shown. The doses reported are for the Monte Carlo calculation, the dose-to-water calculation, the MDC-DA calculation

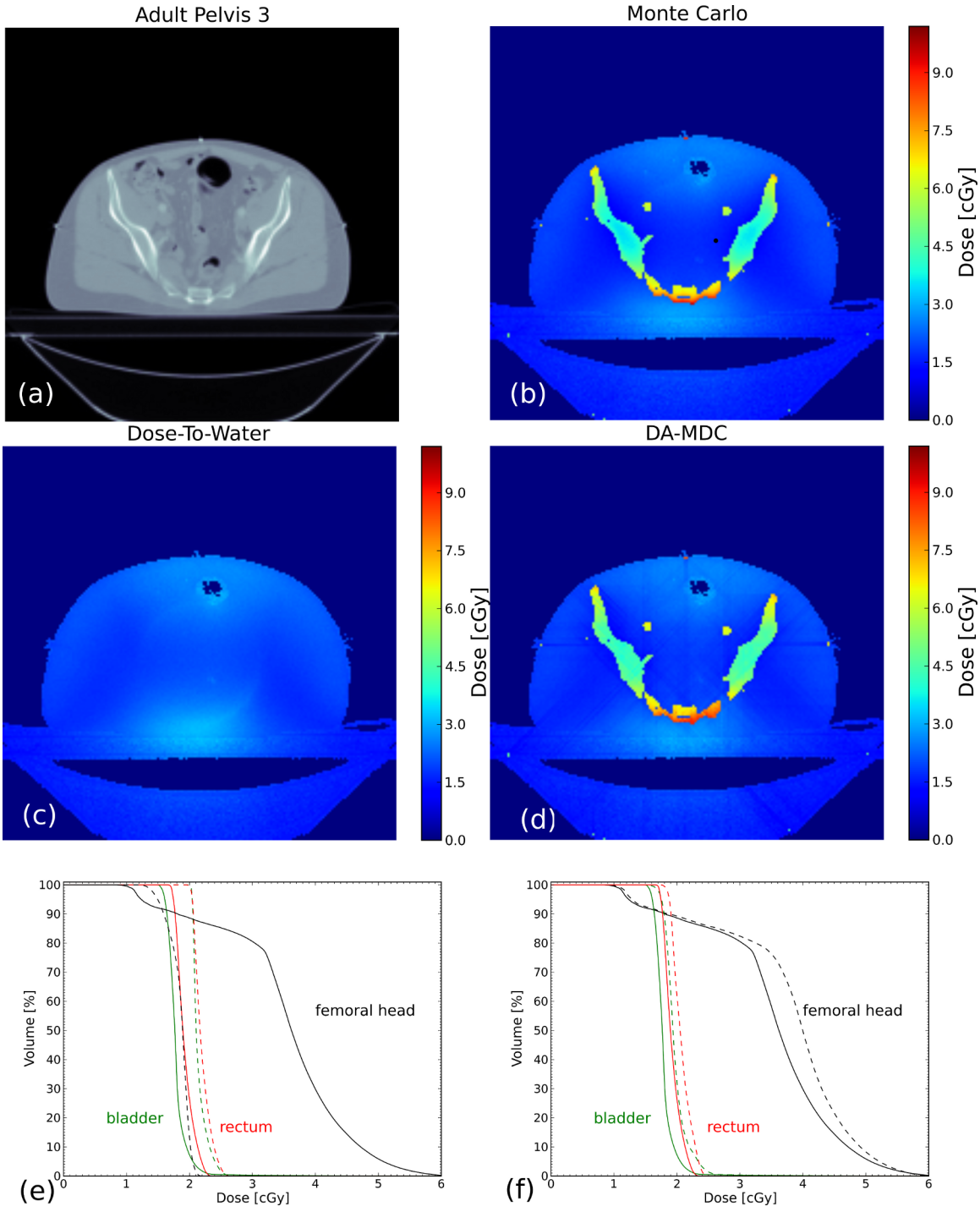

Figure III.5: Axial CT slice (a) and corresponding dose planes in colorwash (b-d) for a kV-CBCT scan of the Adult Pelvis 3 patient. The Monte Carlo (b), dose-to-water (c), and MDC-DA (d) calculations are shown. (e) DVHs calculated from the Monte Carlo distributions (solid) compared to dose-to-water calculation (dashed) for organs at risk in the pelvis. (f) Monte Carlo calculated DVHs (solid) compared to the MDC-DA calculation (dashed).

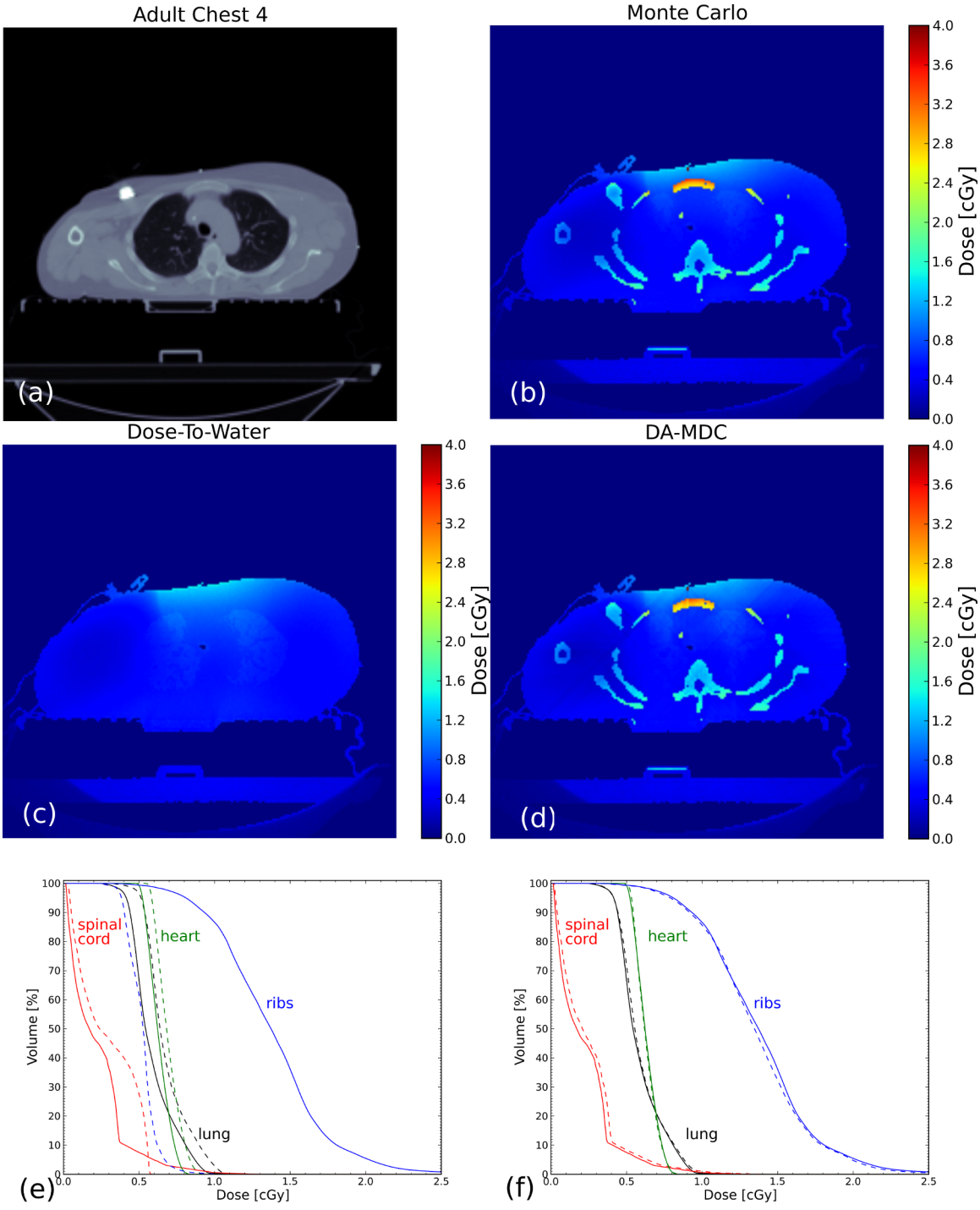

Figure III.6: Axial CT slice (a) and corresponding dose planes in colorwash (b-d) for a kV-CBCT scan of the Adult Chest 4 patient. The Monte Carlo (b), dose-to-water (c), and MDC-DA (d) calculations are shown. (e) DVHs calculated from the Monte Carlo distributions (solid) compared to dose-to-water calculation (dashed) for organs at risk in the pelvis. (f) Monte Carlo calculated DVHs (solid) compared to the MDC-DA calculation (dashed).

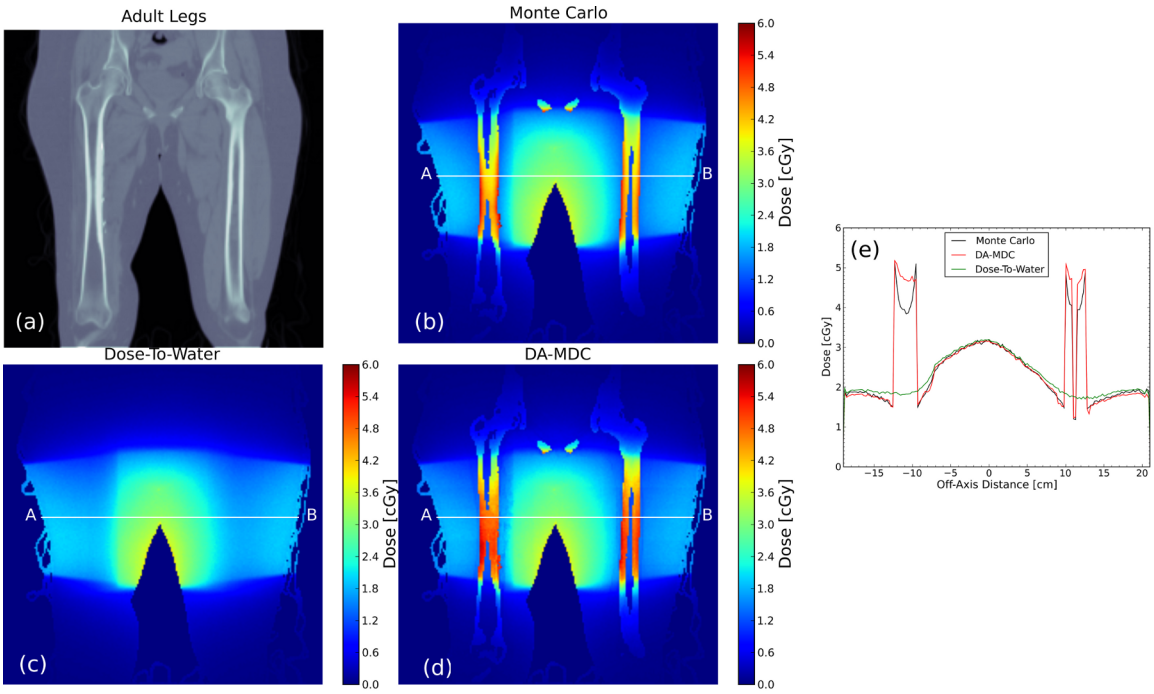

Figure III.7: Coronal CT slice (a) and corresponding dose planes in colorwash (b-d) for a kV-CBCT scan of the Adult Legs patient. The Monte Carlo (b), dose-to-water (c), and MDC-DA (d) calculations are shown. (e) Dose profiles along line AB for each dose calculation method.

using the average parameter set, and the simple correction method of multiplying the dose-to-water by the ratio of the bone-to-water mass-energy absorption coefficients. The absolute dose to patients can vary by more than an order of magnitude depending on patient size, imaging site, and acquisition technique. The mean dose to bone voxels varies from 2.1 to 3.5 times the mean dose to soft-tissue voxels across patients. The dose-to-water calculation underestimates the mean bone dose by up to -64%, with an average error of -60%. In contrast, the simple correction method overestimates the mean bone dose by 28% to 63%. The MDC-DA method using the average model parameter set is accurate to within -4% to 7% for mean bone dose calculation. For soft-tissue voxels, the dose-to-water calculation technique overestimates the mean dose by up to 21%. The MDC-DA method results in mean soft-tissue dose errors that are within -3 to 5%.

Table III.3: Mean dose in cGy from a single kV-CBCT scan to bone and soft-tissue voxels in the region being imaged. Doses were calculated with the Monte Carlo method, the dose-to-water method, and the MDC-DA method using the average model parameter set.

	Mean Bone Voxel Dose [cGy]				Mean Soft-Tissue Voxel Dose [cGy]		
Patient	MC	D_{water}	MDC-DA	Simple Correction	MC	D_{water}	MDC-DA
Adult H&N 1	15.72	6.70	16.76	24.67	5.01	6.06	5.23
Adult H&N 2	0.46	0.18	0.44	0.66	0.19	0.21	0.19
Adult H&N 3	0.47	0.19	0.47	0.70	0.16	0.18	0.16
Adult H&N 4	0.50	0.20	0.49	0.73	0.19	0.22	0.19
Ped. H&N: OBI 1.3	18.84	6.87	18.77	25.31	5.33	6.11	5.26
Ped. H&N: OBI 1.4	0.87	0.30	0.82	1.11	0.26	0.30	0.26
Adult Pelvis 1	7.30	3.01	7.06	11.09	3.03	3.28	2.99
Adult Pelvis 2	3.68	1.63	3.85	6.00	1.56	1.72	1.58
Adult Pelvis 3	4.35	1.89	4.56	6.96	1.73	1.91	1.76
Adult Chest 1	10.65	4.04	10.22	14.90	3.80	4.16	3.71
Adult Chest 2	1.34	0.51	1.35	1.88	0.43	0.48	0.43
Adult Chest 3	2.16	0.85	2.21	3.13	0.73	0.83	0.73
Adult Chest 4	1.24	0.45	1.22	1.66	0.41	0.46	0.41
Adult Legs	3.39	1.31	3.58	4.83	1.61	1.65	1.62
Ped. Abdomen	1.34	0.52	1.37	1.92	0.46	0.50	0.46

III.1.4 Discussion and conclusions

We have presented a new algorithm to calculate medium-dependent correction factors for kV x-rays that accounts for the effects of differential absorption rates in bone relative to the soft tissues in the human body.

We have benchmarked the accuracy of the MDC-DA for the calculation of imaging dose from kV-CBCT by comparing dose calculations performed with this method to Monte Carlo dose-to-medium distributions. We showed that the MDC-DA algorithm is capable of calculating the imaging dose from kV-CBCT acquisitions that use the half-fan (360° source rotation) and full-fan (200° source rotation) scanning techniques. In this work we used a single set of model parameters to calculate the medium-dependent correction factors for all patients. The results of dose calculations using this parameter set were within 7% mean dose error for bone, and 5% mean soft-tissue dose error for each of the 14 patients studied. Potential improvement of these results could be obtained if the separate model parameter sets obtained for each imaging site were used for patients with similar imaging sites; however, this would make the implementation unwieldy in practice.

The MDC-DA algorithm was shown to be superior to a simple correction method by which the medium-dependent effect is accounted for by multiplying the dose-to-water distribution by the ratio of the bone-to-water mass-energy absorption coefficients. The free-in-air mass-energy absorption coefficient ratio overestimates the medium-dependent effect for bone voxels as the energy used to determine this factor was that of the unattenuated beam. Moreover, from Table III.3 we see that the ratio of the mean dose to bone calculated with Monte Carlo to the mean dose to bone calculated with the dose-to-water calculation varied from 2.3 to 2.9 for the patients studied, indicating that a single scalar multiplication

is insufficient to correct for medium-dependent effects when considering variations in patient size and imaging site.

The MDC-DA as presented here can be used to extend model-based radiotherapy treatment planning systems to accurately calculate the dose-to-medium delivered to patients from kilovoltage x-rays, and thus facilitate the recording and management of the radiation dose that patients receive from kilovoltage imaging.

III.2 The effective approach to medium-dependent correction

III.2.1 Introduction

In the previous section the MDC-DA was developed which corrected dose-to-water calculations for the effects of photoabsorption in bone. The corrections for both soft-tissue and bone are based on an empirical parameterization of the medium-dependent correction along rays incident on the patient from the x-ray source. Model parameters were empirically obtained by fitting the model to gold-standard correction factor distributions obtained for multiple patients using the Monte Carlo method. For the patients studied the corrected dose distributions were within 7% for bone and 5% for soft-tissues. To improve on this accuracy it is necessary to use more than one model parameter set, with each set of parameters optimized for use with a specific body site, such as the head-and-neck, pelvis, chest, etc. As Table III.2 shows, there is some variation in optimal model parameters obtained individually for different patients. In practice the approach of using separate model parameters for different imaging sites would be cumbersome to implement. It would also be impossible to implement for CT imaging procedures that are not limited to a single anatomical region, such as a full-body scan. To overcome this potential limitation we have developed a second

approach to determine the medium-dependent corrections for kilovoltage x-rays, which is to be described in this section.

This new approach is based on the hypothesis that the correction factors needed to convert dose from model-based dose-to-water calculations to absorbed dose-to-medium depend on both the attenuation characteristics of the absorbing media and the changes to the energy spectrum of the incident x-rays as they traverse media with an effective atomic number different than that of water. To explore this hypothesis, Monte Carlo simulation techniques were used to generate empirical medium-dependent correction factors that take both effects into account. We found that the correction factors could be expressed as a function of a single intermediate quantity, called the effective bone depth, which is a measure of the average thickness of bone that an x-ray beam must penetrate to reach a voxel. This new correction method is referred to as the Medium-Dependent Correction–Effective Approach (MDC-EA) . In the following, we describe the method in detail and show its application for calculating the dose to patients resulting from kV-CBCT image guidance procedures. The calculation accuracy of this new approach is validated by comparing the dose distributions obtained using the MDC-EA to those calculated with the Monte Carlo technique.

III.2.2 Methods

Monte Carlo simulation of dose correction factors

Using the Monte Carlo techniques described by Ding and Coffey [28], we calculated the imaging dose-to-medium (D_{M}) delivered to 14 patients from kV-CBCT scans for multiple imaging sites including the head-and-neck (H&N), pelvis, chest, abdomen, and legs. The x-ray beams used were from the Varian on-board imager (OBI) system integrated into a

Table III.4: kV-CBCT acquisition techniques used for dose calculation for each patient in this study. Each kV-CBCT x-ray beam simulated was from Varian's OBI system. (Reproduced from [66] with permission)

Patient	CBCT acquisition technique	X-ray Voltage (kVp)
Adult H&N 1[a]	OBI 1.3	125
Adult H&N 2	OBI 1.4 standard-dose head	100
Adult H&N 3	OBI 1.4 standard-dose head	100
Adult H&N 4	OBI 1.4 standard-dose head	100
Pediatric H&N 1[a]	OBI 1.3	125
Adult pelvis 1[a]	OBI 1.3	125
Adult pelvis 2	OBI 1.4 pelvis	125
Adult pelvis 3	OBI 1.4 pelvis	125
Adult chest[a]	OBI 1.3	125
Adult chest	OBI 1.4 low-dose thorax	110
Adult chest	OBI 1.4 low-dose thorax	110
Adult chest	OBI 1.4 low-dose thorax	110
Adult legs	OBI 1.4 pelvis	125
Pediatric abdomen	OBI 1.4 low-dose thorax	110

[a] Patients used to derive correction factor curves.

Trilogy^{TM} linear accelerator (Varian Medical Systems, Palo Alto, CA). The acquisition techniques used were the clinical default protocol half-fan beam from OBI version 1.3 described by Ding et al. [32], and the OBI 1.4 Standard-Dose Head, Pelvis, and Low-Dose Thorax techniques described by Ding et al. [34]. Table III.4 lists the acquisition techniques used for each patient in the study. The kV-CBCT beams were simulated using the BEAMnrc code [68], and dose calculations were performed with the DOSXYZnrc usercode [53, 78].

The calculation volumes for each patient were created from volumetric CT images taken of the patients for the purpose of radiotherapy treatment planning. Four materials were used for dose calculation: air, lung, soft-tissue, and cortical bone. Material type was assigned to each voxel based on the physical density of the voxel, which was determined from a CT number to density calibration curve. Density ranges for each material were 0.001–0.044 g/cm^3 for air, 0.044–0.302 g/cm^3 for lung, 0.302–1.101 g/cm^3 for soft-tissue, and 1.101–2.088 g/cm^3 for bone. A second Monte Carlo calculation was performed for all patients in which dose distributions were obtained by accounting for density inhomo-

geneities, but neglecting medium-dependent effects. This was done by setting all materials in the calculation volume to water and scaling the density of each voxel according to a CT number to density calibration curve. The resulting density-corrected-only dose distribution (D_{DCO}) is consistent with the model-based superposition/convolution calculations of chapter II and Alaei et al. [3]. The gold standard matrix of correction factors, $f_{\mathrm{c}}(x,y,z)$, that converts the density-corrected-only dose distribution to dose-to-medium was found for each patient by taking the ratio of the doses to corresponding voxels resulting from each calculation:

$$f_{\mathrm{c}}(x,y,z) = \frac{D_{\mathrm{M}}(x,y,z)}{D_{\mathrm{DCO}}(x,y,z)}. \tag{III.7}$$

Effective bone depth calculation

Using patient material and density data derived from CT images, the x-ray beam fluence profile, and the imaging isocenter, we calculated the effective bone depth that the x-ray beam penetrates to reach each voxel, d_{EB} . This quantity was calculated by first modeling the rotating x-ray source of the OBI system used for kV-CBCT acquisition as a set of evenly spaced discrete incident beams, and calculating the thickness of bone, d_{B}, that rays parallel to the primary beam pass through to reach each voxel. The effective bone depth was then calculated for each voxel by computing an average of the bone thicknesses for each ray to reach each voxel, weighted by a function that specifies the contribution of each of the individual rays to the effective bone depth at each voxel:

$$d_{\mathrm{EB}}(x,y,z) = \frac{\sum_i w(x,y,z)_i \cdot d_{\mathrm{B}}(x,y,z)}{\sum_i w(x,y,z)_i} \tag{III.8}$$

where the sum in Equation III.8 is over each incident beam. The weighting function, w, depends on the x-ray beam fluence profile ($I(x,y,z)$), the source-to-voxel distance

($SVD\,(x,y,z)$), and the bone thickness for each incident ray. In this work, the weighting function used was:

$$w\,(x,y,z) = \frac{I\,(x,y,z)}{d_{\mathrm{B}}\,(x,y,z)^2 + \left(\frac{SVD(x,y,z)}{a}\right)^2}, \tag{III.9}$$

where a is a constant used to scale the relative weight of SVD and d_{B} .

For each kV-CBCT acquisition technique except for the OBI 1.4 Standard-Dose Head a 360° rotation of the x-ray source was used, and was modeled by utilizing 16 incident rays separated by 22.5° to calculate the effective bone depth. We found that there was a negligible difference in effective bone depth distributions if the number of incident rays was increased from 16 to 360. The Standard-Dose Head technique utilizes a 200° posterior arc of the x-ray source with x-ray incidence spanning from a supine patient's left lateral side to a right anterior oblique incidence. This 200° arc was modeled using 10 incident beams separated by 20° to calculate the effective bone depth.

Correction factor curve determination and dose calculation

Monte Carlo simulation and effective bone depth calculations were carried out as described above for the 14 real patients included in this study. These patients were divided into two groups: (1) four patients were used to derive correction factor curves from the correlation between the effective bone depth and dose correction factor, and (2) ten patients were used as test cases to validate the use of the curves for dose calculation. The imaging sites for the first data set included an adult H&N, a pediatric H&N, an adult pelvis, and an adult chest. The remaining patients used for validation included imaging sites such as the adult H&N, chest, pelvis, pediatric abdomen, and the legs.

To derive correction factor curves as a function of effective bone depth, the gold

standard correction factors and corresponding effective bone depths for all voxels of all patients in group 1 were combined into a single data set. This data set was then investigated to obtain a general correlation of the correction factor as a function of effective bone thickness individually for bone and soft-tissue:

$$f_{\mathrm{c}}\left(d_{\mathrm{EB}}\right) = \begin{cases} f_{\mathrm{c}}^{\text{bone}}\left(d_{\mathrm{EB}}\right) & \text{, bone voxels} \\ f_{\mathrm{c}}^{\text{soft-tissue}}\left(d_{\mathrm{EB}}\right) & \text{, soft-tissue voxels} \end{cases} \tag{III.10}$$

The derived curves were used for dose calculation for each patient by calculating the effective bone depth distributions and applying the resulting correction factor to the density-corrected-only calculation:

$$D_{\mathrm{M}}\left(x,y,z\right) = D_{\mathrm{DCO}}\left(x,y,z\right) f_{\mathrm{c}}\left(d_{EB}\left(x,y,z\right)\right). \tag{III.11}$$

Validation of the dose calculations was performed by comparing the resulting dose distributions to Monte Carlo dose distributions calculated for each patient.

III.2.3 Results

Monte Carlo simulation of dose correction factors

Figure III.8 shows an axial slice through the kV-CBCT image of an adult H&N patient and the dose correction factors for voxels in this slice. Dose correction factors are generally greater than one for bone voxels and are typically in the range of 2–3. Soft-tissue voxels generally have dose correction factors less than one. Bone voxels on the periphery of the skull have the largest correction factors, as the primary x-ray beam has not been attenuated by bone prior to irradiation of these voxels for a portion of the rotation of the x-ray source

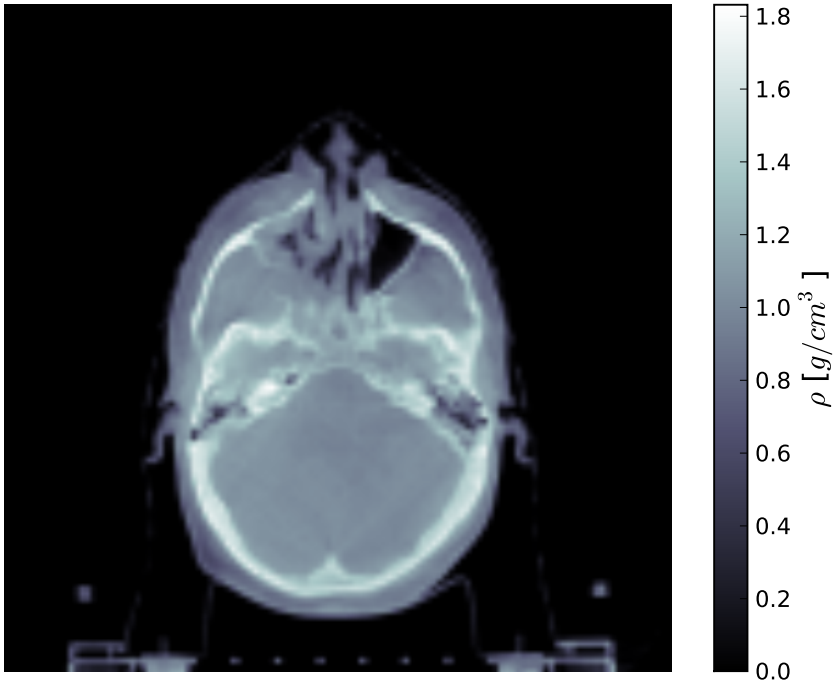

(a) Density distribution

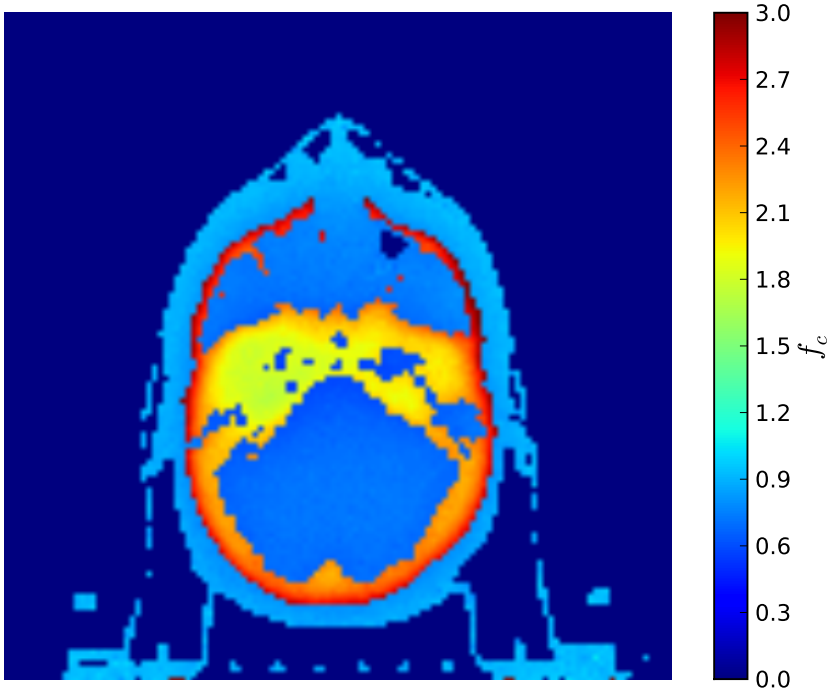

(b) Correction factor distribution

Figure III.8: (a) Axial CT slice through an adult H&N kV-CBCT image. (b) The dose correction factor distribution calculated with Monte Carlo for the slice shown in (a). Note that the values of the correction factors are not constant for all voxels of the same medium. Bone and soft-tissue voxels interior to the skull tend to have smaller correction factors due to the lack of low-energy x-rays at these locations. (Reproduced from [66] with permission)

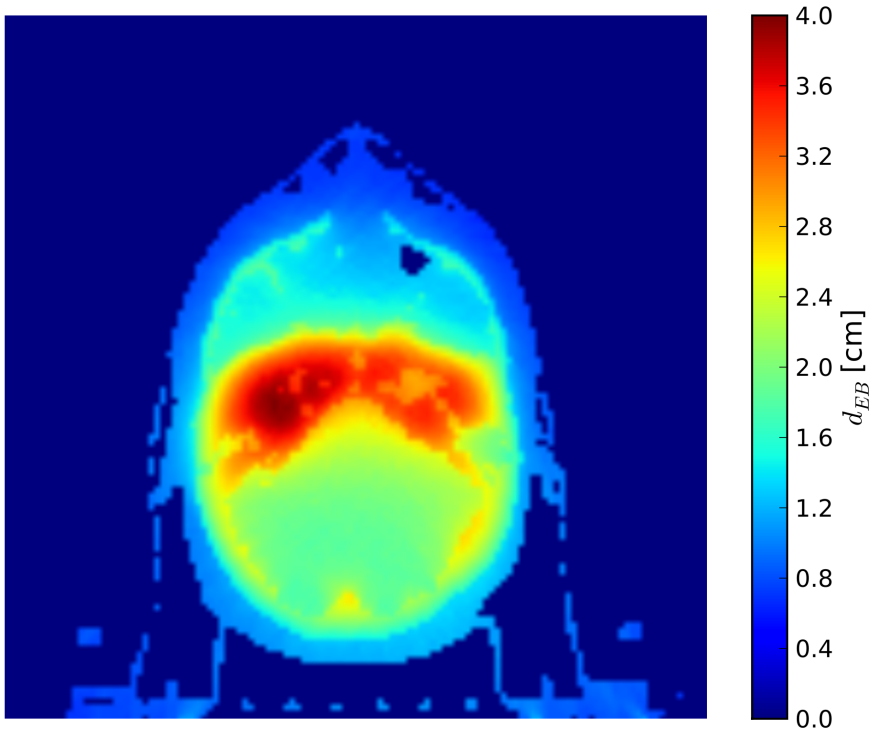

Figure III.9: The calculated effective bone depth distribution for the adult H&N kV-CBCT slice shown in Figure III.8. Regions of high effective bone depth are in the interior portions of the skull where the dose correction factors tend to be the lowest. Low effective bone depth regions are on the periphery of the skull where the primary beam is directly incident on these voxels before traveling through bone for part of the x-ray source rotation. (Reproduced from [66] with permission)

around the skull. Voxels interior to the skull tend to have smaller correction factors as the low energy x-ray fluence is heavily depleted at these locations due to photoabsorption in bone.

Effective bone depth calculation and correction factor curves

Figure III.9 shows an example of the effective bone depth distribution calculated for the axial slice shown in Figure 1. High effective bone depth was calculated in regions in or near thick bones; lower values of effective bone depth are seen in the soft-tissues in the periphery of the patient, and on the most exterior bone surfaces. The effective bone depth distribution shown in Figure III.9 was calculated using the 16 incident rays separated by 22.5° as described

in Section 2.1. We performed similar calculations with 4, 8, 32, 64, and 360 incident rays and found that calculations using less than 16 rays resulted in effective bone depth distributions that inadequately characterized the distribution of bone in the patient, and calculations using more than 16 incident rays did not show significant improvement to justify the additional calculation time.

Dose correction factors and effective bone depth distributions were calculated for each of the patients in the first data set with the intent of correlating the two quantities. FigureIII.10 (left) shows a scatter plot of correction factor versus effective bone depth showing data from all bone voxels and soft-tissue voxels of each patient in the first group. Each point in the scatter plot corresponds to a single voxel. In total, this plot shows data from nearly 3×10^5 bone voxels and more than 3×10^6 soft-tissue voxels. The red lines in Figure III.10 are least-square fits to the combined data set and give the dose correction factors as a function of effective bone depth separately for bone and soft-tissue voxels. The functional form of the correction factor curves was obtained using an online curve fitting application [46]. The equations for these curves are

$$f_{\mathrm{c}}^{\mathrm{bone}} = 3.6258 - 2.1422 \left[1 - \left(1 + \left(\frac{d_{\mathrm{EB}}}{4.4518} \right)^{1.5171} \right)^{-3.3769} \right] \qquad \text{(III.12)}$$

$$f_{\mathrm{c}}^{\text{soft-tissue}} = \left(2.0953 + 6.7997 \cdot d_{\mathrm{EB}}^{4.5429} \right)^{0.07178} . \qquad \text{(III.13)}$$

Figure III.10 (right) shows the scatter plots of dose correction factor vs. effective bone depth for each individual patient in the first group, along with the curves obtained for the combined data set. The obtained curves fit each individual patient distribution, suggesting that the effective bone thickness is a good surrogate for explicit calculation of

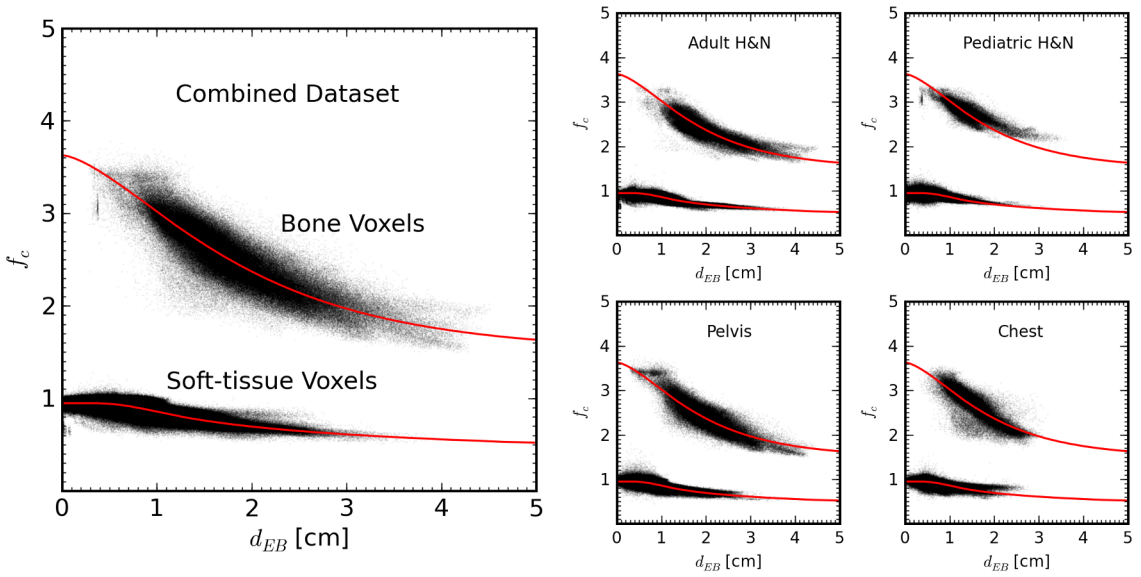

Figure III.10: (Left) Scatter plot of dose correction factor f_c and effective bone depth (d_{EB}) for the combined data set of patients in group 1. Each point on the plot corresponds to a single voxel; a total of nearly 3×10^5 bone voxels and more than 3×10^6 soft-tissue voxels are shown. The red lines are least-square fits that give the dose correction factor as a function of effective bone depth separately for bone and soft-tissue voxels. (Right) Scatter plots of dose correction factor versus effective bone depth for each individual patient in group 1 with the least-squares fit lines from the combined data set. The lines shown here are used as correction factor curves for dose calculation throughout this work. (Reproduced from [66] with permission)

the correction factor at a given voxel, regardless of patient type or imaging site.

The weighting function used to combine the bone depths from each incident direction into the effective bone depth is given by Equation III.8. Neglecting the bone depth term, the weighting function is simply the product of the photon fluence profile and the inverse square divergence of the beam, which was the intuitive starting point for determining the relative contribution of each beam direction to the weighted average. We found, however, that the inclusion of the effective bone depth term in the denominator reduced the relative error of the dose correction factor correlation curves, ie. the scatter plots of dose correction factor vs. effective bone depth showed less dispersion. This was quantified by binning the dose data shown in these plots into effective bone depth bins, and calculating the standard deviation error for each bin. Multiple test functions were attempted, with the function shown in Equation III.8 resulting in the smallest errors overall.

Dose calculation with the MDC-EA

Dose calculations were carried out as described above for each of the 10 patients in the second patient group using Equations III.12 and III.13 to convert effective bone depth to dose correction factor. Example calculated dose distributions are shown in Figures III.11, III.12, and III.13 for the Adult H&N 4, Adult Pelvis 3, and Adult Chest 2 patients, respectively. The dose calculation for Adult H&N 4 was performed with the OBI 1.4 Standard-Dose Head scanning technique which utilizes a 200° posterior rotation of the x-ray source. The Monte Carlo calculations show the enhanced dose to bone, which is most prominent in the regions which are directly irradiated by the primary x-ray beam. The density-corrected-only calculations result in a relatively homogeneous dose distribution as photoabsorption in bone is not accounted for. The MDC-EA calculations correct for the effects of photoabsorption

in bone on the dose distribution by enhancing the dose to bone and decreasing the dose to the surrounding soft-tissues. Note from the profile along line AB in Figure III.12 that the dose-to-medium does not always trend with the density-corrected-only distribution. Simple application of a constant multiplicative correction factor would incorrectly predict the shape of the Monte Carlo distribution; however, the MDC-EA accurately models the dose-to-medium. The thoracic CT scan dose planes and profiles shown in Figure III.13 show that the MDC-EA is capable of accurately calculating the radiation dose to lung, as well as other soft-tissues and bone.

Table III.5 shows the mean dose to bone, soft-tissue, and lung voxels calculated with the Monte Carlo, density-corrected-only, and MDC-EA techniques for each patient. The magnitude of the imaging dose depends on imaging site, patient size, and acquisition technique, varying by roughly an order of magnitude across all patients studied. An examination of the accuracy of the MDC-EA across this group of patients is thus easiest done in a relative fashion. Table III.6 shows the mean and standard deviation dose errors normalized to the maximum soft-tissue dose to each patient calculated for the density-corrected-only calculations and the MDC-EA calculations for each patient. The density-corrected-only calculations result in mean bone dose errors up to -103%, with standard deviations of the distributions approaching nearly 40%. The MDC-EA is capable of correcting the mean bone dose to within 2.55% for all patients and the standard deviation dose errors to within 13.49%. The density-corrected-only calculations produced mean dose errors of up to 8.18% for soft-tissue voxels, whereas the MDC-EA corrected each distribution to within 1.26% of the gold-standard. The standard deviation dose errors for the soft-tissue voxels were as high as 6.61% for the density-corrected-only calculations, but were within 3.22% for the MDC-EA calculations.

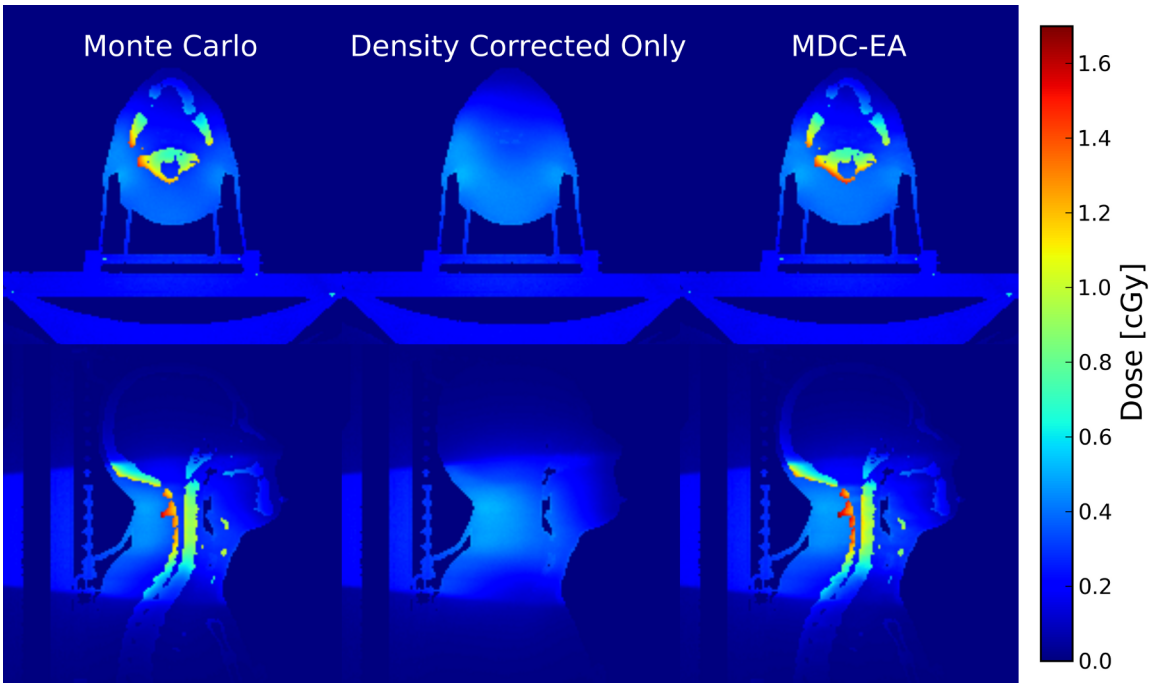

Figure III.11: Dose planes calculated for a single kV-CBCT scan of patient adult H&N 4. Axial (top) and sagittal (bottom) planes are shown for the Monte Carlo calculation (left), the density-corrected-only calculation (middle), and the MDC-EA calculation (right). The kV-CBCT acquisition mode used was the OBI 1.4 Standard Head with a full bow-tie filter and 200° posterior rotation of the x-ray source. (Reproduced from [66] with permission)

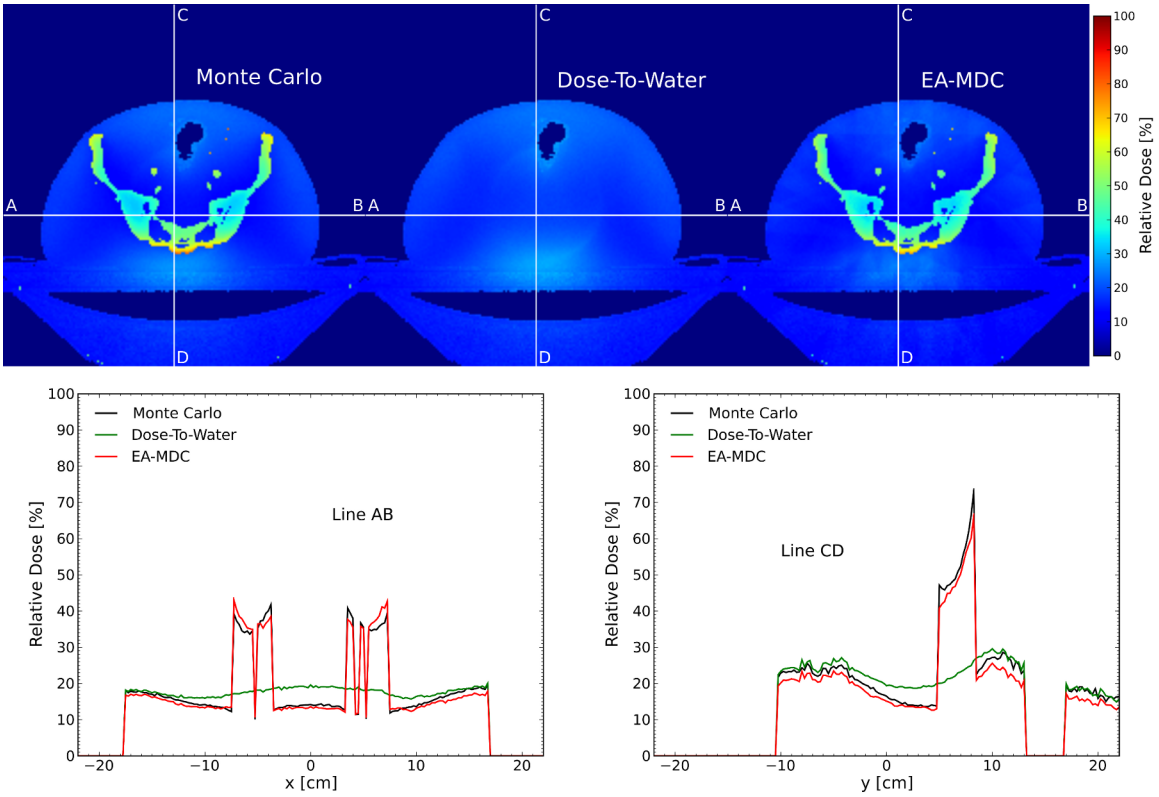

Figure III.12: Single kV-CBCT scan dose planes and line profiles for the Adult Pelvis 3 patient. The Monte Carlo calculation (top left) shows the highly inhomogeneous dose distribution in the bony pelvis that is completely neglected in the density-corrected-only calculation (top middle). The MDC-EA calculation (top right) is capable of accurately accounting for the medium-dependent effect on the bone dose. The line profiles show that the soft-tissue dose is considerably affected by the medium-dependent effect. The density-corrected-only calculations overestimate the soft-tissue dose in the proximity of bone; however, the MDC-EA calculation accounts for the medium-dependent effect. (Reproduced from [66] with permission)

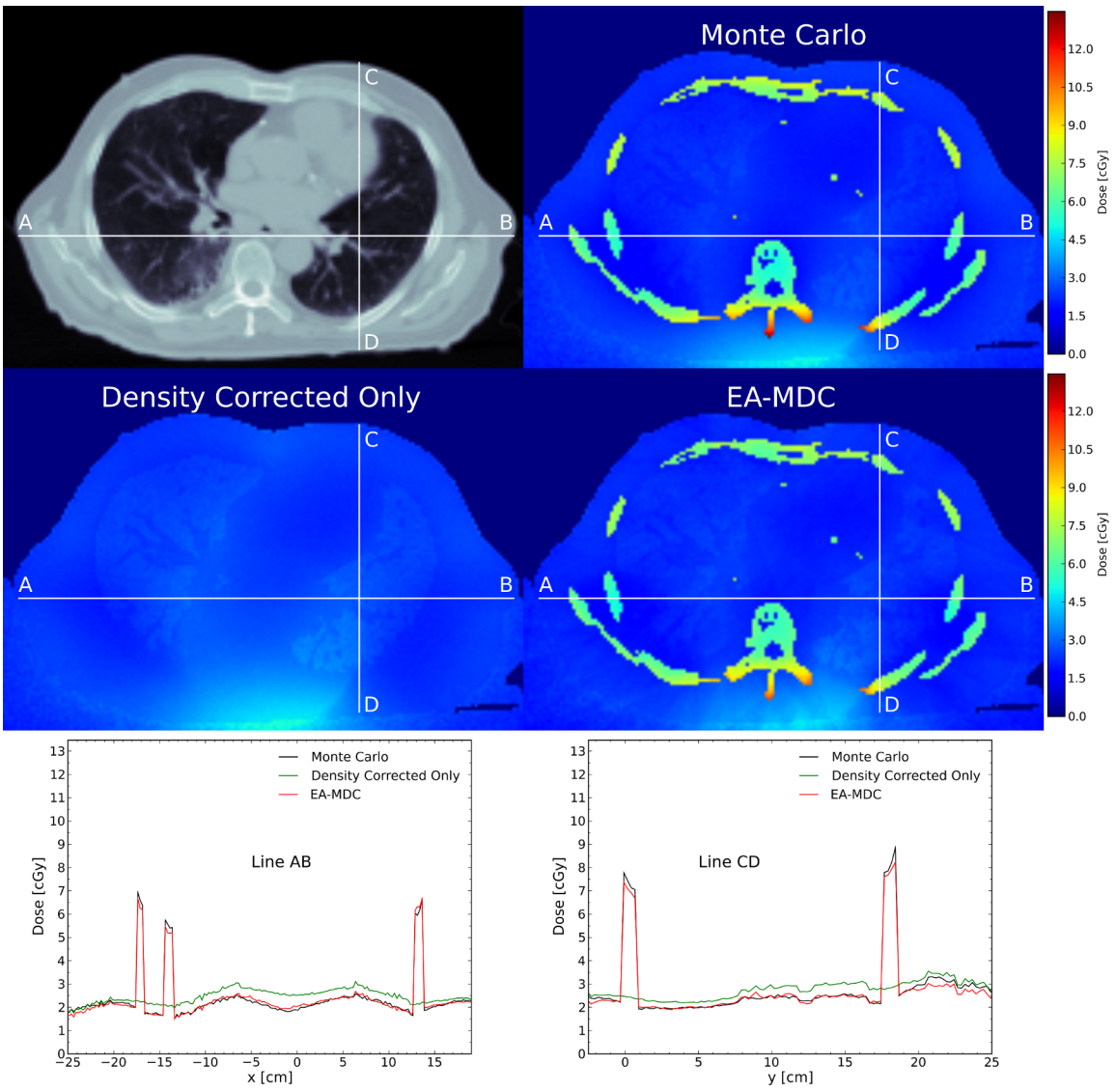

Figure III.13: Single kV-CBCT scan dose planes and line profiles for an axial slice through the thorax of the Adult Chest 2 patient. The dose to the lungs is accurately calculated with the MDC-EA calculation, even though the soft-tissue correction factor curve is used for lung tissue voxels. (Reproduced from [66] with permission)

Table III.5: Mean dose to bone, soft-tissue, and lung voxels in cGy for each patient dose calculation performed with the Monte Carlo (MC) technique, the density-corrected-only (DCO) technique, and the MDC-EA technique. Doses shown are for the volume irradiated by a single kV-CBCT scan performed using the acquisition techniques shown in Table III.4. (Reproduced from [66] with permission)

	Bone Voxels			Soft-Tissue Voxels			Lung Voxels		
Patient	MC	DCO	MDC-EA	MC	DCO	MDC-EA	MC	DCO	MDC-EA
Adult H&N 1[a]	15.72	6.70	15.85	5.01	6.06	5.13	–	–	–
Adult H&N 2	0.46	0.18	0.44	0.19	0.21	0.19	–	–	–
Adult H&N 3	0.47	0.19	0.44	0.16	0.18	0.16	–	–	–
Adult H&N 4	0.50	0.20	0.48	0.19	0.22	0.19	–	–	–
Pediatric H&N [a]	18.84	6.87	18.62	5.33	6.11	5.48	–	–	–
Adult Pelvis 1[a]	7.30	3.01	8.70	3.03	3.28	2.92	–	–	–
Adult Pelvis 2	3.68	1.63	3.69	1.56	1.72	1.49	–	–	–
Adult Pelvis 3	4.35	1.89	4.37	1.73	1.91	1.67	–	–	–
Adult Chest 1[a]	10.65	4.04	10.54	3.80	4.16	3.78	4.15	4.46	4.13
Adult Chest 2	1.34	0.51	1.30	0.43	0.48	0.43	0.47	0.50	0.45
Adult Chest 3	2.16	0.85	2.15	0.73	0.83	0.73	0.60	0.67	0.60
Adult Chest 4	1.24	0.45	1.20	0.41	0.46	0.41	–	–	–
Adult Legs	3.39	1.31	3.59	1.61	1.65	1.56	–	–	–
Pediatric Abd.	1.34	0.52	1.32	0.46	0.50	0.45	–	–	–

[a] Patients used to derive correction factor curves.

Table III.6: Mean and standard deviation dose errors for the MDC-EA dose calculations and density-corrected-only (DCO) calculations performed for a single kV-CBCT scan for each patient. Dose errors are normalized to the maximum dose to soft-tissue in the calculation volume for each patient. (Reproduced from [66] with permission)

	Mean Dose Error (%)				Standard Deviation Dose Error (%)			
	Bone Voxels		Soft-Tissue Voxels		Bone Voxels		Soft-Tissue Voxels	
Patient	MDC-EA	DCO	MDC-EA	DCO	MDC-EA	DCO	MDC-EA	DCO
Adult H&N 1 [a]	1.24	-82.09	0.82	8.18	8.98	28.05	2.56	6.61
Adult H&N 2	-0.58	-24.90	0.19	2.08	7.36	32.69	1.61	2.80
Adult H&N 3	-2.55	-32.70	-0.16	3.00	13.49	37.87	3.22	4.14
Adult H&N 4	-0.30	-28.62	0.39	2.71	8.47	38.77	1.85	3.73
Pediatric H& N [a]	-1.88	-102.65	0.55	4.50	9.05	27.83	2.25	4.26
Adult Pelvis 1 [a]	-1.56	-62.77	-1.26	3.48	8.77	31.91	2.49	3.25
Adult Pelvis 2	1.18	-38.38	-0.97	1.89	7.58	32.23	2.57	2.95
Adult Pelvis 3	1.22	-44.97	-0.96	2.38	8.46	36.72	2.75	3.37
Adult Chest 1 [a]	-0.95	-62.69	-0.15	3.48	6.49	31.91	1.60	3.34
Adult Chest 2	-2.11	-48.87	-0.45	2.74	7.22	35.08	2.47	3.26
Adult Chest 3	0.19	-47.87	0.13	2.78	6.26	39.17	1.90	3.27
Adult Chest 4	-1.50	-33.54	0.12	1.93	5.61	34.29	1.45	2.29
Adult Legs	1.29	-15.31	-0.56	0.44	4.19	19.79	1.24	1.15
Pediatric Abd.	-0.09	-22.72	-0.12	0.88	4.38	28.93	1.16	1.65

[a] Patients used to derive correction factor curves.

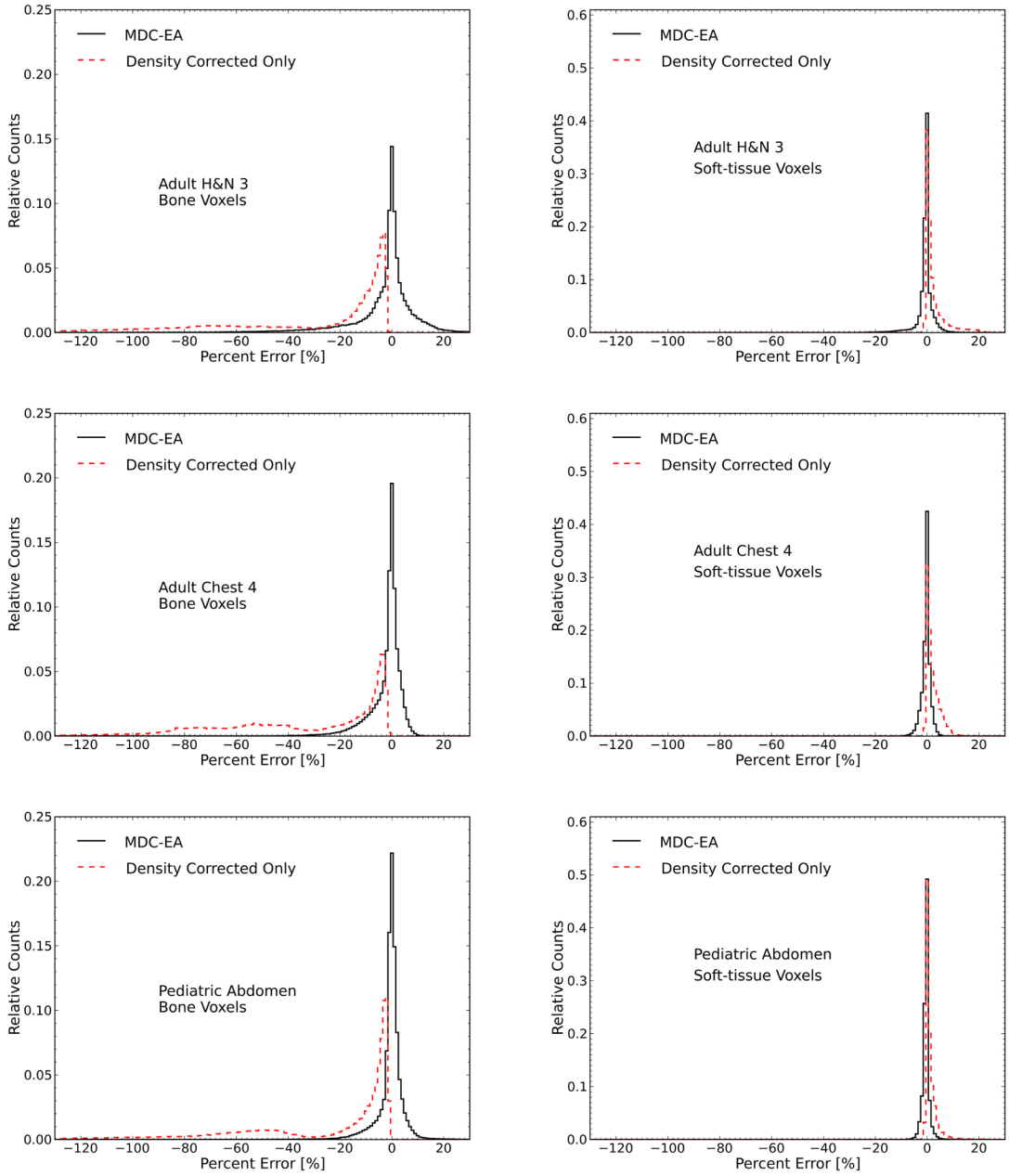

Figure III.14: Dose error histograms for bone voxels (left) and soft-tissue voxels (right) for an adult H&N (top), an adult chest (middle), and a pediatric abdomen (bottom) kV-CBCT scan. The errors are normalized to the maximum soft-tissue dose calculated with Monte Carlo. The long negative percent error tails shown for the density-corrected-only calculated bone dose distributions are typical for this calculation technique. (Reproduced from [66] with permission)

Figure III.14 shows example dose error histograms for the Adult H&N 3 (top), Adult Chest 4 (middle), and Pediatric Abdomen (bottom) patients. Bone error distributions (left), and soft-tissue error distributions (right) are shown for each patient for the density-corrected-only and MDC-EA calculations. The distributions were calculated relative to the maximum dose to soft-tissue for each patient. The density-corrected-only calculations produce bone error distributions with long negative dose error tails as the enhanced dose to bone from photoabsorption is not accounted for in these calculations. The MDC-EA calculation both centered the bone dose error distribution about 0% and significantly reduced the spread in the dose-error distribution, as was indicated in Table III.6. Similar results are shown for soft-tissue, though the magnitude of dose correction is less than that for bone.

Figure III.15 shows dose-volume histograms (DVHs) for bone and soft-tissue structures for the Adult H&N 3 (top), Adult Pelvis 2 (middle), and Adult Chest 4 patients (bottom). Distributions for the spine, femoral head, ribs, parotid gland, bladder and lung are shown. The soft-tissue structures tend to have homogeneous dose distributions, whereas the dose distributions of bony structures are by comparison inhomogeneous. The MDC-EA is capable of accurately accounting for the medium-dependent effect, reproducing the dose distributions to individual organs for each patient despite the disparate anatomies surrounding these structures, and is a significant improvement over the density-corrected-only calculations.

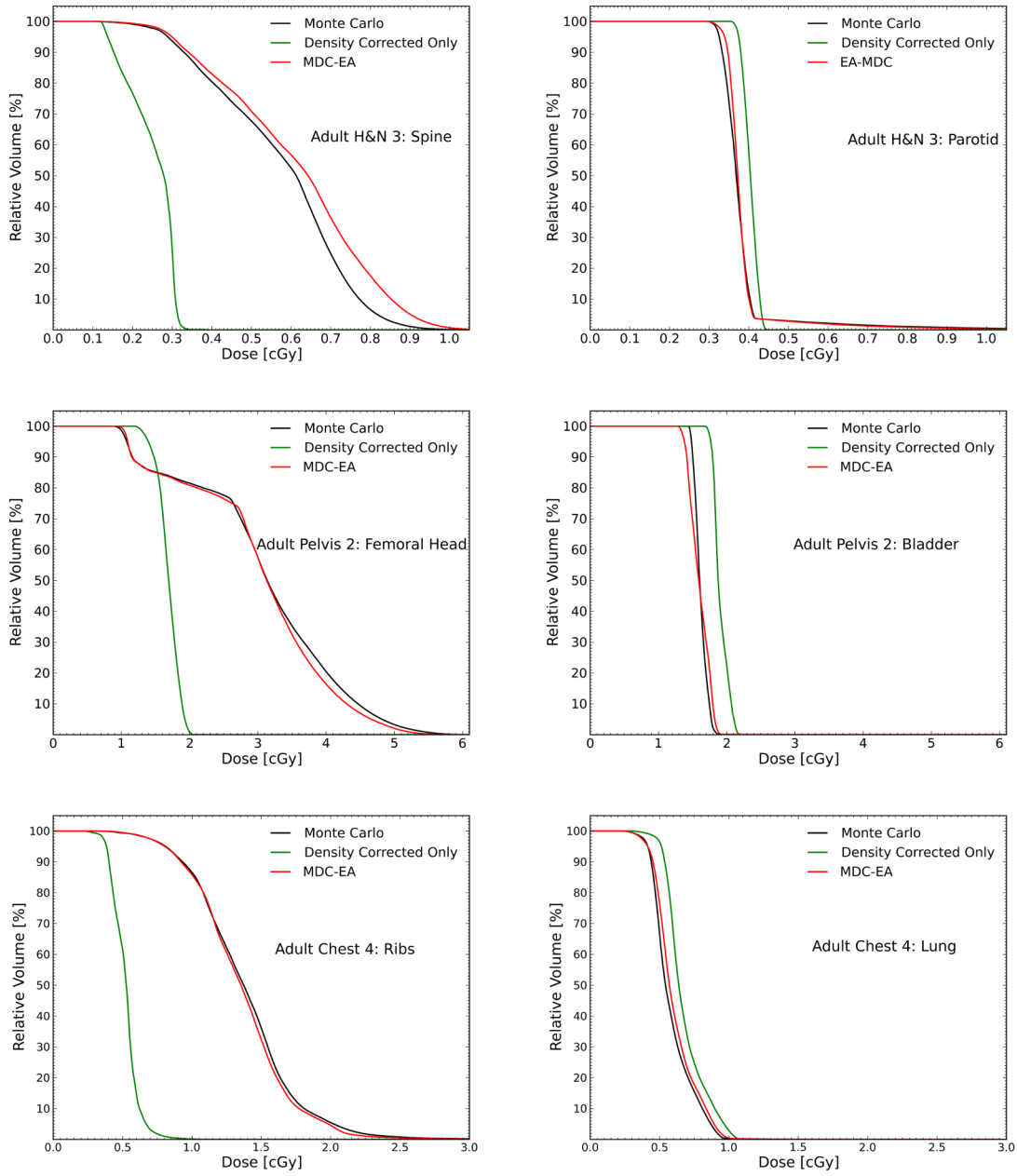

Figure III.15: DVHs calculated for bony and soft-tissue structures of three patients in this study. The density-corrected-only calculation results in significant underestimation of bone dose and overestimates the soft-tissue structure dose. The MDC-EA accurately reproduces the dose distributions for each structure of each patient using a single set of correction factor curves to correct the density-corrected-only distributions. (Reproduced from [66] with permission)

III.2.4 Discussion and conclusions

The new correction method was tested for imaging dose calculations for patients resulting from different kV-CBCT acquisition techniques. The accuracy of this new approach was compared with the Monte Carlo method, which is regarded as the gold standard. For all patients studied, the new approach resulted in mean dose errors of less than 3%. This is in contrast to currently available density corrected methods which resulted in mean errors of up to -103% for bone and 8% for soft-tissue. A limitation to this benchmark is that only four media were used in the Monte Carlo simulations: air, lung, soft-tissue, and cortical bone. This amounts to neglecting the differences in absorption characteristics between adipose tissue and soft-tissue, and between cortical bone and the bone spongiosa consisting of trabecular bone and red bone marrow. The difference in absorption between different soft tissues and between spongiosa and cortical bone may be accounted for by using a second-order correction factor that characterizes the differences in absorption between the two materials

An additional source of error for this approach arises from tissue segmentation uncertainty. This difficulty is not unique to the proposed correction method; any calculation technique relying on tissue segmentation, including the Monte Carlo technique, is susceptible to errors in the segmentation process resulting from volume averaging, image noise, inter-patient variations of tissue densities, implanted prostheses, and image artifacts. Potential advancements in dual-energy CT could result in more accurate tissue segmentation [10], which would be particularly beneficial to kV dose calculations due to the steep dose gradients at the boundaries of atomic number inhomogeneities.

In this work, we applied the medium-dependent correction factors to density-

corrected-only dose distributions obtained by Monte Carlo simulation. It has been shown by Alaei et al. [5, 6] that model-based radiotherapy treatment planning systems are capable of calculating density-corrected-only dose-to-water distributions from kV x-rays. The new correction approach can thus be used in conjunction with a commissioned kV-CBCT x-ray beam in a model-based treatment planning system, such as demonstrated by Alaei et al. [3], to accurately calculate the radiation dose from kV-CBCT without the use of Monte Carlo. The new approach thus has potential to extend the applicability of current and widely available radiotherapy treatment planning systems to accurately calculate the radiation dose to patients from kV x-rays. In chapter IV we present results of dose-to-medium calculations using the MDC-EA to correct dose-to-water distributions obtained with the algorithm developed in chapter II.

The correction method proposed here has numerous advantages over existing methods to calculate dose from kV x-rays including in-medium effects. The main advantage is that model-based dose calculation algorithms are widely used in commercial radiotherapy treatment planning systems, which makes accounting for the additional dose to patients resulting from repeated image guidance procedures readily feasible. Secondly, a simple correction method based on multiplying the density-corrected-only dose to bone by the ratio of the bone-to-water mass-energy absorption coefficients has been shown to be inaccurate since it is difficult to characterize *a priori* the energy spectrum at a given voxel for complicated geometries, such as volumes based on patient CT data [3]. Furthermore, the simple correction method does not correct the dose to soft-tissues in the vicinity of bone that are irradiated by a reduced fluence relative to the uncorrected calculation. Another empirical correction method, the Medium-Dependent Correction-Direct Approach (MDC-DA) has been proposed by Ding et al. [35] which takes into account the effects of photoabsorption in

bone on the dose-distribution including corrections for bone and soft-tissue. This method has been shown to be accurate for patient dose calculation when using empirically parameterized correction factors specifically obtained for a particular imaging site and patient size; however separate model parameters must be used for each permutation of imaging site, patient size, and beam quality, making implementation difficult in practice.

It is worth noting that the calculation speed of the new approach is about two orders of magnitude faster than the Monte Carlo method. For example, the calculation times required to generate the correction factors using a single Intel Pentium D 3.73 GHz processor ranged from 3.2 minutes for the pediatric H&N patient (538,428 voxels calculated in a CT voxel space of 100×140×140 voxels) to 27.0 minutes for Adult Pelvis 2 (3,395,577 voxels calculated in a CT voxel space of 176×200×200 voxels). Dose-to-water calculations performed using a commissioned kV-CBCT beam in the Philips PINNACLE treatment planning system v8.0 (Philips Medical Systems, Milpitas, CA) add 30-60 minutes to the calculation using a serial computation. Our implementation of the MDC-EA algorithm could easily be parallelized, providing a reduction in calculation time proportional to the number of processors used. The Monte Carlo simulations used in this study had calculation times ranging from four to five days on a single processor.

In conclusion, we have presented a new approach of using Monte Carlo techniques to obtain empirical medium-dependent correction factors. It is seen that the correction factors can be expressed as a function of a single quantity, called the effective bone depth, which is a measure of the amount of bone that an x-ray beam must penetrate to reach a voxel. Due to the manner in which the effective bone depth is calculated, this method is able to take into account the effects of both the attenuation characteristics of the absorbing media and the changes to the energy spectrum of the incident kV x-rays as they traverse through

different media. This new approach has potential to overcome the accuracy deficiency of model-based dose calculation algorithms for kV beams and to extend current model-based calculation algorithms used in commercial treatment planning systems to calculate the additional radiation exposure resulting from repeated daily imaging guidance procedures that use diagnostic energy photon beams.

IV Validation of the algorithm for the calculation of radiation dose to real patients from x-ray imaging procedures

IV.1 Introduction

In chapter II we presented a new model-based convolution/superposition algorithm to calculate the dose to water-equivalent media from kilovoltage x-ray beams, and presented the results of applying the algorithm to simple geometric phantoms. In chapter III we developed two methods to determine medium-dependent correction factor distributions to convert dose-to-water distributions to dose-to-medium distributions that account for the effects of photoabsorption in bone. These correction factor distributions were applied to dose-to-water calculations performed with the Monte Carlo technique to obtain dose-to-medium distributions. Benchmarking these correction methods was done by comparing these dose-to-medium distributions to Monte Carlo calculated dose-to-medium distributions.

In this chapter we implement the model-based convolution/superposition dose calculation algorithm developed in chapter II to calculate dose-to-water distributions for radiotherapy patients resulting from kV-CBCT imaging and single-angle projection imaging. We then obtain dose-to-medium distributions by correcting these dose-to-water distributions using the MDC-EA algorithm. These calculations are benchmarked against dose distributions obtained using the Monte Carlo technique.

Dose calculations for these procedures are of importance as they deliver additional radiation dose to patients that is not accounted for in the treatment planning process. They are also potentially repeated daily for as many as 25-40 treatments, which can result in

significant radiation exposure. As the dose from image guidance is added to regions receiving high therapeutic doses with inhomogeneous distributions, it is necessary to have accurate three-dimensional radiation dose calculations for kV imaging procedures to facilitate dose summation. There are a multitude of studies that have experimentally measured and/or calculated the imaging dose from IGRT [24, 28, 30, 33, 38, 51, 60, 77, 79], however, no method is currently employed in routine clinical practice to calculate the additional dose to patients from these procedures.

IV.2 Methods

The dose calculations in this chapter are performed using the algorithms developed in chapters II and III. The dose-to-medium distribution is obtained by multiplying the dose-to-water matrix by the medium-dependent correction factor distribution:

$$D_{\text{medium}}(x,y,z) = MDC(x,y,z) \times D_{\text{water}}(x,y,z). \tag{IV.1}$$

The dose-to-water distribution is calculated using the model-based convolution/superposition algorithm developed in chapter II. For patient dose calculations from kV-CBCT the rotation of the x-ray source was discretized into a finite number of incident beams separated by 5° . Dose-to-water calculations were individually performed for each beam and combined to generate the total dose-to-water distribution.

The medium-dependent correction factor distributions were obtained using the MDC-EA algorithm developed in chapter III. Correction factor distributions for the full 360° scans were obtained by calculating the effective bone depth along 16 incident rays. The standard dose head technique utilizes a 200° posterior scan which was modeled with 10 incident rays to calculate the effective bone depth. For the single-angle projection imaging

calculation a single ray incident parallel to the x-ray beam was used to calculate the effective bone depth.

The Monte Carlo calculations presented in this chapter were performed as described by Ding et al. [28, 34]. The x-ray beams were simulated using the BEAMnrc code [68], and dose calculations were performed with the DOSXYZnrc usercode [53, 78]. Dose-to-medium calculations were performed with consideration of four materials: air, lung, soft-tissue, and cortical bone. The material type was assigned to each voxel of the CT data based on the physical density of the voxel, which was determined from a CT number to density calibration curve. The density ranges for each material were 0.01-0.044 g/cm^3 for air, 0.044-0.302 g/cm^3 for lung, 0.302-1.101 g/cm^3 for soft tissue, and 1.101-2.088 g/cm^3 for bone [78]. Dose-to-water calculations were performed by setting all materials in the calculation volume to water and scaling the density of each voxel according to the CT number to density calibration curve.

The simulated x-ray beams were from the Varian on-board imager (OBI) system integrated into a Trilogy^{TM}linear accelerator (Varian Medical Systems, Palo Alto, CA). The acquisition techniques used were the Varian OBI version 1.4 standard-dose head, pelvis, and low-dose thorax techniques described by Ding et al. [34]. The standard-dose head technique uses the full-fan bowtie filter, while the pelvis and low-dose thorax techniques use half-fan bowtie filter. The x-ray energies are 100 kVp for the head technique, 110 kVp for the thorax, and 125 kVp for the pelvis.

IV.3 Results

Figures IV.1–IV.3 show dose calculation results for a kV-CBCT scan taken of a male pelvis using the pelvis x-ray beam, an adult head imaged with the standard-dose head

technique, and a female breast cancer patient set up on a breast board imaged with the low-dose thorax technique. For the pelvis and chest calculations 72 incident beams separated by 5° were used for the model-based dose-to-water calculation. The head scan is done with a 200° posterior source rotation spanning from the patient right anterolateral side to the left lateral side. The model-based dose calculation for this scan utilized 41 incident beams separated by 5° . The dose-to-water distributions all show excellent agreement with the Monte Carlo dose-to-water calculations.

The dose-to-medium distributions were calculated for each patient using the MDC-EA to correct the dose-to-water distributions for the effects of bone on the dose distribution. The dose-to-medium results show the enhanced dose to bone due to photoabsorption, and the decreased dose to the surrounding soft tissues as a result of the corresponding decrease in photon fluence in these areas. The dose to bone is typically on the order of 2–3 times greater than the dose to the surrounding soft tissue. The dose-to-medium calculations show acceptable accuracy compared to the Monte Carlo calculations.

Similar calculations were performed for kV-CBCT scans of additional pelvis, head, and chest patients. Table IV.1 shows the mean and standard deviation dose errors for the dose-to-water calculations for each patient, normalized to the maximum dose-to-water in the irradiated volume. Dose errors were calculated relative to the Monte Carlo dose-to-water distributions to reveal the accuracy of the convolution/superposition model-based method alone. Voxels that are superior or inferior to the primary beam were excluded from the calculation of the mean and standard-deviation error. The results show mean dose errors less than 0.3% for each patient. Standard deviation dose errors were within 2.0% for the pelvis scans, 2.6% for the chest, and 4.1% for the H&N. The results shown in Figures IV.1-IV.3 correspond to the patients labeled Pelvis 2, Chest 2, and H&N 2 respectively.

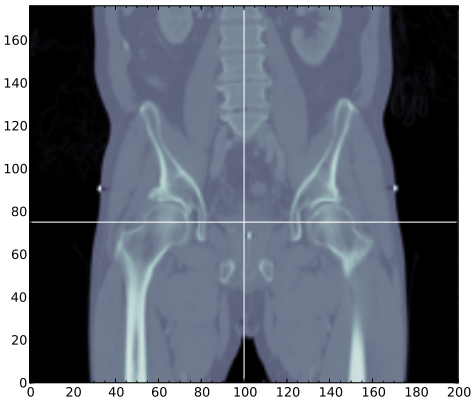

(a) Coronal view of patient CT data

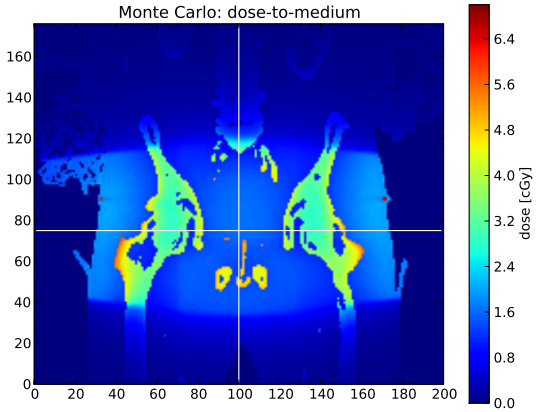

(b) Monte Carlo dose calculation

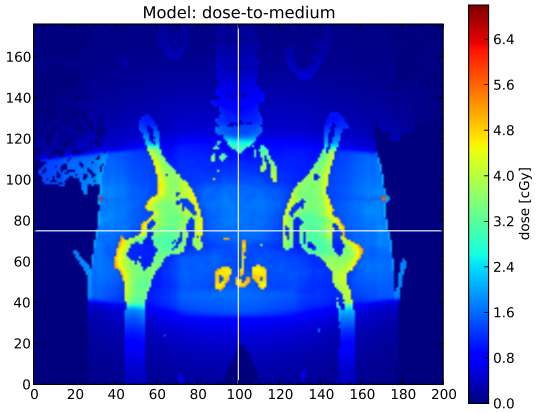

(c) Model-based dose calculation

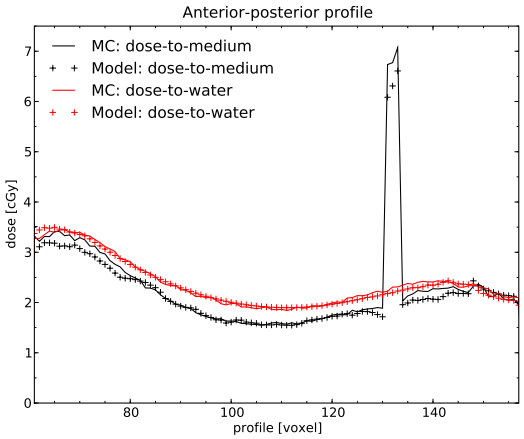

(d) Dose profile along anterior-posterior axis

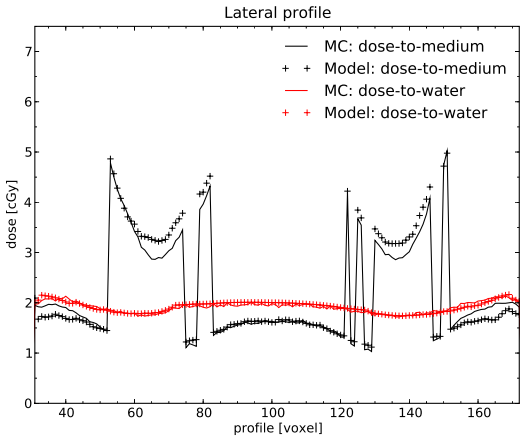

(e) Lateral dose profiles

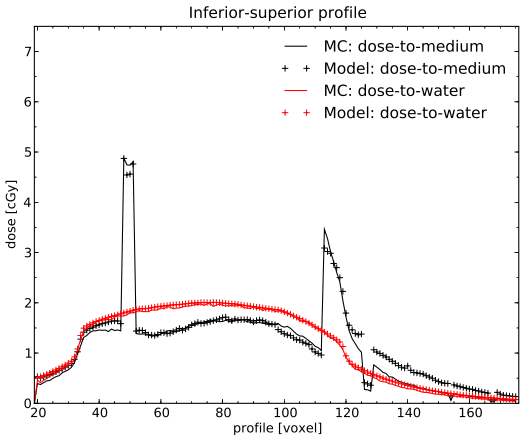

(f) Inferior-superior dose profiles

Figure IV.1: Results for calculations performed for the standard-dose pelvis kV-CBCT beam irradiating an adult male pelvis patient.

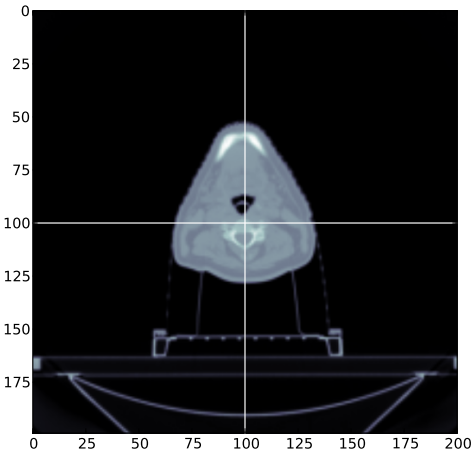

(a) Transverse view of patient CT data

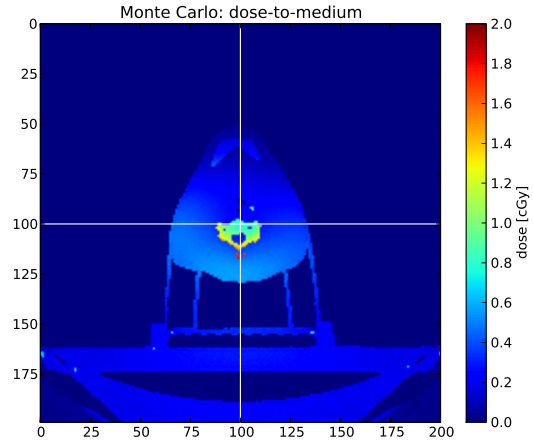

(b) Monte Carlo dose calculation

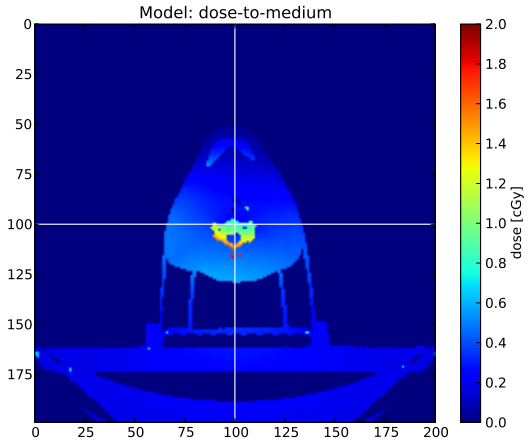

(c) Model-based dose calculation

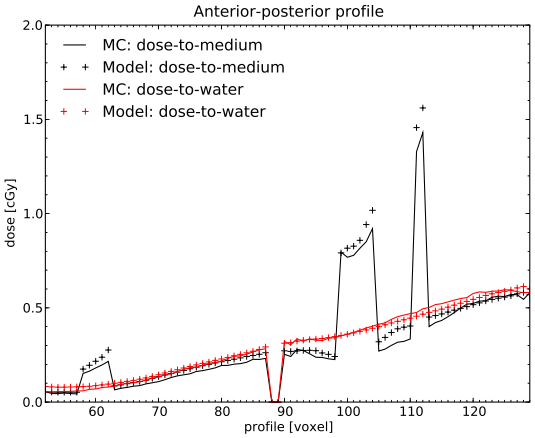

(d) Dose profile along anterior-posterior axis

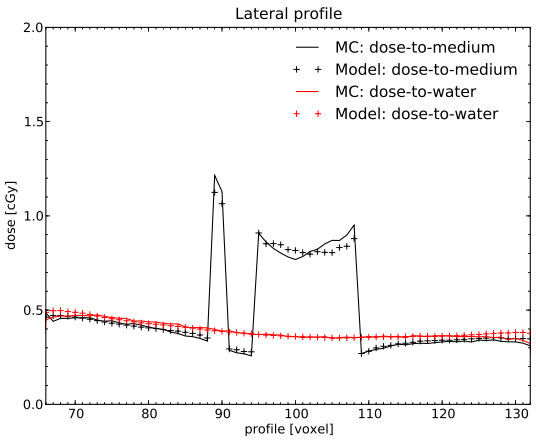

(e) Lateral dose profiles

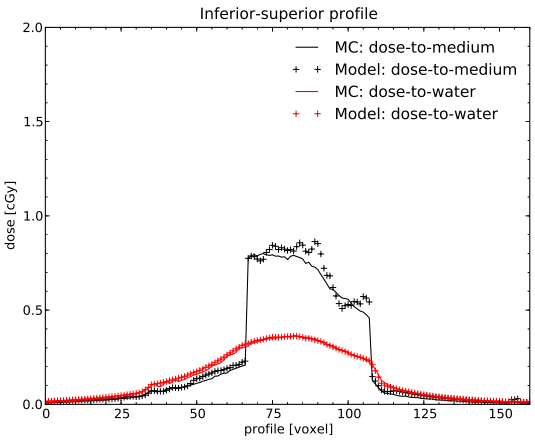

(f) Inferior-superior dose profiles

Figure IV.2: Results for calculations performed for the standard-dose head kV-CBCT beam irradiating an adult head. The x-ray beam rotates posteriorly around the patient resulting in the observed dose gradient in the anterior-posterior direction.

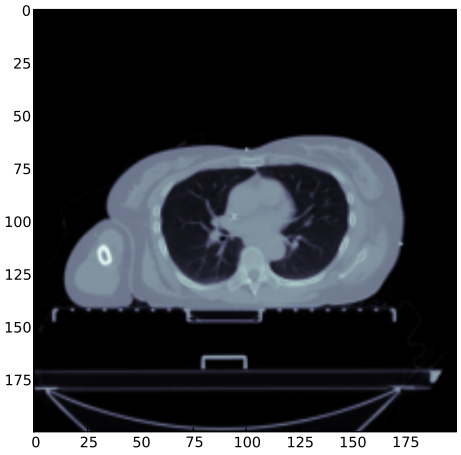

(a) Transverse view of patient CT data

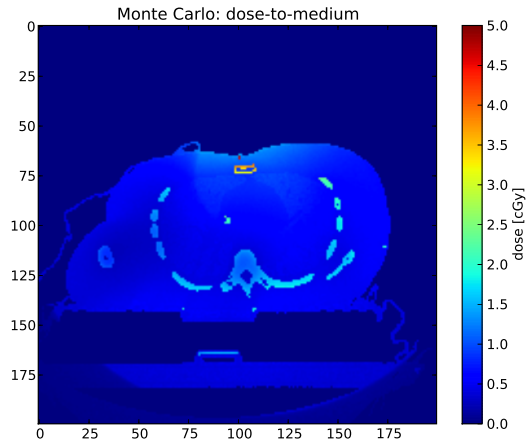

(b) Monte Carlo dose calculation

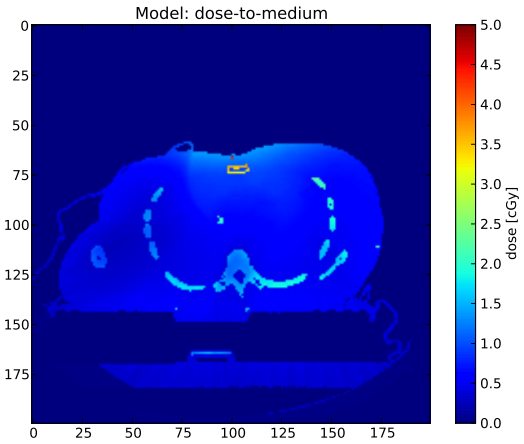

(c) Model-based dose calculation

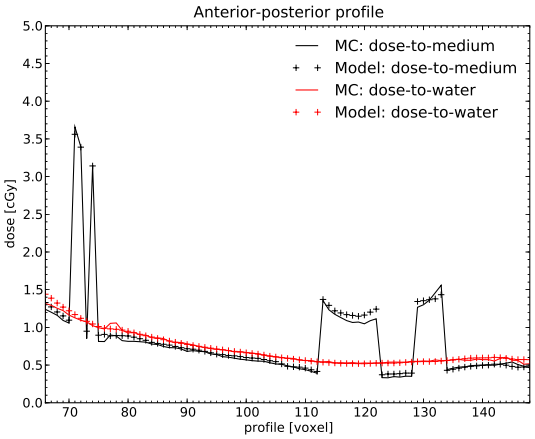

(d) Dose profile along anterior-posterior axis

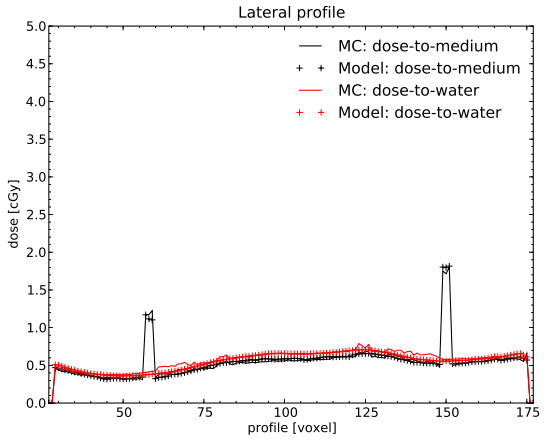

(e) Lateral dose profiles

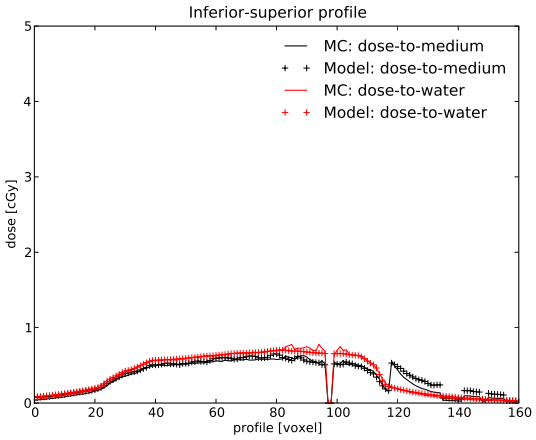

(f) Inferior-superior dose profiles

Figure IV.3: Results for calculations performed for the low-dose thorax kV-CBCT beam irradiating a female breast patient set up on a breast board.

Table IV.1: Relative dose errors for the model-based dose-to-water calculation relative to the Monte Carlo dose-to-water calculation. Dose errors are normalized to the maximum dose-to-water in the irradiated volume.

Patient	Mean dose error (% $\pm$ 1 σ)
Pelvis 1	-0.1 $\pm$ 2.0
Pelvis 2	-0.3 $\pm$ 1.7
Chest 1	-0.3 $\pm$ 2.7
Chest 2	-0.2 $\pm$ 2.4
H&N 1	-0.3 $\pm$ 3.0
H&N 2	-0.1 $\pm$ 3.0
H&N 3	-0.2 $\pm$ 4.1

Table IV.2 shows mean and standard deviation dose errors for the patient dose calculations compared to the Monte Carlo dose-to-medium calculations. Results are shown for the model-based calculation alone, and for the model-based calculation corrected with the MDC-EA. Dose errors were separately calculated for bone, soft tissue, and lung voxels, and are normalized to the maximum dose to soft tissue in the irradiated volume. The uncorrected dose-to-water distributions show significant underestimation of the dose to bone, with an average dose error of -60.2%. Dose to soft tissues, on the other hand, is overestimated by an average of 5.1% across all patients. The average lung voxel dose error for these calculations is 1.7%. The corrected dose-to-medium distributions have average bone, soft tissue, and lung dose errors of 0.0%, -0.3%, and -0.9% respectively, showing considerable improvement over the model-based calculation alone. Mean dose errors range from -3.6% to 2.5% for bone, -2.4% to 1.3% for soft tissue, and -1.7 to -0.3% for lung. Bone voxels have the largest deviation in dose error, with an average standard deviation of 10.6% for the corrected dose-to-water calculation. The average standard deviation dose errors are 3.0% for soft tissue and 2.8% for lung.

We also performed dose calculations for single-angle projection imaging procedures in order to illustrate the suitability of the new algorithm for imaging modalities such as fluoroscopy that make use of single incident beams. Figures IV.4, IV.5, and IV.6 show

Table IV.2: Relative dose errors for the model-based calculation relative to the Monte Carlo dose-to-medium calculation. Results for the model-based calculation that have been corrected for medium-dependent effects, as well as uncorrected dose-to-water results are shown relative to the maximum dose to soft tissue in the irradiated volume.

	D_w corrected with MDC-EA (% ± 1 σ)			Uncorrected D_w(% ± 1 σ)		
Patient	Bone	Soft tissue	Lung	Bone	Soft tissue	Lung
Pelvis 1	2.5 ± 11.3	-1.8 ± 3.7	-1.7 ± 3.8	-67.4 ± 34.9	6.0 ± 4.3	-0.2 ± 2.7
Pelvis 2	2.0 ± 10.5	-2.4 ± 3.5	-1.1 ± 2.5	-63.5 ± 25.3	5.3 ± 4.0	-0.0 ± 1.6
Chest 1	-1.2 ± 10.4	0.4 ± 2.5	-1.3 ± 2.6	-79.3 ± 28.5	6.9 ± 4.1	3.6 ± 3.3
Chest 2	1.4 ± 6.7	1.3 ± 1.6	-1.7 ± 2.0	-47.6 ± 39.6	4.2 ± 2.8	2.2 ± 2.5
H&N 1	-1.0 ± 9.6	0.3 ± 2.9	-0.8 ± 2.2	-44.3 ± 43.4	3.9 ± 5.2	1.6 ± 3.9
H&N 2	-3.6 ± 11.4	-0.1 ± 3.0	-0.3 ± 2.8	-51.1 ± 37.9	4.2 ± 4.4	1.5 ± 3.8
H&N 3	-0.3 ± 14.2	0.4 ± 3.6	0.4 ± 3.4	-67.9 ± 35.2	5.5 ± 6.9	3.1 ± 6.1

example dose calculation results for simulated single projection imaging procedures done on a head-and-neck, thoracic, and pelvis patients (patients H&N 1, Chest 1, and Pelvis 1 respectively). In each calculation the x-ray beam is anteriorly incident on the patient. The x-ray beam used for these simulations was the pelvis beam.

IV.4 Discussion and conclusions

The new model-based dose calculation method for kilovoltage x-rays was tested for calculating the imaging dose to patients from kV-CBCT imaging and single-angle projection imaging. Used in conjunction with the MDC-EA to account for medium-dependent effects, the new model-based approach resulted in mean dose errors of less than 4% for bone and 3% for soft tissues across all patients studied. Of note is that the medium-dependent correction method adds minimal calculation time to the dose-to-water calculation as the time consuming ray-tracing step can be used for both calculations. The dose-to-medium distributions obtained in this chapter indicate that the dose calculation algorithm developed in this dissertation has acceptable accuracy for the application of aggregating the radiation dose from kV-CBCT image guidance procedures and single-angle projection imaging with

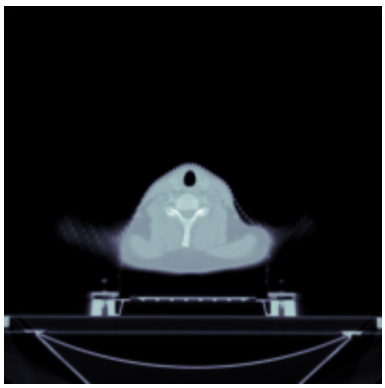

(a) Transverse view of patient CT data

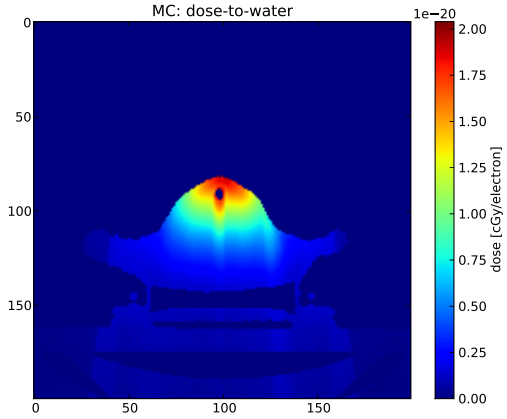

(b) Monte Carlo dose-to-water

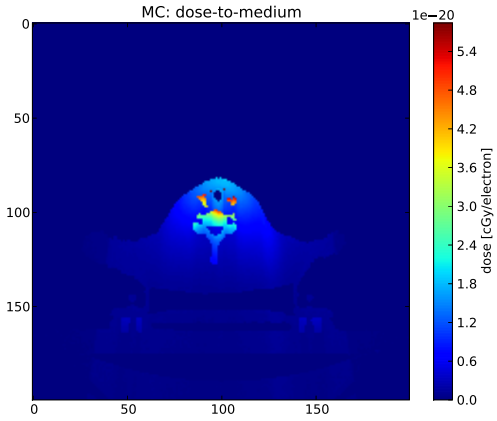

(c) Monte Carlo dose-to-medium

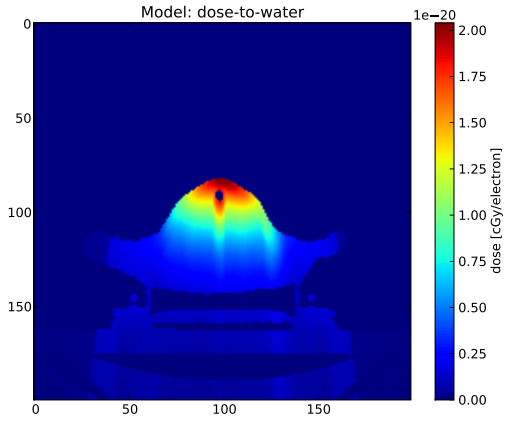

(d) Model-based dose-to-water

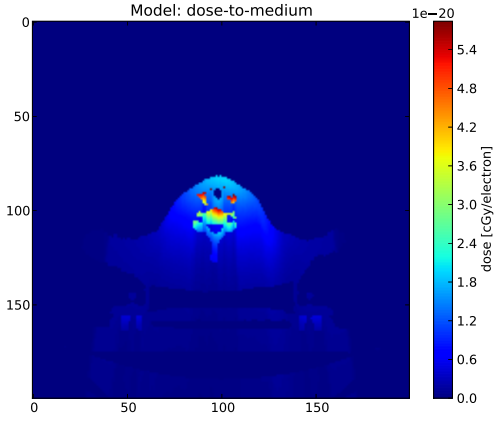

(e) Model-based dose-to-medium

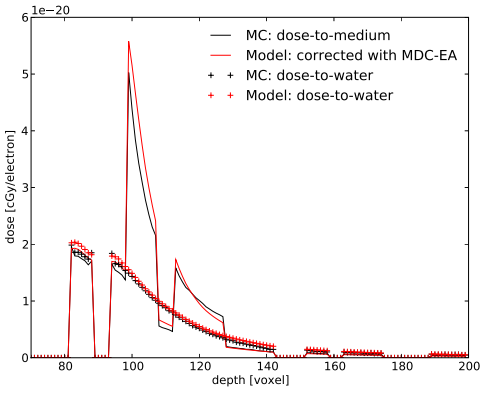

(f) Anterior-to-posterior dose profile along the central axis of the x-ray beam

Figure IV.4: Dose calculation results for a single anterior-to-posterior x-ray beam incident on a head-and-neck patient (H&N 1).

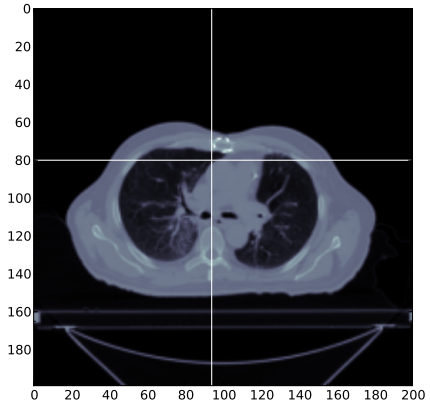

(a) Transverse view of patient CT data

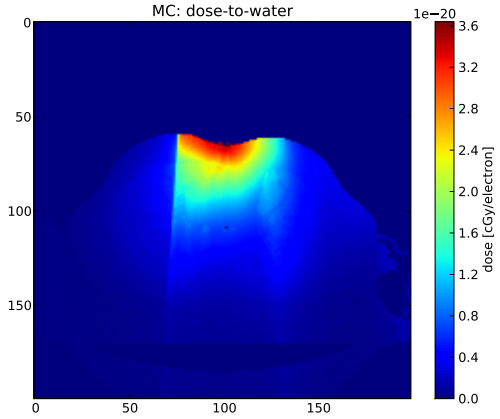

(b) Monte Carlo dose-to-water

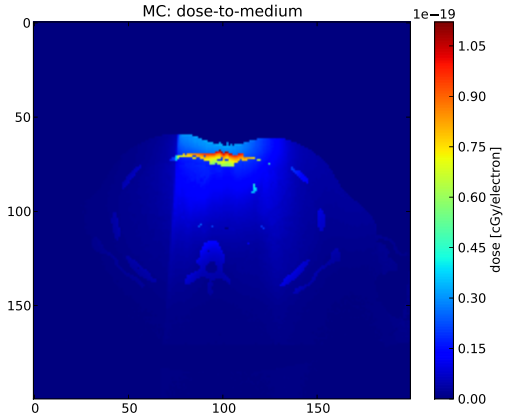

(c) Monte Carlo dose-to-medium

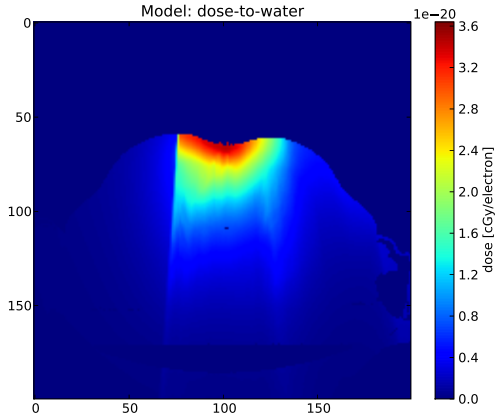

(d) Model-based dose-to-water

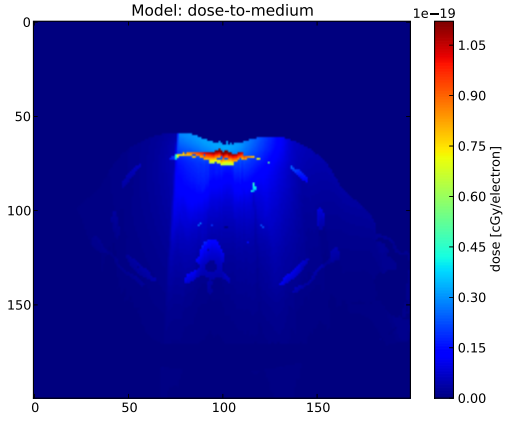

(e) Model-based dose-to-medium

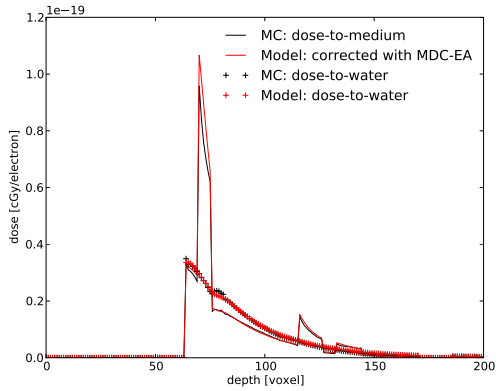

(f) Anterior-to-posterior dose profile along the central axis of the x-ray beam

Figure IV.5: Dose calculation results for a single anterior-to-posterior x-ray beam incident on a chest patient (Chest 1).

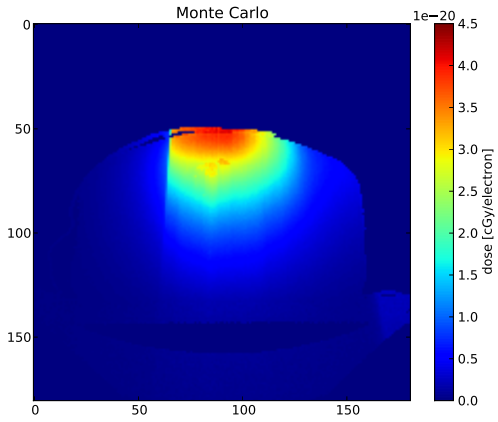

(a) Monte Carlo dose-to-water

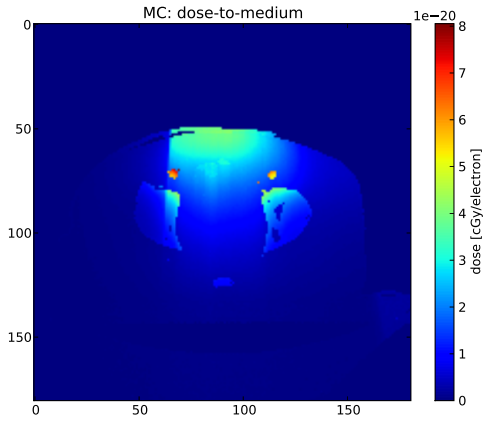

(b) Monte Carlo dose-to-medium

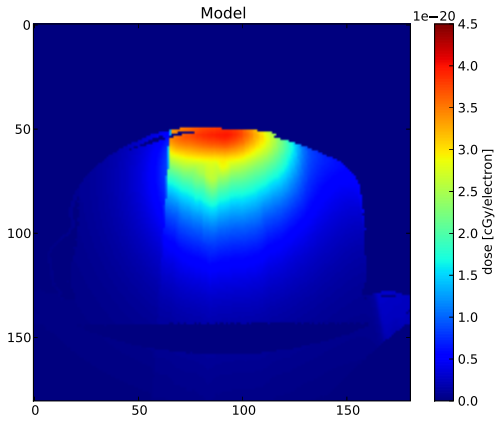

(c) Model-based dose-to-water

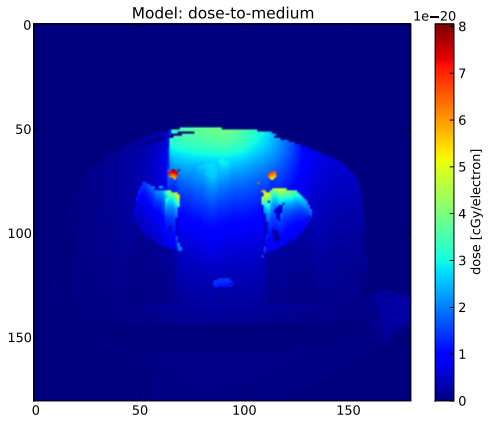

(d) Model-based dose-to-medium

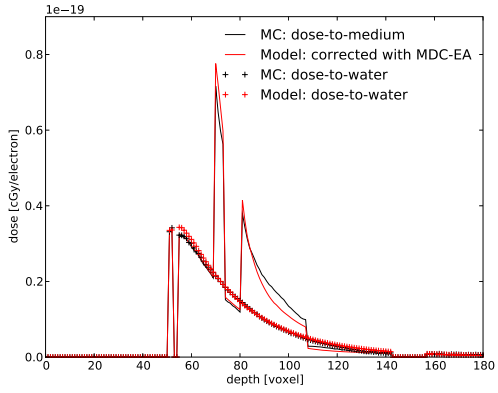

(e) Anterior-to-posterior dose profile through the femoral head

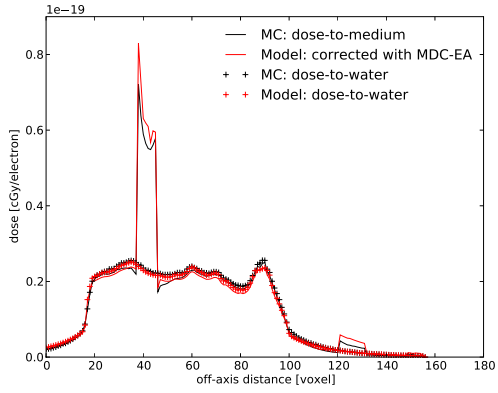

(f) Superior-inferior dose profile

Figure IV.6: Dose calculation results for a single anterior-to-posterior x-ray beam incident on a male pelvis patient (Pelvis 1).

the therapeutic dose delivered during radiotherapy.

The results obtained for the single-angle projection imaging cases are indicative of the calculation accuracy that can be expected when applying this algorithm to calculate the radiation dose from superficial x-ray therapies since the energy of superficial x-ray beams is comparable to the energies of the beams used to generate the results in this section. As these x-ray beams are generally collimated to sizes that are small relative to the area of the body being irradiated, the effects of phantom size on kernel generation should be minimized in these situations. One potential difficulty in applying this algorithm to superficial x-ray therapy calculations is that the area treated can be irregular in shape. For instance, the treatment of a basal cell carcinoma on the nose may involve a beam that has an oblique incidence. As Figure II.10 shows, the model-based calculation may overestimate the dose to the surface of the patient in these situations.

V Summary and conclusions

This work presents the first model-based dose calculation algorithm designed for kilovoltage x-ray beams that includes the effects of photoabsorption in bone on the dose distribution. Model-based convolution/superposition dose calculations are commonplace in radiation therapy treatment planning systems where they are used to calculate patient specific dose distributions resulting from megavoltage x-ray beams. The algorithm presented in this dissertation extends the applicability of this class of algorithm to accurately calculate the radiation dose to patients from the multitude of kilovoltage x-ray procedures used in medicine including superficial and orthovoltage x-ray therapies, image-guidance procedures in radiation therapy, and diagnostic procedures such as projection x-ray imaging and x-ray computed tomography.

The new algorithm calculates radiation dose in two main steps: (1) a model-based convolution/superposition algorithm is used to calculate the dose assuming that all media in the calculation volume is equivalent in composition to water, but with density equal to the actual media; (2) a medium-dependent correction method is used to obtain correction factor distributions that account for perturbations to the dose distribution due to photoabsorption of the x-ray beam in bone.

The dose-to-water calculation technique developed in this dissertation differs from previous work in that our approach is the first model-based convolution/superposition method designed from the ground up to calculate the dose from kilovoltage x-ray beams. Adopting the model-based calculation framework and limiting the applicability of the algorithm to the kilovoltage energy range has enabled us to invoke multiple approximations that drastically simplify dose calculation yet result in acceptable accuracy for clinical ap-

plications.

We presented two methods to obtain the medium-dependent correction factor: the Medium-Dependent Correction: Direct Approach, and the Medium-Dependent Correction: Effective Approach. The MDC-DA uses an empirical parameterization of the medium-dependent correction factor as a function of depth along rays incident on the patient parallel to the incident x-ray beam. This approach was shown to be accurate with the use of an average model-parameter set, but improvements could be made if separate model parameter sets were used for different imaging sites such as the head, thorax, and pelvis. The MDC-EA improved on the accuracy of the MDC-DA method by correlating the medium-dependent correction factor with a newly introduced quantity, the effective bone depth, that is easily calculated from patient CT images. This method is preferable to the MDC-DA as a single set of model parameters was sufficient to accurately calculate the medium-dependent correction factor distributions for all imaging sites studied.

The algorithm described in this work can be extended to dose calculations for arbitrary kilovoltage x-ray beams by fitting the dose-to-water model to Monte Carlo calculations as described in chapter II. For the x-ray beams studied in that chapter we found that we could adjust the model to fit each beam simply by adjusting the ratio of the scatter dose conversion factor to the primary dose conversion factor. For energies that differ significantly from the range studied here more significant changes to the model parameters may be necessary. Similarly, the MDC-EA model may require adjustment for x-ray beam energies that differ from those studied here as the bone-to-water mass-energy absorption coefficient ratio is highly dependent on energy. For the three beams included in chapter III, however, we found that we could use a single set of correction factor curves regardless of the kVp of the x-ray beam.

The algorithm developed in this work can be used to accurately extend model-based dose calculations to kilovoltage energy photon beams. The inability to account for medium-dependent effects has long been a shortcoming of model-based dose calculation algorithms. The algorithm presented in this work overcomes this deficiency, and makes model-based dose calculations a suitable alternative to the Monte Carlo calculation technique which is currently the only method available for kilovoltage energy dose calculation.

VI Appendix

VI.1 Summary of original contributions

In this section we summarize the original contributions to the dissertation that are attributable to the author. The dissertation research was performed under the guidance and supervision of Dr. George Ding, and many ideas are as a result of our close collaboration. The Monte Carlo calculations used within this work were all performed by Dr. George Ding.

The research culminating in this dissertation was performed during the period from 2008–2013. The author was enrolled as a full-time student in the Physics Ph.D. program at Vanderbilt University from June 2009 to August 2010. After this time, the author was employed full-time as a medical physicist at Centennial Medical Center in Nashville, TN, and completed the remainder of the dissertation research as a part-time student.

From 2008–2011 we investigated the medium-dependent correction methods presented in chapter III. During this time, the author developed and implemented the two algorithms presented in the dissertation: the MDC-DA, and the MDC-EA. The parameterization of the medium-dependent effects used in the MDC-DA, and the introduction of the effective bone depth to model these effects in the MDC-EA are attributable to the author. These algorithms were published in separate journal articles [35, 66].

From 2011–2013 we investigated the problem of calculating the dose to water-equivalent media. The dose-to-water calculation techniques were developed and implemented by the author including the parameterization of the dose deposition model, the monoenergetic approximation, introducing the effective density in the scatter dose calcula-

tion, and neglecting kernel tilting in the scatter dose calculation. The author implemented the ray-tracing algorithm and scatter dose convolution calculations to calculate the dose-to-water.

The author implemented the algorithms developed within the dissertation to calculate the radiation dose to real patients from x-ray imaging procedures. Benchmark calculations and analyses were carried out by the author for each of the algorithms presented to compare the accuracy of the model-based approach to Monte Carlo calculated dose distributions. At the time of writting the dissertation this work was being incorporated into a manuscript being prepared for submission for publication.

In addition to the journal articles resulting from the dissertation research, the work presented in this dissertation has been presented by the author at several national meetings of the American Association of Physicists in Medicine [64, 65, 67].

VII Bibliography

[1] S. Agostinelli. GEANT4—A simulation toolkit. *Nucl. Instrum. Methods Phys. Res. A*, 506:250–303, 2003.

[2] A. Ahnesjö. Collapsed cone convolution of radiant energy for photon dose calculation in heterogeneous media. *Med Phys*, 16:577–592, 1989.

[3] P. Alaei, G. Ding, and H. Guan. Inclusion of the dose from kilovoltage cone beam CT in the radiation therapy treatment plans. *Medical Physics*, 37(1):244–248, 2010.

[4] P. Alaei, B. J. Gerbi, and R. A. Geise. Generation and use of photon energy deposition kernels for diagnostic quality x rays. *Med Phys*, 26:1687–1697, Aug 1999.

[5] P. Alaei, B. J. Gerbi, and R. A. Geise. Evaluation of a model-based treatment planning system for dose computations in the kilovoltage energy range. *Med Phys*, 27:2821–2826, Dec 2000.

[6] P. Alaei, B. J. Gerbi, and R. A. Geise. Lung dose calculations at kilovoltage x-ray energies using a model-based treatment planning system. *Med Phys*, 28:194–198, Feb 2001.

[7] M. M. Aspradakis, R. H. Morrison, N. D. Richmond, and A. Steele. Experimental verification of convolution/superposition photon dose calculations for radiotherapy treatment planning. *Phys Med Biol*, 48:2873–2893, Sep 2003.

[8] J. V. Atherton and W. Huda. Energy imparted and effective doses in computed tomography. *Medical Physics*, 23(5):735–741, 1996.

[9] J. Baro, J. Sempau, Fernandez-Varea, J. M., and F. Salvat. PENELOPE—An algorithm for Monte-Carlo simulation of the penetration and energy-loss of electrons and positrons in matter. *Nucl. Instrum. Methods Phys. Res. A*, 100:31–46, 1995.

[10] M. Bazalova, J. F. Carrier, L. Beaulieu, and F. Verhaegen. Dual-energy CT-based material extraction for tissue segmentation in Monte Carlo dose calculations. *Phys Med Biol*, 53:2439–2456, May 2008.

[11] M. Bazalova and F. Verhaegen. Monte Carlo simulation of a computed tomography x-ray tube. *Phys Med Biol*, 52:5945–5955, Oct 2007.

[12] J. M. Boone. The trouble with CTDI_{100}. *Med Phys*, 34:1364–1371, Apr 2007.

[13] A. Boyer and E. Mok. A photon dose distribution model employing convolution calculations. *Med Phys*, 12:169–177, 1985.

[14] D. Brenner, C. Elliston, E. Hall, and W. Berdon. Estimated risks of radiation-induced fatal cancer from pediatric CT. *AJR Am J Roentgenol*, 176:289–296, Feb 2001.

[15] D. J. Brenner. Estimating cancer risks from pediatric CT: going from the qualitative to the quantitative. *Pediatr Radiol*, 32:228–223, Apr 2002.

[16] D. J. Brenner. Is it time to retire the CTDI for CT quality assurance and dose opti-

mization? *Med Phys*, 32:3225–3226, Oct 2005.

[17] D. J. Brenner, R. Doll, D. T. Goodhead, E. J. Hall, C. E. Land, J. B. Little, J. H. Lubin, D. L. Preston, R. J. Preston, J. S. Puskin, E. Ron, R. K. Sachs, J. M. Samet, R. B. Setlow, and M. Zaider. Cancer risks attributable to low doses of ionizing radiation: assessing what we really know. *Proc. Natl. Acad. Sci. U.S.A.*, 100:13761–13766, Nov 2003.

[18] D. J. Brenner and E. J. Hall. Risk of cancer from diagnostic X-rays. *Lancet*, 363:2192–2193, Jun 2004.

[19] D. J. Brenner and E. J. Hall. Computed tomography–an increasing source of radiation exposure. *N. Engl. J. Med.*, 357:2277–2284, Nov 2007.

[20] F. B. Brown. MCNP—A general Monte Carlo-particle transport code, version 5. Report LA-UR-03-1987, Los Alamos National Laboratory, Los Alamos, NM, 2003.

[21] M. J. Butson, T. Cheung, and P. K. Yu. Measurement of dose reductions for superficial x-rays backscattered from bone interfaces. *Phys Med Biol*, 53:N329–336, Sep 2008.

[22] A. K. Carlsson and A. Ahnesjo. Point kernels and superposition methods for scatter dose calculations in brachytherapy. *Phys Med Biol*, 45(2):357–382, Feb 2000.

[23] J. C. Chow. Cone-beam CT dosimetry for the positional variation in isocenter: a Monte Carlo study. *Med Phys*, 36:3512–3520, Aug 2009.

[24] J. C. Chow, M. K. Leung, M. K. Islam, B. D. Norrlinger, and D. A. Jaffray. Evaluation of the effect of patient dose from cone beam computed tomography on prostate IMRT using Monte Carlo simulation. *Med Phys*, 35:52–60, Jan 2008.

[25] Indra J. Das. Forward dose perturbation at high atomic number interfaces in kilovoltage x-ray beams. *Medical Physics*, 24(11):1781–1787, 1997.

[26] Indra J. Das and Kashmiri L. Chopra. Backscatter dose perturbation in kilovoltage photon beams at high atomic number interfaces. *Medical Physics*, 22(6):767–773, 1995.

[27] G. X. Ding. Energy spectra, angular spread, fluence profiles and dose distributions of 6 and 18 MV photon beams: results of monte carlo simulations for a varian 2100EX accelerator. *Phys Med Biol*, 47:1025–1046, Apr 2002.

[28] G. X. Ding and C. W. Coffey. Radiation dose from kilovoltage cone beam computed tomography in an image-guided radiotherapy procedure. *Int. J. Radiat. Oncol. Biol. Phys.*, 73:610–617, Feb 2009.

[29] G. X. Ding and C. W. Coffey. Beam characteristics and radiation output of a kilovoltage cone-beam CT. *Phys Med Biol*, 55:5231–5248, Sep 2010.

[30] G. X. Ding and C. W. Coffey. Dosimetric evaluation of the OneDoseTM MOSFET for measuring kilovoltage imaging dose from image-guided radiotherapy procedures. *Med Phys*, 37:4880–4885, Sep 2010.

[31] G. X. Ding, D. M. Duggan, and C. W. Coffey. Commissioning stereotactic radiosurgery beams using both experimental and theoretical methods. *Phys Med Biol*, 51:2549–2566,

May 2006.

[32] G. X. Ding, D. M. Duggan, and C. W. Coffey. Characteristics of kilovoltage x-ray beams used for cone-beam computed tomography in radiation therapy. *Phys Med Biol*, 52:1595–1615, Mar 2007.

[33] G. X. Ding, D. M. Duggan, and C. W. Coffey. Accurate patient dosimetry of kilovoltage cone-beam CT in radiation therapy. *Med Phys*, 35:1135–1144, Mar 2008.

[34] G. X. Ding, P. Munro, J. Pawlowski, A. Malcolm, and C. W. Coffey. Reducing radiation exposure to patients from kV-CBCT imaging. *Radiother Oncol*, 97:585–592, Dec 2010.

[35] G. X. Ding, J. M. Pawlowski, and C. W. Coffey. A correction-based dose calculation algorithm for kilovoltage x rays. *Med Phys*, 35:5312–5316, Dec 2008.

[36] R. L. Dixon. A new look at CT dose measurement: Beyond CTDI. *Medical Physics*, 30(6):1272–1280, 2003.

[37] R. L. Dixon, J. A. Anderson, D. M. Bakalyar, K. Boedeker, J. M. Boone, D. D. Cody adn R. Fahrig, D. A. Jaffray, I. S. Kyprianou, C. H. McCollough, M. F. McNitt-Gray, H. T. Morgan, R. L. Morin, K. D. Nakonechny, T. J. Payne adn R. J. Pizzutiello, B. T. Schmidt, A. J. Seibert, W. E. Simon, T. W. Slowey, S. H Stern, P. Sunde, T. L. Toth, and S. Vastagh. Report of AAPM Task Group 111: Comprehensive Methodology for the Evaluatuation of Radiation Dose in X-Ray Computed Tomography. Technical report, The American Association of Medical Physicists, February 2010.

[38] P. Downes, R. Jarvis, E. Radu, I. Kawrakow, and E. Spezi. Monte Carlo simulation and patient dosimetry for a kilovoltage cone-beam CT unit. *Med Phys*, 36:4156–4167, Sep 2009.

[39] A. Van Esch, L. Tillikainen, J. Pyykkonen, M. Tenhunen, H. Helminen, S. Siljamäki, J. Alakuijala, M. Paiusco, M. Iori, and D. P. Huyskens. Testing of the analytical anisotropic algorithm for photon dose calculation. *Medical Physics*, 33(11):4130–4148, 2006.

[40] M. Fippel. Fast Monte Carlo dose calculation for photon beams based on the VMC electron algorithm. *Medical Physics*, 26(8):1466–1475, 1999.

[41] I. Fotina, P. Winkler, T. Kunzler, J. Reiterer, I. Simmat, and D. Georg. Advanced kernel methods vs. Monte Carlo-based dose calculation for high energy photon beams. *Radiother Oncol*, 93:645–653, Dec 2009.

[42] J. Geleijns, M. Salvado Artells, P. W. de Bruin, R. Matter, Y. Muramatsu, and M. F. McNitt-Gray. Computed tomography dose assessment for a 160 mm wide, 320 detector row, cone beam CT scanner. *Phys Med Biol*, 54:3141–3159, May 2009.

[43] E. J. Hall and D. J. Brenner. Cancer risks from diagnostic radiology. *Br J Radiol*, 81:362–378, May 2008.

[44] H. Hansson, P. Bjork, T. Knoos, and P. Nilsson. Verification of a pencil beam based treatment planning system: output factors for open photon beams shaped with MLC or blocks. *Phys Med Biol*, 44:N201–207, Sep 1999.

[45] W. R. Hendee and E. R. Ritenour. *Medical Imaging Physics*. Wiley-Liss, New York, 4^{th} edition, 2002.

[46] http://zunzun.com. Online Curve And Surface Fitting, 2010.

[47] W. Huda and J. V. Atherton. Energy imparted in computed tomography. *Medical Physics*, 22(8):1263–1269, 1995.

[48] W. Huda, E. L. Nickoloff, and J. M. Boone. Overview of patient dosimetry in diagnostic radiology in the USA for the past 50 years. *Med Phys*, 35:5713–5728, Dec 2008.

[49] W. Huda and K. M. Ogden. Comparison of head and body organ doses in CT. *Phys Med Biol*, 53:N9–N14, Jan 2008.

[50] W. Huda, A. Sterzik, S. Tipnis, and U. Joseph Schoepf. Organ doses to adult patients for chest CT. *Medical Physics*, 37(2):842–847, 2010.

[51] M. K. Islam, T. G. Purdie, B. D. Norrlinger, H. Alasti, D. J. Moseley, M. B. Sharpe, J. H. Siewerdsen, and D. A. Jaffray. Patient dose from kilovoltage cone beam computed tomography imaging in radiation therapy. *Med Phys*, 33:1573–1582, Jun 2006.

[52] I. Kawrakow and M. Fippel. Investigation of variance reduction techniques for Monte Carlo photon dose calculation using XVMC. *Phys Med Biol*, 45:2163–2183, Aug 2000.

[53] I. Kawrakow and D. W. Rogers. The EGSnrc Code System: Monte Carlo simulation of electron and photon transport. Ottawa: Ionizing Radiation Standards, National Research Council of Canada, NRCC Report PIRS-701; 2002.

[54] H. H. Liu, T. R. Mackie, and E. C. McCullough. A dual source photon beam model used in convolution/superposition dose calculations for clinical megavoltage x-ray beams. *Med Phys*, 24:1960–1974, Dec 1997.

[55] H. H. Liu, T. R. Mackie, and E. C. McCullough. Calculating dose and output factors for wedged photon radiotherapy fields using a convolution/superposition method. *Medical Physics*, 24(11):1714–1728, 1997.

[56] H. H. Liu, E. C. McCullough, and T. R. Mackie. Calculating dose distributions and wedge factors for photon treatment fields with dynamic wedges based on a convolution/superposition method. *Medical Physics*, 25(1):56–63, 1998.

[57] C. M. Ma, C. W. Coffey, L. A. DeWerd, C. Liu, R. Nath, S. M. Seltzer, and J. P. Seuntjens. AAPM protocol for 40-300 kV x-ray beam dosimetry in radiotherapy and radiobiology. *Med Phys*, 28:868–893, Jun 2001.

[58] T. R. Mackie, A. F. Bielajew, D. W. Rogers, and J. J. Battista. Generation of photon energy deposition kernels using the EGS Monte Carlo code. *Phys Med Biol*, 33:1–20, Jan 1988.

[59] T. R. Mackie, J. W. Scrimger, and J. J. Battista. A convolution method of calculating dose for 15-MV x rays. *Med Phys*, 12:188–196, 1985.

[60] M. J. Murphy, J. Balter, S. Balter, J. A. BenComo, I. J. Das, S. B. Jiang, C. M. Ma, G. H. Olivera, R. F. Rodebaugh, K. J. Ruchala, H. Shirato, and F. F. Yin. The

management of imaging dose during image-guided radiotherapy: report of the AAPM Task Group 75. *Med Phys*, 34:4041–4063, Oct 2007.

[61] Azam Niroomand-Rad, Michael T. Gillin, Francisco Lopez, and Daniel F. Grimm. Performance characteristics of an orthovoltage x-ray therapy machine. *Medical Physics*, 14(5):874–878, 1987.

[62] NIST. Glossary of Radiation Physics for Radiation Therapy. http://physics.nist.gov/Divisions/Div846/Glossary/glossary.html.

[63] J. E. O'Connor. The variation of scattered x-rays with density in an irradiated body. *Phys Med Biol*, 1:352–369, Apr 1957.

[64] J. M. Pawlowski, C. W. Coffey, and G. X. Ding. A medium-dependent correction-based algorithm for calculating imaging dose resulting from kv x-rays. *Med Phys*, 36:2758, 2009 (abstract).

[65] J. M. Pawlowski, C. W. Coffey, and Ding G. X. A new approach to model-based dose calculations for kilovoltage beams. *Med Phys*, 37:3382, 2010 (abstract).

[66] J. M. Pawlowski and G. X. Ding. A new approach to account for the medium-dependent effect in model-based dose calculations for kilovoltage x-rays. *Phys Med Biol*, 56:3919–3934, Jul 2011.

[67] J M Pawlowski and GX Ding. Mo-f-110-02: A new model-based dose calculation algorithm for kilovoltage x- rays. volume 38, pages 3727–3727. AAPM, 2011 (abstract).

[68] D. W. Rogers, B. A. Faddegon, G. X. Ding, C. M. Ma, J. We, and T. R. Mackie. BEAM: a Monte Carlo code to simulate radiotherapy treatment units. *Med Phys*, 22:503–524, May 1995.

[69] J. W. Scrimger and S. G. Connors. Performance characteristics of a widely used orthovoltage x-ray therapy machine. *Medical Physics*, 13(2):267–269, 1986.

[70] J. P. Seuntjens and C. M. Ma. Dose conversion factors and depth scaling for tissue dose calculations in kilovoltage x-ray beams. *Med Phys*, 26:1421, 1999. (Abstract).

[71] D. Sheikh-Bagheri and D. W. O. Rogers. Monte Carlo calculation of nine megavoltage photon beam spectra using the BEAM code. *Medical Physics*, 29(3):391–402, 2002.

[72] T. B. Shope, R. M. Gagne, and G. C. Johnson. A method for describing the doses delivered by transmission x-ray computed tomography. *Med Phys*, 8:488–495, 1981.

[73] R. L. Siddon. Fast calculation of the exact radiological path for a three-dimensional CT array. *Med Phys*, 12:252–255, 1985.

[74] E. Spezi, P. Downes, E. Radu, and R. Jarvis. Monte Carlo simulation of an x-ray volume imaging cone beam CT unit. *Med Phys*, 36:127–136, Jan 2009.

[75] N. Theocharopoulos, J. Damilakis, K. Perisinakis, A. Tzedakis, A. Karantanas, and N. Gourtsoyiannis. Estimation of effective doses to adult and pediatric patients from multislice computed tomography: A method based on energy imparted. *Medical*

Physics, 33(10):3846–3856, 2006.

[76] F. Verhaegen, A. E. Nahum, S. Van de Putte, and Y. Namito. Monte Carlo modelling of radiotherapy kV x-ray units. *Phys Med Biol*, 44:1767–1789, Jul 1999.

[77] B. R. Walters, G. X. Ding, R. Kramer, and I. Kawrakow. Skeletal dosimetry in cone beam computed tomography. *Med Phys*, 36:2915–2922, Jul 2009.

[78] B.R. Walters, I. Kawrakow, and D. W. Rogers. DOSXYZnrc users manual. Ottawa: National Research Council of Canada, NRCC Report PIRS-794revB; 2006.

[79] N. Wen, H. Guan, R. Hammoud, D. Pradhan, T. Nurushev, S. Li, and B. Movsas. Dose delivered from Varian's CBCT to patients receiving IMRT for prostate cancer. *Phys Med Biol*, 52:2267–2276, Apr 2007.